



Universiteit
Leiden
The Netherlands

Formation of graphene and hexagonal boron nitride on Rh(111) studied by in-situ scanning tunneling microscopy

Dong, G.

Citation

Dong, G. (2012, November 7). *Formation of graphene and hexagonal boron nitride on Rh(111) studied by in-situ scanning tunneling microscopy*. *Casimir PhD Series*. Kamerlingh Onnes Laboratory, Leiden Institute of Physics, Faculty of Science, Leiden University. Retrieved from <https://hdl.handle.net/1887/20105>

Version: Corrected Publisher's Version

License: [Licence agreement concerning inclusion of doctoral thesis in the Institutional Repository of the University of Leiden](#)

Downloaded from: <https://hdl.handle.net/1887/20105>

Note: To cite this publication please use the final published version (if applicable).

Cover Page



Universiteit Leiden



The handle <http://hdl.handle.net/1887/20105> holds various files of this Leiden University dissertation.

Author: Dong, Guocai

Title: Formation of graphene and hexagonal boron nitride on Rh(111) studied by in-situ scanning tunneling microscopy

Date: 2012-11-07

**Formation of graphene and
hexagonal boron nitride on Rh(111) studied
by in-situ scanning tunneling microscopy**

Guocai Dong

**Formation of graphene and hexagonal boron nitride on
Rh(111) studied by in-situ scanning tunneling microscopy**

Guocai Dong

**Formation of graphene and hexagonal boron nitride on
Rh(111) studied by in-situ scanning tunneling microscopy**

PROEFSCHRIFT

ter verkrijging van

de graad van Doctor aan de Universiteit Leiden

op gezag van Rector Magnificus prof. mr. P.F. van der Heijden

volgens besluit van het College voor Promoties

te verdedigen op woensdag 7 november 2012

klokke 11:15 uur

door

Guocai Dong

geboren te Heilongjiang, China

in 1981

PROMOTIECOMMISSIE

Promotor: Prof. Dr. J. W. M. Frenken (Leiden University)

Overige leden: Prof. Dr. J. Aarts (Leiden University)

Prof. Dr. E.R. Eliel (Leiden University)

Prof. Dr. T. Greber (University of Zürich)

Prof. Dr. T. Michely (University of Cologne)

Prof. Dr. P. Rudolf (University of Groningen)

Prof. Dr. R. Tromp (IBM, Leiden University)

Dr.ir. S.J. van der Molen (Leiden University)

Dr. A. Yanson (Leiden University)

Casimir PhD series, Delft-Leiden 2012-31

ISBN: 978-90-8593-138-6

An electronic version of this thesis can be found at
<https://openaccess.leidenuniv.nl> and at <http://www.interfacephysics.nl>.

The work described in this thesis was made possible by financial support from the Foundation for Fundamental Research on Matter (FOM/NWO), the EU project 'Nanomesh' (No. FP6-013817), and an ERC Advanced Investigator Grant. This work has been performed at the Kamerlingh Onnes Laboratory, Leiden Institute of Physics, Leiden University, The Netherlands.

To my family

Contents

CHAPTER 1 INTRODUCTION	1
1.1 ULTRATHIN FILM DEPOSITION.....	1
1.2 NANOMESH.....	2
1.2.1 <i>The structure and properties of nanomesh</i>	2
1.2.2 <i>h-BN growth on other metals</i>	4
1.2.3 <i>Formation mechanism of the nanomesh structure</i>	4
1.3 GRAPHENE	5
1.3.1 <i>The properties of graphene</i>	7
1.3.2 <i>Potential applications of graphene</i>	8
1.3.3 <i>Graphene production</i>	9
1.3.4 <i>Graphene growth on transition metals</i>	10
1.4 THIS THESIS	12
CHAPTER 2 EXPERIMENTAL	13
2.1 EXPERIMENTAL SETUP.....	13
2.1.1 <i>Vacuum chamber and equipment</i>	13
2.1.2 <i>The Variable-Temperature STM</i>	15
2.1.3 <i>The heating of the sample</i>	18
2.2 THE RH(111) SAMPLE.....	20
2.3 THE MOIRÉ PATTERNS.....	21
PART I NANOMESH FORMATION ON RH (111)	26
CHAPTER 3 INTRODUCTION OF PART I	27
3.1 BACKGROUND.....	27
3.2 EXPERIMENTAL METHODS.....	28
3.3 THIS PART OF THE THESIS.....	31

CHAPTER 4 NANOMESH FORMATION AT DIFFERENT TEMPERATURES ON RH(111) ..	33
4.1 INTRODUCTION	33
4.2 NANOMESH FORMATION FROM BORAZINE DEPOSITED AT ROOM TEMPERATURE.....	33
4.3 NANOMESH FORMATION FROM BORAZINE DEPOSITED BETWEEN 627 K AND 865 K	36
4.4 NANOMESH FORMATION FROM BORAZINE DEPOSITED AT 978 K.....	38
4.4.1 <i>The growth unit</i>	39
4.4.2 <i>Nanomesh island shape</i>	39
4.4.3 <i>Nanomesh growth along different edges</i>	40
4.4.4 <i>Growth barriers of the nanomesh structure at various sites</i>	42
4.5 CONCLUSIONS	46
CHAPTER 5 ADSORPTION AND DECOMPOSITION OF BORAZINE	49
5.1 THE BREAKING OF B-N BONDS	49
5.2 DESORPTION OF BORAZINE MOLECULES AND B AND N ATOMS.....	50
5.3 FROM WHICH BORAZINE IS THE <i>H</i> -BN OVERLAYER FORMED?	51
5.4 DISCUSSION	58
5.5 CONCLUSION.....	58
CHAPTER 6 DEFECTS IN THE NANOMESH LATTICE.....	59
6.1 STRUCTURE AND FORMATION OF DOMAIN BOUNDARIES.....	59
6.2 REMOVAL OF DOMAIN BOUNDARIES.....	62
6.3 CONCLUSION.....	65
PART II GRAPHENE FORMATION ON RH(111)	66
CHAPTER 7 INTRODUCTION TO PART II.....	67
7.1 GENERAL BACKGROUND.....	67
7.2 EXPERIMENTAL METHOD.....	68
7.3 THIS PART OF THE THESIS	69

CHAPTER 8 PARAMETERS INFLUENCING GRAPHENE AND CARBIDE FORMATION.....	71
8.1 INTRODUCTION	71
8.2 THE TEMPERATURE DEPENDENCE OF GRAPHENE AND CARBIDE FORMATION	71
8.3 THE CRUCIAL ROLE OF THE HISTORY OF THE SAMPLE.....	77
8.4 CONCLUSION	80
CHAPTER 9 TOWARDS THE OPTIMAL GROWTH RECIPE	81
9.1 INTRODUCTION	81
9.2 USING SEGREGATED CARBON TO FORM GRAPHENE	81
9.3 FURTHER ETHYLENE DEPOSITION	83
9.4 CONCLUSION	84
CHAPTER 10 RH ISLAND FORMATION INDUCED BY GRAPHENE GROWTH.....	85
10.1 INTRODUCTION	85
10.2 EXPERIMENT.....	85
10.3 TUNNELING CURRENT VS. ADATOM DENSITY.....	89
10.4 MODELS	91
10.5 CONCLUSION	93
CHAPTER 11 GROWTH KINETICS	95
11.1 INTRODUCTION	95
11.2 HOW THE MOIRÉ PATTERN INFLUENCES THE GROWTH	98
11.3 THE INFLUENCE OF CORNER STRUCTURE ON KINK CREATION.....	101
11.4 THE INFLUENCE OF CORNER ENERGY	103
11.5 DIFFERENCE BETWEEN GROWTH AT EXTERNAL AND INTERNAL GRAPHENE EDGES.....	103
11.6 FROM WHICH CARBON DOES GRAPHENE GROW?.....	105
11.7 CONCLUSION	106
CHAPTER 12 THE STRUCTURE OF GRAPHENE ON RH.....	107
12.1 INTRODUCTION	107

Contents

12.2 EXPERIMENT	108
12.3 RESULT AND CONCLUSION	110
CHAPTER 13 A UNIVERSAL DESCRIPTION OF GRAPHENE FORMATION ON TRANSITION METALS	113
REFERENCES	119
SUMMARY	126
SAMENVATTING	132
ACKNOWLEDGEMENTS	139
PUBLICATIONS AND PATENTS	140
CURRICULUM VITAE	141

Chapter 1 Introduction

In this thesis, the formation of hexagonal boron nitride (*h*-BN) 'nanomesh' structures and of graphene on Rhodium (111) is studied experimentally. The structures of *h*-BN and graphene are extremely similar: both of them are single atomic layers with a honeycomb lattice, and the lattice constants are nearly identical. Both materials introduce novel properties and have the potential for a variety of applications. In this thesis, the layers were grown by chemical vapor deposition (CVD) on Rh(111). During growth, the formation processes were tracked by scanning tunneling microscopy (STM). This was performed *in situ*, namely during deposition at the elevated temperatures, required for the growth. In this way, we have obtained detailed knowledge of the formation mechanisms. In this thesis, basic surface science principles are employed to explain the observed, special growth behavior. Our understanding of the mechanisms at play has enabled us to compose new, improved deposition recipes that result in higher quality nanomesh and graphene layers. This knowledge is not only valuable for these specific systems, but it also deepens our general insights into deposition and growth of atomically thin layers.

1.1 Ultrathin film deposition

The deposition and growth of thin films on well-defined substrates forms one of the traditional topic areas of surface science [1-5]. The idea usually is to use the film to modify the surface properties, either chemically, electronically, optically, mechanically, etc. The deposited films are often base materials for practical applications, such as electronic devices, protective coatings, anti-reflection coatings, and coatings to reduce friction and wear. The importance of applications in each of these directions has been a real thrust for the surface-science investigations of the laws that govern the nucleation and the growth, the structures that form, the preferred orientations, the interfacial

arrangements, including mixing layers and misfit dislocations, the larger-scale grain structure, the smoothness or roughness, the strain in the film, etc. Nowadays, a dominant role is played by the nucleation and growth of single- or few-monolayer films that form in a self-limiting fashion that automatically leads to the formation of the thinnest possible films. These films may be either regarded as an interesting coating of the underlying materials, as a scaffold for further deposits, or as a thin foil that is to be detached later from the substrate on which it is grown, in order to be transferred to either another substrate or to a suspension structure for application as a free-standing film. The two materials that this thesis concentrates on are *h*-BN nanomesh [6] and graphene [7, 8].

1.2 Nanomesh

The spontaneous formation of a regular superstructure of hexagonal boron nitride (*h*-BN) on a metal surface was first reported by Corso et.al in 2004 [6]. The original recipe for preparing the overlayer is the exposure of a Rh(111) surface at 1050K to a low pressure of pure borazine gas (HBNH)₃. The *h*-BN layer that results from this procedure was found to adopt a highly regular superstructure that has been called the 'nanomesh', with 2 nm diameter depressions and a 3.2 nm period, as observed by scanning tunneling microscopy (STM). An example of an STM image of the nanomesh structure on Rh(111) is shown in Fig. 1.1.

1.2.1 The structure and properties of nanomesh

Ultraviolet photoelectron spectroscopy (UPS) revealed a splitting of the σ -band, which indicated two different types of bonds between the overlayer and the Rh [6]. Based on these observations, the atomic structure proposed by the first report was two atomic layers of hexagonal boron nitride, with holes in each layer. This was regarded as an ideal self-assembling template, since the dangling bonds at the edges of the holes in the top layer would be available as a regular pattern of binding sites for other molecules, with a

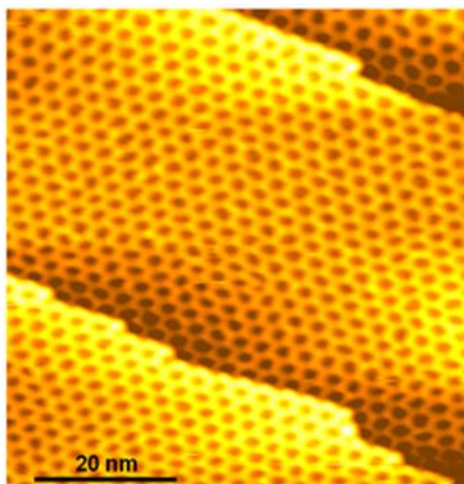


Fig. 1.1 An STM image of the *h*-BN nanomesh structure, prepared by exposing a Rh(111) surface to borazine at 1050K. (part I of this thesis) The structure features 2 nm diameter holes and a period of 3.2 nm. Sample voltage: $V_b = 1.4$ V. Tunneling current $I_t = 0.05$ nA.

wide variety of possible functionalities. However, subsequent theoretical calculations showed that the two-layer model costs too much energy, and that the most probable model structure is one consisting of a highly corrugated single *h*-BN layer [9-11]. The single-layer model was soon confirmed by a surface X-ray diffraction (SXR) study [12]. The size of the nanomesh unit cell is 13 x 13 BN units on 12 x 12 Rh atoms, which was reported by a low energy electron diffraction (LEED) study [6] and confirmed by theoretical calculations [9-11], SXR [12, 13], and high-resolution STM [14]. Recently, a LEED study of *h*-BN formation on Rh-(yttria-stabilized zirconia)-Si(111) exhibited a (14 x 14) BN on 13 x 13 Rh(111) superstructure [15]. The reason for this is still under debate [13]. High-resolution SXR showed that the 13 x 13 BN on 12 x 12 Rh structure is stable up to a temperature of 1107 K. From this collection of studies, we can conclude that the structure of the *h*-BN nanomesh on bulk Rh(111) is a single, corrugated layer of *h*-BN, with hexagonally arranged high and low regions, which have a height difference of 0.55 Å [11]. The unit cell of the nanomesh pattern contains 13 x 13 unit cells of the *h*-BN lattice, fitting onto 12 x 12 unit cells of the underlying Rh(111) surface.

Although the nanomesh is a single-layer structure, it was demonstrated to be sufficiently corrugated to act as a two-dimensional scaffold for the deposition of bucky balls in the first report [6]. Further studies showed that it can be a template for assembling nanoparticles [16] and for trapping molecules [14, 17, 18]. The nanomesh coating has been demonstrated to remain intact under ambient conditions [12], in liquids [19], and at high temperatures [13, 20], thus protecting the underlying metal. This stability makes the nanomesh an ideal template and coating with great application potential.

1.2.2 *h*-BN growth on other metals

h-BN can be grown as a single-layer structure on many metals [9, 11, 16, 21-29], using the method of CVD. On most surfaces with a lattice constant that differs from that of the *h*-BN, a superstructure is found. Initially, all these superstructures were considered to be mere moiré patterns, i.e. straightforward beating patterns between the lattices. Interestingly, there are remarkable differences between the corrugation amplitudes of the superstructures on different substrates. For example, on Pt(111), the *h*-BN overlayer stays nearly flat [21, 30]. On the other hand, on Ru(0001), *h*-BN forms an extremely corrugated structure, similar to that on Rh(111), with a unit cell of 14 x 14 BN unit cells on 13 x 13 Ru unit cells [22, 28, 31, 32]. Studies using X-ray photoelectron spectroscopy (XPS) and SXRD showed the strength of the interfacial chemical interaction between *h*-BN and the substrates to rise in the series Pt(111)–Ir(111)–Rh(111)–Ru(0001) [21]. It was concluded that, in addition to the lattice mismatch, a large strength of interfacial chemical bonding is a prerequisite for the formation of a significantly corrugated layer [21, 30].

1.2.3 Formation mechanism of the nanomesh structure

In spite of the growing number of studies on the structure and properties of the nanomesh overlayers, the mechanisms by which these layers nucleate and grow are virtually unexplored [20]. This is due to several practical reasons. Firstly, the unit cell contains 13 x 13 BN units on 12 x 12 Rh atom distances, which is difficult for theoretical and computational approaches. Secondly, the conditions for the CVD reaction, in particular the required high temperatures, disqualify many experimental techniques, such

as STM. Thirdly, most of the methods that can be applied at high temperature only give information in reciprocal space and average over large surface areas, which makes it very difficult to extract the microscopic mechanisms at work. To reveal the details of the kinetic processes, local, real-space observations are more direct. One technique, which readily gives real-space images and can be used at elevated temperatures, is low-energy electron microscopy (LEEM). Unfortunately, the size of the nanomesh unit cell is just at the resolution limits of LEEM, so it is difficult to study the nanomesh growth in detail with that technique.

What are the influences of the high temperature and the superstructure on the growth of the nanomesh structure? The high temperature could be necessary to crack the borazine molecules, releasing hydrogen and possibly rupturing B-N bonds, in order to form reactive precursors that stick sufficiently strongly to the surface and serve as the growth units, from which the overlayer can be assembled. One can also imagine that a high temperature would be required to provide sufficient lateral mobility for crystallizing the otherwise disordered overlayer into the perfectly periodic nanomesh structure. The growth unit of the nanomesh could be as simple as a single unit of *h*-BN, and the superstructure could just be formed as a moiré pattern. Or perhaps the superstructure also influences the growth process. To address these questions, a variable-temperature STM was used, which allows fast scanning and imaging over a wide range of temperatures and during substantial temperature changes [33, 34]. STM observations under the reported growth conditions, i.e. *during* borazine exposure at temperatures up to 1200 K, were carefully analyzed in this thesis, which unveiled the mechanisms of the adsorption, and the decomposition of borazine and the *h*-BN nucleation and growth in detail. These results are presented in part I of this thesis.

1.3 Graphene

Graphene is a planar sheet of sp^2 -bonded carbon atoms, a single atom thick, which are densely packed into a honeycomb crystal lattice. Alternately, it can be viewed as a single atomic layer of graphite, while graphite itself consists of many graphene sheets stacked together. The interatomic distance of carbon atoms in graphene is 0.142 nm. Graphene is one of many carbon allotropes, along with diamond, graphite, carbon nanotubes, and

1.3 Graphene

fullerenes. Diamond and graphite are three-dimensional (3-D) structures; carbon nanotubes can be considered a 1-D structure; fullerenes are molecules where carbon atoms are arranged spherically, and hence are 0-D objects; they feature discrete energy states [35]. Graphene fits nicely into the gap, being the 2-D allotrope of carbon. Among systems with only carbon atoms, graphene plays an important role, since it forms the basis for the understanding of the electronic properties of the other allotropes [35]. Besides its interesting and important physical properties, graphene also provides the focus for further application-oriented research, for example concerning its electronic performance (see next section) [35-37], in view of its possible role as a future replacement for silicon-based electronics. Because of its importance in the scientific world and for its applications, this simple material has drawn enormous attention during the last decade. Fig. 1.2 shows the recent increase of the publication rate of papers concerning graphene, especially after 2004, when the first experimental evidence was reported of the electronic properties of graphene [7, 38], and even more so after 2005, when follow-up experiments confirmed that its charge carriers were massless Dirac fermions [8, 39]. This led to an explosion of articles devoted to graphene, which has been called the graphene 'gold rush' [38].

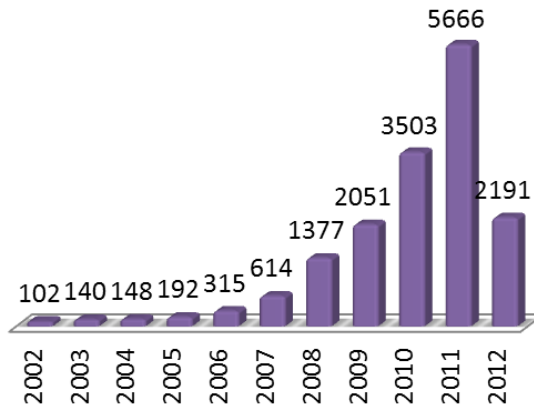


Fig. 1.2 The number of scientific papers published on graphene in each year over the last ten years. A dramatic increasing can be seen after 2005. This graph was obtained by searching the *ISI Web of KnowledgeTM* for the key word 'graphene' (including data up to May 3, 2012).

1.3.1 The properties of graphene

Graphene has many properties that make it special, for example, its electronic properties, its extreme mechanical deformability in combination with extreme yield strength, and its chemical stability in an atmospheric environment. The electronic properties of graphene are receiving most attention. They combine appealing fundamental physics with the potential for future electronics applications. Graphene can be considered as a basic building block for graphitic materials of all other dimensionalities. It can be wrapped up into 0-D fullerenes, rolled into 1-D nanotubes [40], or stacked into 3-D graphite [35, 38]. Theoretically, graphene (or ‘2-D graphite’) has been studied for sixty years [38, 41, 42], and it has been used for describing properties of various carbon-based materials.

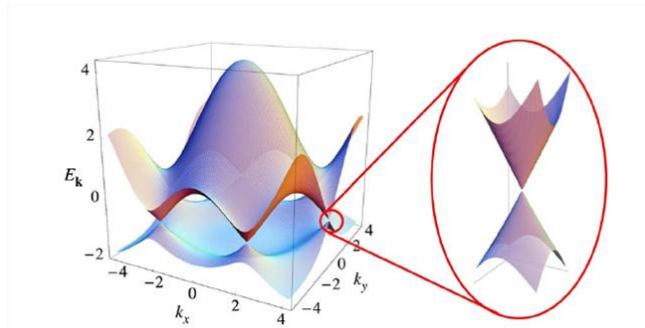


Fig. 1.3 Electronic energy dispersion of the graphene lattice. Left: the energy as a function of momentum components k_x and k_y in the plane of the graphene. Right: a zoom-in of the energy bands near one of the Dirac points. (From ref. [35])

In 2009, A.H. Castro Neto reviewed the basic theoretical aspects of graphene [35]. Graphene is a semi-metal, or zero-gap semiconductor, and has a linear dispersion at its Dirac points (Fig. 1.3). This was discovered by Wallace, using the tight-binding approximation, already in 1947 [41]. The energy dispersion for electrons in the vicinity of the Dirac points of graphene can be described by [35, 41]: $E_{\pm}(q) \approx \pm V_F |q| + O[(q/K)^2]$, where E is the energy with respect to the Fermi level, q is the difference in momentum from the Dirac point, and V_F is the Fermi velocity, with a value $V_F \approx 1 \times 10^6$ m/s. This energy dispersion can be derived from the Dirac equation for massless particles. This behavior was demonstrated experimentally sixty years later [8, 39]. The Dirac electrons

can be controlled by the application of external electric and magnetic fields, or by altering sample geometry and/or topology [35].

Dirac fermions behave in unusual ways when magnetic fields are applied, which leads to special phenomena, such as the anomalous integer quantum Hall effect (IQHE) [8, 39] and the fractional quantum Hall effect (FQHE) [43]. Different from the IQHE observed in other systems, the IQHE in graphene can be observed at room temperature [35, 44]. In fact, the anomalous IQHE should be regarded as the trademark of Dirac fermion behavior. Another interesting feature of Dirac fermions is that they can be transmitted with probability unity through a classically forbidden region, due to the so-called Klein paradox [45].

1.3.2 Potential applications of graphene

The number of potential applications of graphene is enormous, and it seems to increase further every day. In order to provide an impression, I simply reproduce the list of proposed application areas of graphene that can be found on Wikipedia [46].

1. Room temperature distillation of ethanol for fuel and human consumption
2. Single-molecule gas detection
3. Graphene nanoribbons
4. Graphene transistors
5. Graphene optical modulators
6. Integrated circuits
7. Electrochromic devices
8. Transparent conducting electrodes
9. Reference material for characterizing electroconductive and transparent materials
10. Thermal management materials
11. Solar cells
12. Ultracapacitors
13. Engineered piezoelectricity
14. Graphene biodevices
15. Anti-bacterial
16. Study of liquids

Which of these applications will become truly dominant in its own application area remains to be seen. In any case it is evident from the long list and wide variety of potential practical applications that graphene should be expected to rapidly acquire significant economical and societal impact.

1.3.3 Graphene production

Graphene is a single layer of graphite, and graphite is a traditional base material, for example in lubricants, ink and pencils. So simply writing on paper with a pencil can create flakes of graphene. But the problem is that they cannot be located and distinguished easily from multilayer graphene or plain graphite (thick multilayers). The first experimentally produced and verified graphene was obtained in 2004 by mechanical exfoliation of graphite [7]. Scotch tape was used to repeatedly separate graphite crystals into progressively thinner pieces. The tape, with the optically transparent flakes attached to it, was dissolved in acetone and, after a few further steps, the flakes, including single-layer graphene, multilayer graphene and graphite, were transferred onto the native oxide on a Si wafer. Individual atomic planes were then 'hunted' for under an optical microscope. Later, researchers simplified the technique, and started using dry deposition, avoiding the stage where graphene floated in a liquid. Relatively large crystallites have been obtained by this technique. As remarked before, graphene is relatively easy to make, but hard to find. The key point of this method is the possibility of visual recognition of graphene on a properly chosen substrate, which provides a small, but noticeable, optical contrast under an ordinary optical microscope [7]. Most of the experiments on graphene have been performed using this method [43, 47]. It nicely provides experimentalists with the best quality in topographical flatness [47] and electron mobility [43]. With this method, electron mobility in graphene sample has reached $200,000 \text{ cm}^2 \text{ V}^{-1}\text{s}^{-1}$ [43]. The drawback of this method is, of course, reproducibility. From an application point of view, it is hard to imagine any production facility using microscopes to find tiny bits of graphene for electronic devices.

Since 2004, researchers have tried out many ways for a reproducible, bottom-up production of graphene. One method is to heat silicon carbide to high temperatures ($>1100 \text{ }^\circ\text{C}$), in order to make it sublime silicon and thereby reduce its surface to graphene [48, 49]. The choice of the face of the silicon carbide that is used for graphene

creation, either silicon-terminated or carbon-terminated, strongly influences the thickness (i.e. the number of layers), mobility, and carrier density of the graphene. This process produces a graphene sample size that is dependent on the size of the SiC substrate. However, the size of the domains is still in the order of hundreds of nanometers [48, 49]. Although the QHE could be measured with the graphene samples created by this method [48], the electronic mobility in this graphene only reached $2700 \text{ cm}^2 \text{ V}^{-1} \text{ s}^{-1}$, [50] which is much lower than for the scotch tape method.

1.3.4 Graphene growth on transition metals

A very promising alternative method to produce precisely one single layer of graphene is chemical vapor deposition (CVD) on transition metal (TM) surfaces [25, 51-58]. It is the method that we have concentrated on in the work described in this thesis. TMs are favorable substrates for graphene growth by CVD because they are excellent catalysts for hydrocarbon decomposition and they strongly bind the graphene that forms as a consequence, while newly arriving hydrocarbon molecules do not stick to or decompose on the graphene that has already formed. In addition, because the solubility of carbon in TMs often depends strongly on temperature, graphene can also be made using segregated carbon [51, 53, 57, 59, 60]. In most investigations of the growth of graphene, the graphene and its properties are typically inspected only after the growth, at room temperature or below. After samples have been prepared at high temperature and cooled down subsequently, it is not easy to distinguish which kind of carbon, segregated or deposited, has been responsible for the formation of the graphene layer. Actually, graphitic layers on TMs had been investigated much earlier [25-27, 59, 61, 62], before specific attention was paid to graphene.

As a consequence of its strong interaction with the substrate, graphene on top of TMs is very different from the idealized free-standing graphene. It does not have the interesting electronic properties mentioned before, but it does have its own special appeal, for example, being the template for the self assembly of additional overlayers [17], or the graphene-metal contact serving a spin filter [63, 64], etc. Recently, in order to produce free-standing graphene, several recipes have been introduced for transferring graphene from TMs onto other substrates [56, 60, 65, 66]. With these recipes, CVD-grown graphite layers on TMs have become a good candidate for producing high-quality graphene. A

promising carrier mobility of 4,000 to 7,350 $\text{cm}^2 \text{V}^{-1}\text{s}^{-1}$ has already been reported for graphene, obtained via this route [67-70]. The size of graphene made by CVD method is reported up to 30 inch [70].

No matter in what form the graphene is produced, free-standing or on a substrate, for many applications it is the structural quality of the graphene that limits its properties and therefore the quality of the final products in which it can be applied. The typical types of imperfections introduced by the CVD method on TMs are impurities and structural defects. The problem of impurities can be solved by using a sufficiently clean production setup and sufficiently clean materials (metal substrate and precursor gasses). The structural defects include other carbon phases (e.g. metal carbide), domain boundaries between different graphene patches, point defects [54] (e.g. pentagons and heptagons [71]) and thickness variations (voids or multilayers). It has been demonstrated that such defects can influence the electronic properties of graphene [71]. To reduce and eventually completely avoid the occurrence of structural defects, full control of the formation mechanism of graphene is necessary. This can only come through a thorough, atomic-scale understanding of the process. Once we have acquired a full understanding of the basic mechanisms of graphene formation and possible competing processes, we can use that to subsequently develop an optimal growth recipe.

In spite of their obvious importance, only a very limited number of experiments have directly addressed the important kinetic processes [51, 53]. CVD of graphene on TMs is typically performed at elevated temperatures, where the interaction between the carbon and the TMs can lead to very complex behavior. If measurements are performed at room temperature or lower, after the graphene has been grown, it is hard to infer the reaction path, especially if part of this path also involves the cool-down of the sample. Unfortunately, most of the experimental methods that can be used *in situ* at elevated temperatures do not have atomic resolution, which is also a prerequisite for obtaining detailed information on the growth kinetics [56].

Our special-purpose, variable-temperature scanning tunneling microscope (VT-STM) is well-suited for this purpose [33, 34], since it enables one to follow the reaction and growth of graphene *in situ*. Ethylene decomposition on Rh(111) is taken as a generic example of carbon deposition on TMs. The interaction between carbon and Rh can lead to carbide formation [72], carbon dissolution [73], and graphene formation [61]. These

are also the typical 'products' that can be formed on other TMs. Actually, carbon is the main contaminant in Rh crystals.

The complexity of the carbon-on-Rh(111) system makes it a good example for demonstrating, in general, the interaction between carbon and TMs. The 3-fold (111) orientation was chosen, to act as a template for graphene crystallization. In addition, graphene forms an easily recognizable moiré pattern on Rh(111). A simple calculation shows that the moiré pattern 'magnifies' the misfit defects between the lattice of the graphene layer and that of the Rh substrate. For example, 1 degree of actual graphene rotation with respect to the Rh lattice results in a 10 degree apparent rotation in the moiré pattern. In this way, atomic information about graphene can be achieved even without actually achieving atomic resolution in STM. In part II, detailed observations of this system are provided, such as the temperature range for graphene and carbide formation and for their stability, the dependence of the forming structures on temperature, and the role of the precise initial conditions. Armed with this information, we demonstrate that a higher-quality graphene can be obtained. Also carbide formation can be avoided, and the dissolved carbon can be controlled to form graphene. Based on this, we attempt to derive the optimal recipe for obtaining low-stress, single-orientation, single-crystalline, single-layer graphene.

1.4 This thesis

This thesis starts with a detailed description of the experimental setup and basic experimental procedures in Chapter 2. The main component of the thesis is devoted to the formation of monolayers on Rh(111). This is organized in two parts, part I (from Chapter 3 to Chapter 6) concerning the growth of *h*-BN nanomesh overlayers and part II (from Chapter 7 to Chapter 13) to the growth of graphene. Each part starts with a short introductory chapter (Chapter 3 and Chapter 7). The thesis ends with a summary for the layman.

Chapter 2 Experimental

2.1 Experimental setup

2.1.1 Vacuum chamber and equipment

All measurements in this thesis were performed with a dedicated STM-setup in the Kamerlingh Onnes Laboratory of Leiden University. This setup consisted of a single ultrahigh vacuum (UHV) chamber, equipped with a scanning tunneling microscope (STM), a low-energy electron diffraction (LEED) apparatus, an Auger electron spectroscopy (AES) instrument, and a quadrupole mass spectrometer (QMS), for analysis purposes¹.

The base pressure of the vacuum system was 1.5×10^{-11} mbar. During measurements, the vacuum level was kept below 2×10^{-10} mbar. To achieve and maintain this vacuum, a single 170 liter/second magnetically levitated turbo-molecular pump, a 410 liter/second ion getter pump, and a titanium sublimation pump, integrated into a cold trap, were connected to the UHV chamber. Also, the entire vacuum system was extensively degassed by a bake-out procedure up to 450 K and the sample holder and STM components were further degassed by prolonged annealing of the Rh sample to 800K.

The pressure in the UHV system was measured by an ion gauge in the middle of the chamber. The measured pressure had not been corrected for the different sensitivities to

¹ Instruments and techniques that are considered standard for surface science will not be given a detailed introduction in this thesis. The operation principles of these can be found in most surface science textbooks.

2.1 Experimental setup

different gases. The difference in location of the pressure gauge and the sample may have resulted in a further error in the recorded pressure. To correct for these errors, a calibration experiment using borazine deposition (section 5.3) was performed, and the calibration constant for ethylene was calculated from that for borazine, using the known relative sensitivities for the two gases.

To reduce the effect of vibrations on the STM measurements, several isolation stages were combined. The entire setup rested on four air legs, which were placed on a foundation separated from the foundation of the building. The setup was thus effectively decoupled from the vibrations of the building. The rotation pump that was connected to the turbo-molecular pump was placed on the building foundation, and its connection to the turbo-pump was made by long, flexible bellows. In this way, the effect of vibrations from the rotation pump was also reduced to a minimum. The influence of the vibrations of the turbo-pump was minimized by connecting it to the UHV chamber via bellows with a damping jacket. Together with the magnetic bearings of the turbo-pump, these measures reduced the residual vibrations in the STM images to such a low level that atomic resolution could be achieved even with the turbo-pump and the rotation pump running.

The rhodium sample was cleaned routinely by Ar^+ ion bombardment and annealing. The Ar^+ ions were produced in a differentially pumped, focused ion gun, fitted with a Wien mass filter. With the differential pumping on the ionization chamber, the pressure in the main chamber did not exceed 1×10^{-8} mbar, while the pressure in the ionization chamber was held at 5×10^{-4} mbar. The focusing and alignment of the ion beam were optimized with the help of a dummy sample in the form of a Faraday cup. The diameter of the beam was less than 1 mm, which is smaller than the size of the sample, so a $5 \times 5 \text{ mm}^2$ scanning was applied by use of sweep voltages on the deflection plates of the ion gun, in order to clean the whole sample. The sample holder was made of molybdenum, and coated by the sample material, in this case Rh, to avoid sputter deposition on the sample of other materials from the sample holder.

High-purity borazine $(\text{HBNH})_3$, was synthesized by the research group of Prof. Hermann Sachdev (University of Saarland). It was dosed into the UHV-system via a dosing valve from a container in which the material was stored at a reduced temperature, by means of a Peltier cooler. The container and dosing system were obtained from the research group of Prof. Jürg Osterwalder and Prof. Thomas Greber (University of Zurich). For each deposition experiment, the borazine was allowed to warm up temporarily. Ethylene

gas with a purity of 99.99% was purchased from ALDRICH™. This gas was dosed through a leak valve. The connections between gas bottles and valves were 6 mm stainless steel pipes. A turbo-pump was used to evacuate these gas lines. For high-purity deposition results it proved to be important to keep these lines clean by degassing (heating) and flushing them with the gas of choice (borazine or ethylene).

2.1.2 The Variable-Temperature STM

The central part of the setup was an STM, which had been optimized for (fast) scanning at high sample temperatures and also during substantial temperature variations [33, 34]. Like most other STMs, our Variable-Temperature STM (VT-STM) is using a piezoelectric tube, in our case with a length of 12 mm, to scan regions up to typically $3 \times 3 \mu\text{m}^2$, with sub-nanometer resolution. The macroscopic dimensions of the piezo element, the sample and other components in the mechanical path between the tip and the sample make that even modest temperature variations can cause a significant drift in an STM image. More dramatically, when the component of this drift in the z-direction, along the tip axis, were to exceed the control range of the piezo element, this would lead either to a situation where the surface drifts out of range or to a crash of the tip into the sample surface. For these reasons, most STMs are used either at room temperature or at a constant, low or (modestly) elevated temperature, at which the sample and microscope are first allowed to equilibrate for a long time, typically several hours, prior to the coarse tip-sample approach and imaging. The STM we were using could compensate for thermal drifts in all directions by its special design. The details of this can be found in ref [33]. Here, only a brief summary is given. As shown in Fig. 2.1, in the scanner, a radiation shield protects the piezo element from thermal radiation from the sample. Apart from its three legs, the scanner is cylindrically symmetrical around the axis of the tip. A finite-element analysis of the scanner was utilized to match the expansion of the legs with that of the assembly of the piezo element, the tip holder and the tip, in order to minimize the vertical drift of the tip, due to temperature changes of these components of the microscope. The sample was clamped into a molybdenum holder, with its surface against two ledges. The holder itself was clamped down with two extending arms on two supports. The ledges, the arms, and the supports all reside in the same plane, coinciding with the precise level of the tip apex. This configuration ensured that also expansions of the sample and its holder did not affect the vertical position of the surface plane with

2.1 Experimental setup

respect to the tip. With this design, neither the expansion of the piezo element and other components of the microscope nor that of the sample and sample holder can give rise to a significant tip-sample distance variation. In practice, experiments have been performed without the need for any mechanical adjustments in the tip height, while the sample temperature was being changed from 300 K to approximately 1200 K. In section 9.2, an example is given in which the same area of the sample was followed by the STM during a 50°C temperature variation.

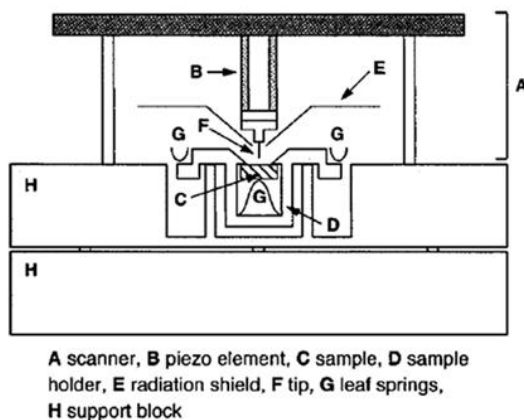


Fig. 2.1 Schematic cross section of the STM. The scanner A is cylindrically symmetric around the axis through the tip F. It rests with three legs on the support block H. A radiation shield E protects the piezo element B against thermal radiation from the sample C. The sample holder D is clamped down against two supports by leaf springs G. The sample is clamped up against two ledges of the sample holder. (from ref [33])

Fig. 2.2 (a) shows a schematic top view of the holder. Four arms extend from the holder. Two of these are rotated against vertical posts, which form part of the Mo support block. The other two are shaped like knife-edges and are pressed down against two oppositely tilted supports by two leaf springs. When the holder is heated, it expands outwards along the four extensions, but the center stays at its original position. To make coarse adjustment possible, the tip is mounted 1 mm outside this stable center position. When the sample holder is placed in the support block, it first makes contact with the vertical posts. At that stage, the sample holder still has the freedom to rotate around the axis through these first two contact points. This rotational freedom ensures that both knife-

edges will make contact with their supports, when the holder is pushed further into its final position. In this way, a completely unstrained four-point mechanical contact is established. Once in place, the sample holder can still rotate around the two knife-edges, which allows coarse adjustment of the tip-sample separation. This design, together with the choice of low-expansion-coefficient materials, makes it possible to follow the same area on the surface during hundreds of degrees of temperature variation.

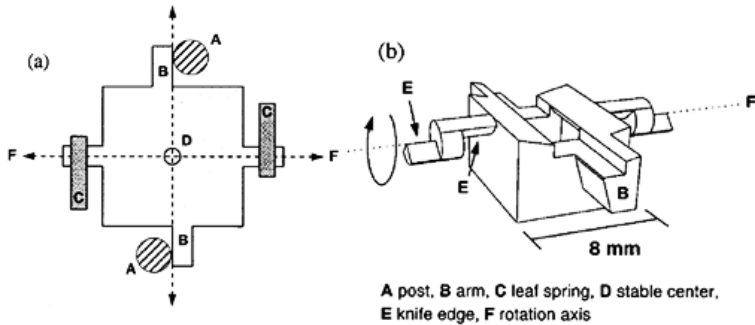


Fig. 2.2 Schematic top view of the sample holder body. The center circle D denotes the point from which all the lateral expansions are directed outwards. (b) A perspective drawing of the sample holder. The sample holder can rotate around the axis F, defined by the knife edges E. (from ref. [33])

In addition to the drift-minimizing mechanical design, the STM electronics have been optimized to scan fast. It has been demonstrated that the STM can image surfaces at video rate (24 frames per second) [34] (A commercial version of this instrument is marketed by Leiden Probe Microscopy BV, www.leidenprobemicroscopy.com). Because of the critical experimental conditions, in particular the high temperatures during deposition, video-rate scanning is very difficult. Therefore, the high-speed capabilities of the VT-STM have not been exploited directly in the work described in this thesis. On the other hand, the low noise level that the high-speed electronics has at low frequencies and the modular design of the electronics provided stable scanning conditions plus possibilities for customization of the scans, which played an important role in this work.

2.1.3 The heating of the sample

There were several requirements on the heating system of the sample. The experiments in this thesis required stable elevated sample temperatures up to 1200 K. The cleaning of the Rh sample required a maximum temperature of 1300 K. The surroundings should be kept at a relatively low temperature in order to maintain a low degassing rate and, thus, a low rate of contamination on the sample. Finally, the lifetime of the heating system needed to be long, in order to enable routine, long-duration experiments at high temperature.

A sketch of the sample heating system is shown in Fig. 2.3. We chose to use a tungsten filament with which we could heat the sample both by thermal radiation and by electron bombardment. The heating efficiency was optimized by a quartz tube (part C) that was placed around the filament. The quartz tube reduced the thermal radiation from the filament to the sample holder, so that the sample holder remained colder while the sample was hot. Sublimation of tungsten from the filament led to a conductive coating on the inner side of the tube, which was not connected conductively to the sample or the metallic components of the sample holder. Therefore, during electron bombardment, when the filament was biased to a high, negative voltage of typically -600 V, while the sample was held at ground potential, the metal film in the tube charged up negatively. This made the tube act as a lens, focusing the electrons that were emitted by the filament, onto the sample, which improved the heating efficiency of the sample, while reducing the heat load on the holder. During the mounting of the sample holder, the transparent quartz tube made it easier to place the filament as close as possible to the sample, which also increased the efficiency of the thermal radiation heating. A small tantalum spring (part F) was positioned between the quartz tube and the sample, to accommodate the thermal expansion difference between the tube and the Mo sample holder. The inner scale of the spring was larger than the inner diameter of the tube, so that the metal deposited from the filament would not make a short circuit between the filament and the sample. For the same purpose, a ceramic part E was used to hold the tube and the sample, and provided insulation between the filament and the parts at ground potential. Using this sample holder, the sample could be heated from room temperature to 1300 K in 10 seconds. Experiments in which the sample was held at 1000 K or higher for hours, while the background pressure in the UHV chamber stayed below 5×10^{-10} mbar, became a routine.

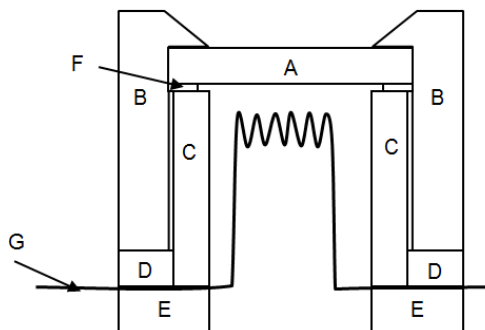


Fig. 2.3 A sketch of the heating system for the sample. A sample; B Mo sample holder; C quartz tube; D insulating ceramic parts; E a larger ceramic part which holds the quartz tube; F springs to accommodate the thermal expansion difference between C and B; G filament.

In our experiments it proved to be of crucial importance that the measurement of the sample temperature was accurate (within 5 K) and reproducible (within 1 K). For example, it was by virtue of our reliable temperature scale that we could identify the narrow temperature window of about 40°C in section 8.2, in which graphene is formed and carbide is not. In Chapter 6, the disappearance temperature of the nanomesh overlayer was determined twice, in two separate experiments, in both cases resulting in precisely the same temperature of 1160 K. In practice, we found that accurate measurements of the sample temperature were not straightforward. For example, when the Rh sample was heated to 1000 K, even the part of the Mo sample holder that was directly touching the sample, responded with a significant time delay and when it reached its final temperature it was still approximately 300 K colder than the sample. We paid specific attention to four aspects to achieve the required quality of the temperature measurement. First of all, the temperature measurement was performed by use of a K-type thermocouple directly on the Rh sample. Secondly, in order to avoid a temperature difference between the sample and the junction of the thermocouple, the two wires of the thermocouple were connected separately to the Rh, each onto one of the edges of the sample. Third, in order to make sure that the ends of the thermocouple wires were really at the temperature of the sample, the connections were made by spot welding, which was performed by use of a laser spot welding machine. Finally, the pins and sockets,

used for connecting the thermocouple wires between the sample holder and the support block and the wires running between the sockets on the support block and the feedthroughs on the UHV chamber were all made out of the appropriate K-type thermocouple materials, in order to properly define the reference temperature with respect to which the thermovoltage was measured, irrespective of the slowly drifting temperature of the passively heated support block.

2.2 The Rh(111) sample

A clean Rh sample formed the essential starting point for well-defined experiments, as presented in this thesis, for both the projects of graphene growth and of nanomesh growth. Because most of the experiments required elevated temperatures, where rapid diffusion can make near-surface contaminants segregate to the surface, the Rh sample should not only be clean at room temperature, but had to stay clean even at elevated temperatures, throughout the entire experiment.

The Rh single crystal was purchased from Surface Preparation Laboratory™, where it had been aligned by use of Laue diffraction to within 0.1 degree of the (111) orientation, spark eroded to dimensions of 4.8 x 4.8 x 1 mm³, and mechanically polished. In the UHV chamber, the (111) surface of the Rh sample was cleaned by cycles of Ar⁺ ion sputtering, followed by flash annealing to 1300 K. Then the sample was exposed to 2 - 3 × 10⁻⁷ mbar O₂ for 1 to 2 hours, at a temperature of 700 to 800 K; this latter step proved necessary, for removal of carbon surface contamination, defusing from the bulk. Residual O was removed from the Rh surface by flashing the sample to 1000 K [73]. The Ar⁺ sputtering was performed with the focused sputter gun (see section 2.1.1), at a current of 280 nA and a energy of 800 eV, for 30 to 45 minutes. Although cycles of sputtering and annealing can remove most of the contaminants in the near-surface region of the sample, the total amount of carbon in the sample is hardly changed. Delouise et.al. already reported that the carbon remnants in Rh can form a graphite structure during annealing, and that this graphite can then be reacted away by oxygen at elevated temperatures [73]. This process has been followed by STM (one example can be found in Chapter 12.). When the surface of Rh was fully covered by graphene, the oxidation reaction of the carbon was very slow. If there were uncovered Rh areas, the reaction took place at the

edges of the graphene, with a very noticeable speed. When the surface was fully covered by graphene or by graphite, Ar^+ ion bombardment introduced defects in the overlayer, from which the oxidation reaction could proceed. As shown in Chapter 13, we also learned that the elevated temperature was necessary for carbon diffusion from the bulk to the surface. When the concentration of carbon adatoms on the Rh surface exceeded a critical value, graphene or carbide islands could form on the surface. After nucleation of such islands, carbon atoms that segregated from the bulk to the surface contributed only to further growth of these islands. This process decreased the carbon concentration in the bulk material. This is also why annealing at 1300 K was necessary, before oxygen treatment, to make dissolved carbon atoms segregate to the surface and become incorporated in graphene or another carbon-containing surface species, where they could be removed by oxidation. In the beginning of the cleaning process, even brief annealing at 1000 K was sufficient to bring one layer of carbon to the surface, as indicated by AES. After tens of cleaning cycles, the quality of the sample was checked by LEED, AES, and more importantly, by STM. Although STM does not have elemental resolution, a clean STM image, without local protrusions or depressions and without pinning or decoration of the steps, provided very strong evidence for the cleanness of the sample. Furthermore, we tested the sample during heating up to the experimental temperature, for times that were comparable to those that were needed for one measurement. This provided the experiments in this thesis with a very well-defined substrate.

2.3 The moiré patterns

Because of lattice mismatch between graphene or *h*-BN and Rh(111), moiré patterns appeared in the STM images of *h*-BN and graphene. The moiré pattern behavior could be used as a magnifier of lattice defects, allowing us to get atomic information, even without always actually having atomic resolution. Obtaining atomic resolution with an STM is a serious challenge at high temperatures, which makes moiré patterns a very useful tool. To translate the moiré pattern to an atomic model, one of the easiest ways is go to reciprocal space [74]. The moiré pattern resulting from the combination of two hexagonal lattices, with different periods and different orientations, is also a hexagonal lattice. If \vec{k}_1 and \vec{k}_2 both designate one of the principal reciprocal lattice vectors of the

2.3 The moiré patterns

two hexagonal lattices, we can immediately obtain one of the principal reciprocal lattice vectors \vec{k}_m of the moiré pattern as their difference

$$\vec{k}_m = \vec{k}_1 - \vec{k}_2 . \quad \text{Eq. 2.1}$$

With this, one can easily calculate that the apparent rotation angle α between the moiré pattern and the Rh(111) lattice and the actual rotation angle β between the lattice of the *h*-BN or graphene overlayer and the Rh(111) substrate are related via

$$\sin \alpha = \frac{d_1 \sin \beta}{\sqrt{d_1^2 + d_2^2 - 2d_1d_2 \cos \beta}} \quad ; \text{Eq. 2.2}$$

d_1 is the lattice constant of the overlayer and d_2 is the lattice constant of the Rh(111) substrate. The moiré pattern lattice constant (d_m) is

$$d_m = \frac{d_1d_2}{\sqrt{d_1^2 + d_2^2 - 2d_1d_2 \cos \beta}} \quad . \text{Eq. 2.3}$$

Note here the moire lattice does not necessarily corresponds to a rational fit between the two lattices. In most cases, the lattices do not precisely coincide at regular distances. Only for special ratios between lattice constants and for special angles will the combined 2-lattice system be really periodic with the periodicity of the moire lattice. However, the calculated d_m and α still represents a beating pattern between the two lattice, which can still be measured by for example STM.

Due to the six-fold symmetry of *h*-BN and graphene, the geometry of the overlayer and the moiré pattern is the same when the rotation angle β of the overlayer is changed by integer multiples of 60°. In our calculations we therefore restricted the range of β to the interval between -30° and 30°. Due to the symmetry of the substrate there is an intrinsic $n \times 60^\circ$ ambiguity in the principal lattice direction of the substrate with respect to which the moiré pattern rotation has to be specified. As a result of this, we also present the calculated moiré pattern orientation angles α in the interval between -30° and 30°. The calculated relations between the rotation angle β of the overlayer and the orientation α (Eq. 2.2) and lattice constant d_m (Eq. 2.3) of the moiré pattern are shown for *h*-BN and graphene in Fig. 2.4 and Fig. 2.5, respectively.

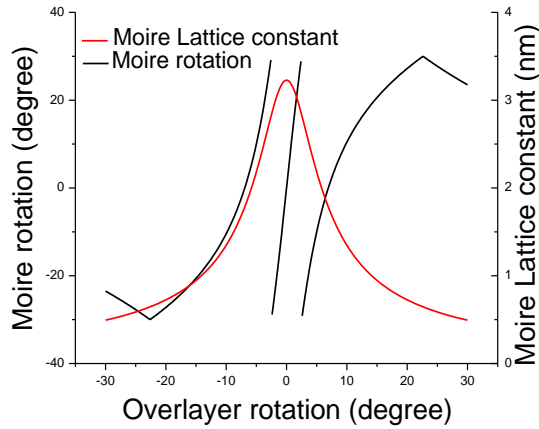


Fig. 2.4 Relation calculated between the overlayer rotation angle β and the orientation angle α (black curve) and lattice constant d_m (red curve) of the moiré pattern for *h*-BN on Rh (111).

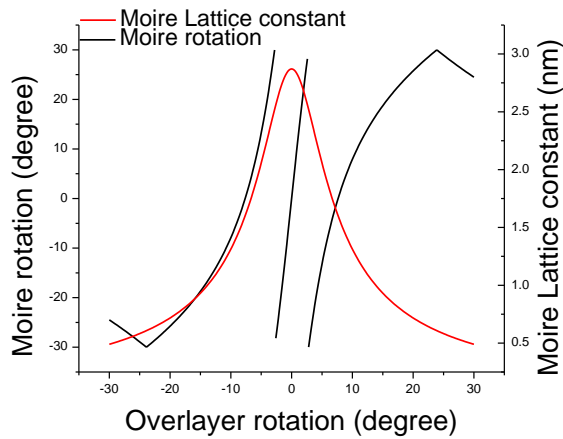


Fig. 2.5 Relation calculated between the overlayer rotation angle β and the orientation angle α (black curve) and lattice constant d_m (red curve) of the moiré pattern for graphene on Rh (111).

2.3 The moiré patterns

The two figures show that the rotation of the overlayer is amplified very much by the moiré pattern, but that the mere measurement of the rotation angle α of a moiré pattern is not enough to derive the rotation angle β of the overlayer.

Moiré patterns also amplify translational errors of the overlayer. If a patch of graphene or *h*-BN is translated over a distance \vec{S} with respect to the original position, the accompanying displacement of the moiré pattern \vec{M} is:

$$\vec{M} = -\frac{L_m}{L_o} \vec{S} \quad \text{Eq. 2.4}$$

Here, L_m and L_o are the periodicities in the \vec{S} direction for the moiré pattern and the overlayer, respectively. Because L_m is larger than L_o , translational errors are amplified by the moiré patterns by a factor of $L_m/L_o > 1$.

Part I

Nanomesh formation on Rh (111)

Chapter 3 Introduction of part I

3.1 Background

On the Rh(111) surface, hexagonal boron nitride (*h*-BN) adopts a highly regular superstructure, with 2 nm diameter depressions and a 3.2 nm period. Similar structures are found on other metal surfaces. This so-called *nanomesh* [6] serves as a two-dimensional scaffold for deposition of bucky balls and other, functional molecules [6, 18], which may lead to interesting e.g. electronic, magnetic, or catalytic properties and applications. The nanomesh coating has been demonstrated to remain intact under ambient conditions [12], in liquids [19], and at high temperatures [6], thus protecting the underlying metal. The combination of *h*-BN and graphene provides opportunities for sophisticated band gap engineering in the graphene [75-77] and for advanced device development [78]. The atomic structure of the nanomesh has been unraveled, by a combination of Scanning Tunneling Microscopy (STM) [6, 14], surface X-ray diffraction (SXRD) [12], and theoretical calculations [10, 11]. It is a single, highly corrugated layer of *h*-BN, with 13×13 unit cells of the *h*-BN lattice fitting onto 12×12 unit cells of the underlying Rh(111) surface.

In view of the large super-cell, containing 338 overlayer atoms, the superb quality of the observed nanomesh patterns is quite surprising. The procedure, originally introduced by Corso *et al.* for the deposition of a nanomesh film, is to expose the Rh(111) surface to borazine (HBNH_3)₃ gas at 1050 K [6]. What is the role of this high temperature? It could be that a high temperature is necessary to crack the borazine molecules, releasing hydrogen, and possibly rupturing B-N bonds, in order to form reactive precursors, which stick sufficiently strongly to the surface and serve as the growth units, from which the overlayer can be assembled. One can also imagine that a high temperature would be required to provide sufficient lateral mobility for crystallizing the otherwise disordered

overlay into the perfectly periodic nanomesh structure. While the high temperature serves as an important clue, it also poses a significant experimental difficulty.

3.2 Experimental methods

All measurements were carried out under ultrahigh vacuum (UHV), with a variable-temperature STM setup, which allowed fast scanning and imaging over a wide range of temperatures and during substantial temperature changes [33, 34]. The base pressure of the system was 1.5×10^{-11} mbar. All pressures, including that of the borazine gas, were measured with an ion gauge, without considering the differences in the sensitivities for the different gases. Sample temperatures were measured by a K-type thermocouple, spot-welded directly onto the Rh single crystal. The crystal was heated from the rear side by a filament, using either by thermal radiation or by electron bombardment, extracting electrons from the filament and accelerating them through a voltage of -600 V between the filament and the sample. This allowed the sample to be heated from room temperature to 1300 K in 10 seconds. The Rh sample was cleaned by cycles of Ar^+ ion sputtering, followed by flash annealing to 1300 K, and exposure of the sample to 2 to 3×10^{-7} mbar of O_2 for 1 to 2 hours, at temperatures of 700-800 K. The latter step proved necessary for removal of carbon surface contamination, which segregated out of the bulk. Residual O was removed from the Rh surface by flashing the sample to 1000 K [73]. After having repeated this cycle at least 10 times, no C contamination could be detected by Auger Electron Spectroscopy, and the density of visible impurities in the STM images was typically below $1/\mu\text{m}^2$. High-purity borazine, $(\text{HBNH})_3$, was gratefully obtained from the group of Prof. Hermann Sachdev at the University of Saarland in Germany and was deposited in the UHV-system from a dosing nozzle, that stored the material at a reduced temperature, by means of a Peltier cooler, and allowed it to warm up for deposition purposes. The cooling/dosing system was thankfully received from Prof. Jürg Osterwalder and Prof. Thomas Greber from the University of Zurich in Switzerland.

Most of the measurements in this part consist of in-situ STM imaging, namely at elevated temperatures and during deposition. By this method, one can achieve direct observations, which are far easier for understanding the mechanisms than images or other measurements carried out after completion of the growth procedure. However, the

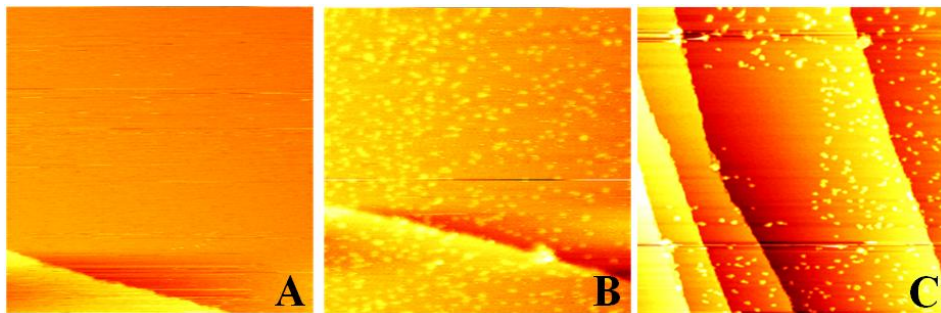


Fig. 3.1 Examples of the influence of the tip on the borazine deposition: (A) A Rh surface being scanned by STM, during borazine deposition. No deposits are visible on the surface. The feature at the bottom of the image is a monoatomic step on the Rh substrate. (B) An equally large region directly on the left-hand side of area that was scanned during deposition (image A). After deposition, many adsorbed borazine molecules are visible in this image. Notice the gradient in density from right (where the tip had been) to left. (C) A zoomed out STM image, after the Rh surface had been dosed with 0.2 L of borazine at room temperature and annealed to 576 K. Small clusters had been formed during the annealing. The image shows that the clusters have been removed from the central region by the STM tip. The imaging conditions for the central region of panel C had been the same as the imaging conditions for the zoomed-out scan of panel C itself.

The image sizes of panels A and B are $85 \times 85 \text{ nm}^2$, while that of panel C is $200 \times 200 \text{ nm}^2$. Sample voltage: $V_b = 2.5 \text{ V}$, 2.0 V , and 1.7 V , for fig. A, B, and C, respectively. Tunneling current $I_t = 0.05 \text{ nA}$.

presence of the STM tip may influence the deposition. In particular, it can shadow off the portion of the surface that is being imaged, thus making the local deposition rate lower than the average rate. In the present work, it was found that the STM tip sometimes completely blocked the deposition of borazine molecules. For example, in Fig. 3.1, after 0.2 L (1 Langmuir = 10^{-6} torr s) of borazine exposure, the area that was scanned by the STM was still completely clean (panel A), while the direct surroundings had very noticeable amounts of borazine adsorbed (panel B). In addition to being an obstacle for the impinging molecules, the tip can also act as a ‘vacuum cleaner’, emptying the scanned area, even when it is covered already by adsorbed borazine molecules or clusters. Such effects may be particularly strong at elevated temperatures. An example of this tip-induced ‘cleaning’ can be found in Fig. 3.1C. Occasionally the tip switched spontaneously from the ‘cleaning’ configuration to normal behavior, in which it did not influence the surface, suggesting that the ‘cleaning’ did not depend on sample voltage or

3.2 Experimental methods

tunneling current but on the configuration details of the tip. A possible explanation for this is that the 'cleaning' results from the interaction (Van der Waals or electrostatic) of the full tip with the borazine. If the structure of the very apex of the tip changes in such a way that it protrudes less far from the body of the tip, this interaction is significantly increased, thus possibly switching on the 'cleaning' effect, seemingly without significant changes in imaging quality.

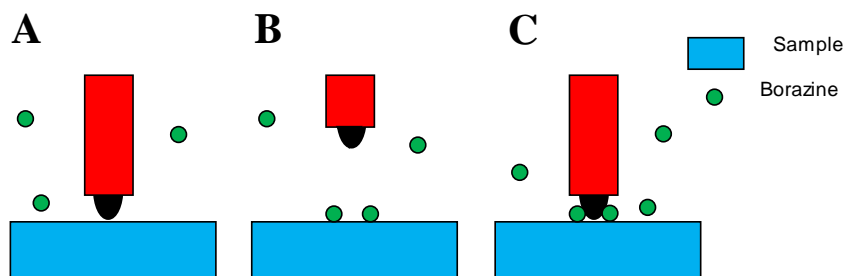


Fig. 3.2 Sketch of the tip retraction procedure. During STM imaging, borazine molecules sometimes cannot reach the scanned area because of geometrical blocking by the STM tip (A). In such cases we adopted the procedure to retract the tip during one entire image period (B), so that borazine could reach the sample surface. After this the tip was returned to the measurement position, to acquire a single STM image. This (B)/(C) procedure was repeated throughout the entire deposition.

The blocking of the borazine deposition made it very difficult to perform STM measurements during deposition. Fig. 3.2 shows our method to circumvent this problem when it presented itself. The STM tip was retracted between subsequent STM frames for the duration of an entire STM frame. This meant that there was an empty image between every two scanned images. During the empty imaging, the borazine could reach the scanned area and react, so that this procedure effectively reduced the borazine exposure by a factor 0.5 (or slightly above 0.5) with respect to completely unhindered exposure. One disadvantage of our retraction procedure is the significant creeping of the piezo-electric scanner that follows after each substantial change in position. Even though the retraction (and re-approach) were directed along the z-direction, perpendicular to the surface, also the x- and y-position was found to exhibit a strong creeping effect that lasted for typically 30 minutes after the last re-approach. This creeping made it difficult to

relocate the original area that had been in view before a retraction–re-approach cycle. In addition, in the slow scan direction the creeping resulted in a nonlinear elongation of the image, which introduced the risk of large errors in the counting of the areas of islands or vacancies. Fortunately, the growth of the nanomesh structure was observed to follow a very specific mode, in which the growth unit was precisely equal to one complete unit of the nanomesh pattern, corresponding to 169 units of the BN overlayer. Usually the area of the growing *h*-BN could be identified just by counting the additional nanomesh units.

3.3 This part of the thesis

In this part of the thesis, we concentrate on the assembly of *h*-BN nanomesh films on Rh(111) by *in-situ* STM observations under the reported growth conditions, i.e. *during* borazine deposition, at temperatures up to 1200 K. Experimental procedures are provided in section 3.2. In the same section it will also be pointed out that the STM tip can block the borazine molecules from landing on the surface of the sample. A method will be introduced for avoiding such a tip influence. In Chapter 4, the behavior of *h*-BN and borazine at different temperatures will be investigated by deposition of borazine at various temperatures. The growth unit is found to be one entire unit cell of the nanomesh pattern. We will also consider the different edges (boron terminated and nitrogen terminated) of the nanomesh islands and we will discuss the energy barriers for growth on different sites in section 4.4.4. In Chapter 5, the adsorption of borazine and the temperature needed for its decomposition will be discussed. Chapter 6 will concentrate on the formation and stability of defects in the *h*-BN nanomesh. Based on this, we can understand why a high deposition temperature is needed for a high-quality nanomesh structure and an optimal growth recipe will be derived.

Chapter 4 Nanomesh formation at different temperatures on Rh(111)

4.1 Introduction

The procedure, originally introduced by Corso *et al.* for the formation of a nanomesh film, is to expose the Rh(111) surface to borazine (HBNH)₃ gas at 1050 K [6]. The temperature seems to be an important parameter, as mentioned in section 3.1. In order to investigate the influence of the temperature on the formation of the *h*-BN nanomesh structure, borazine (HBNH)₃ was deposited at various temperatures onto Rh(111). In addition to this, we also investigated the evolution of the overlayer with temperature after the deposition by heating the sample to higher temperatures while imaging the surface continuously by STM.

4.2 Nanomesh formation from borazine deposited at room temperature

We first exposed a cleaned Rh(111) surface to 4×10^{-5} mbar s of borazine at room temperature. This pre-exposed surface was heated up slowly, from room temperature to ~1060 K, while STM images were taken continuously. Selected images from this measurement are shown in Fig. 4.1A complete STM-movie, from 295 to 1057 K, is available online [79]. At 690 K, the first noticeable rearrangements into small, nanometer-scale clusters were observed. As the temperature increased further, these small clusters became mobile, and coalesced. The branched and elongated shapes, observed in Fig. 4.1B, are characteristic of a diffusion-limited type of aggregation (DLA)

[80]. Within the individual clusters, distinct height variations were seen, with a typical amplitude of 0.05 nm (Fig. 4.1B). This indicates that these were not mere clusters of borazine molecules, but that instead, the clusters already had the *h*-BN structure, with a thickness of a single monolayer and with the corrugation resulting from the mismatch with the underlying Rh lattice. In Fig. 4.1C, it can be seen that, at a high temperature of 1007 K, the shapes of the islands had become more compact, and the height variations had organized into the nanomesh superstructure, albeit with a high density of defects. When the temperature was further increased to 1042 K, most of these defects disappeared, and the islands ripened to larger sizes (Fig. 4.1D). The images in Fig. 4.1B-D clearly show that the total coverage was well below that corresponding to a full *h*-BN nanomesh monolayer, even though the initial exposure of 40 L had been sufficient to reach the maximum coverage at room temperature. What these images also indicate is that there was, at most, a minor loss of material (borazine or BN) from the surface. This implies that almost all the B- and N-atoms deposited at room temperature were still present at 1042 K, and that their numbers added up to no more than a 50% monolayer of *h*-BN. Two potential causes for this lack of material are (i) that, at room temperature, the borazine molecules formed a highly disordered, and therefore, non-compact layer (Fig. 4.1A), and (ii), that with most of their hydrogen atoms still present, the borazine molecules, initially present at room temperature, required more space than that occupied their B- and N-atoms, after hydrogen desorption, in the final *h*-BN structure. From this first experiment, we conclude that the typical deposition temperature of 1050 K is not necessary for borazine adsorption or *h*-BN formation. Furthermore, it was observed that the overlayer was formed via two-dimensional nucleation and growth.

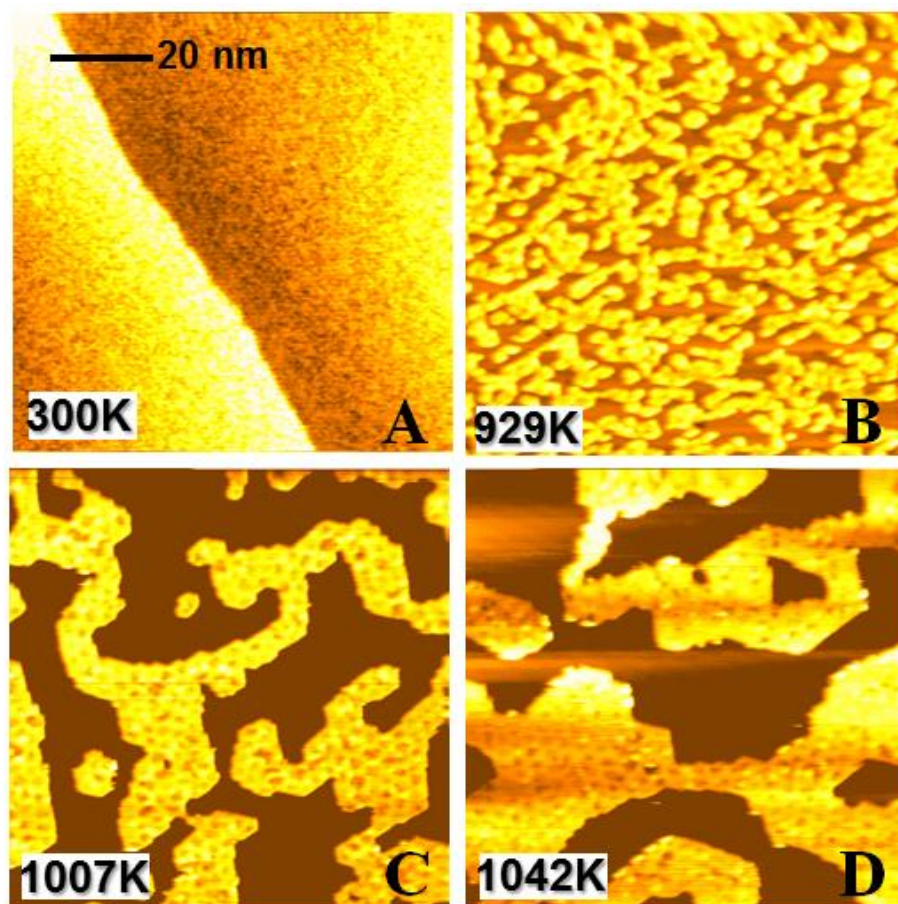


Fig. 4.1 A series of images selected from the STM Movie 1 [79], during a continuous temperature ramp from 300 K to 1057 K of a borazine-pre-exposed Rh(111) surface. (A) The Rh surface directly after exposure to 40 L of borazine gas at room temperature. A monatomic step on the Rh surface crosses the image. The rough appearance of the upper and lower terraces is caused by the borazine deposit. (B) At higher temperatures, the overlayer first organized into narrow, somewhat elongated islands of *h*-BN. The height variations within the islands result from the mismatch between the lattice constants of the overlayer and the substrate. (C) The next stage was the formation of more compact *h*-BN islands, with a defective nanomesh superstructure. (D) At the final temperature, the nanomesh structure was relatively well-defined.

All images are 85 nm × 85 nm, and have been taken at a sample voltage of $V_b = 3.0$ V and a tunneling current of $I_t = 0.05$ nA.

4.3 Nanomesh formation from borazine deposited between 627 K and 865 K

As suggested by the fractal-like island growth patterns in Fig. 4.1B, after pre-exposure of the Rh substrate to borazine at room temperature, the initial *h*-BN islands are formed by diffusion-limited aggregation [80] of individual borazine molecules or small borazine clusters. Next, we address the role of the substrate temperature during the exposure. For this, we exposed the substrate to borazine at 627 K. After 10 minutes at a pressure of 3.7×10^{-10} mbar, the STM images showed no sign of either borazine adsorption or *h*-BN formation. A significantly higher pressure of 1.5×10^{-9} mbar was required to obtain the first stages of island formation; Fig. 4.2A shows an example at a somewhat higher pressure of 3.2×10^{-9} mbar. While the terraces exhibited a low density of nuclei, the steps on the Rh substrate were saturated by small islands. The shapes of these islands were again fractal-like. No corrugation was observed on the islands, which means that they did not yet have the structure of *h*-BN. Then we increased the sample temperature. Whereas at 762 K the islands still retained their fractal shapes, at 806 K they had become compact (Fig. 4.2B). In addition, as we will discuss in more detail in section 5.1, the orientations of the island edges indicate that in this temperature window the island rearrangements had involved the breaking of B-N bonds. Fig. 4.2B further illustrates that at 806 K the *h*-BN islands did not merely occur at steps of the Rh substrate. The islands displayed a variety of orientations, the preferred orientation being the one with the *h*-BN lattice, and therefore also the moiré pattern, aligned with the Rh(111) substrate.

On this *h*-BN seeded surface, with different orientations, further *h*-BN was formed by exposing the surface to borazine pressures ranging from 1.2×10^{-9} to 1.2×10^{-8} mbar, while the substrate temperature was held at 865 K. Fig. 4.2C and D show the same area before and after this extra deposition. They show that most of the additional *h*-BN closely followed the orientations of the 'seed' islands. At every location where two domains met, a domain boundary line or a defect line was formed between them. However, there were exceptions. For example, the domain indicated by the black arrow in Fig. 4.2D was newly formed at the connection between two differently oriented domains, suggesting that the mismatch between these orientations was so unfavorable, that in spite of the extra domain boundary length, the new domain could lower the total energy. Further evidence

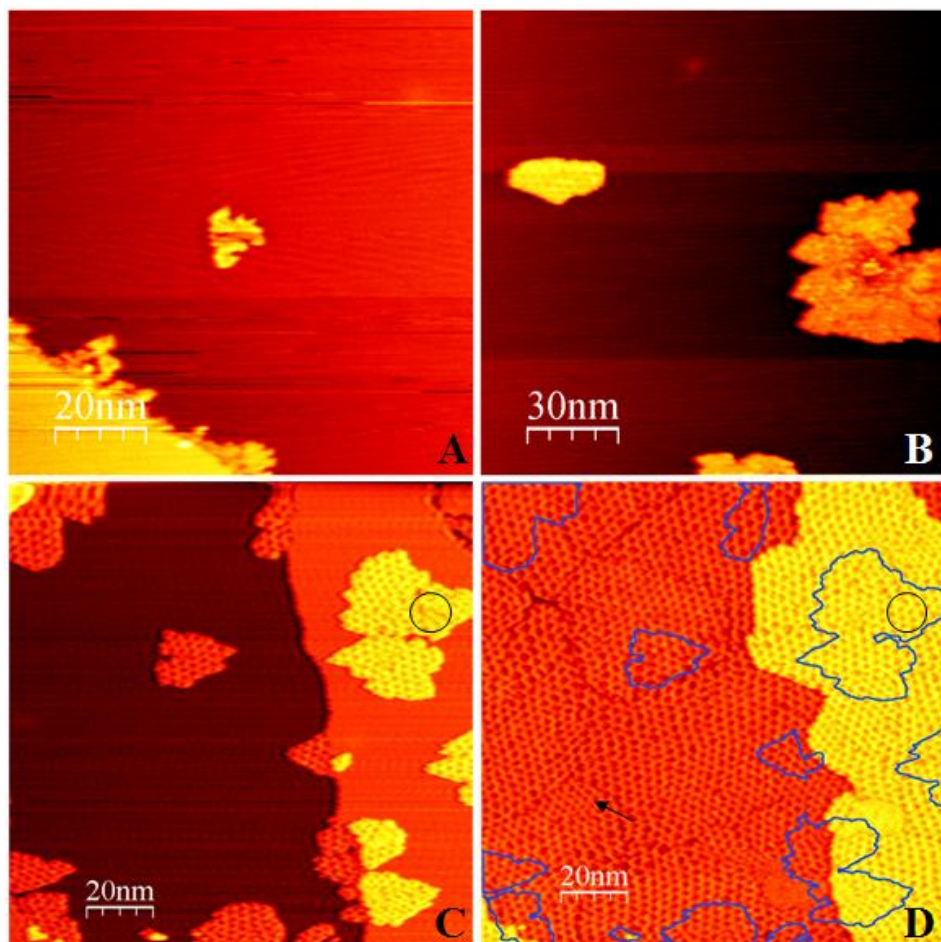


Fig. 4.2 (A) STM image of Rh(111) at 627 K, after having been exposed at that temperature to 3×10^{-9} mbar of borazine for 12 minutes. The Rh steps were saturated by small islands and the shapes of islands were fractal-like. (B) STM image after the temperature had been increased to 806 K. The *h*-BN islands appeared to be compact. Within each island, the nanomesh superstructure can be observed. The islands did not occur primarily at steps of the Rh substrate. (C) After a further temperature increase to 865 K, the islands had become more compact. (D) The same area as in panel C, after an additional borazine exposure at pressures ranging from 2×10^{-9} to 1.2×10^{-8} mbar for 78 minutes, while the temperature of the sample was held at 865 K. The surface was fully covered by *h*-BN with a variety of orientations. The blue lines indicate the contours of the initial islands in panel C. Most of the growth followed the orientations of these initial islands. The black arrow indicates a new domain that had formed during growth. In the circled part, defects had been removed that were still present in panel C. $V_b = 2.9, 2.8 \text{ V}, -1.0 \text{ V}, -1.0 \text{ V}$ for panels A – D, respectively, $I_t = 0.05 \text{ nA}$.

were present in the initial islands. For example, the defect marked by a circle in Fig. 4.2C was no longer present in Fig. 4.2D. Similar effects can be seen in Fig. 4.1. But the removal of defects occurred far less frequently than the formation of defect lines where different domains encountered one another. As a result, the completed *h*-BN overlayer contained a significant density of defects. A detailed discussion of these defects will be given in Chapter 6.

4.4 Nanomesh formation from borazine deposited at 978 K

In section 4.2 we concluded that the typical deposition temperature of 1050 K of *h*-BN on Rh(111) is not necessary for borazine adsorption or for *h*-BN formation. Furthermore, we saw that the overlayer formed via two-dimensional nucleation and growth. Due to the procedure adopted in section 4.2, where the borazine was deposited at room temperature and the substrate was subsequently heated, the resulting structure was far from a perfectly regular nanomesh. In order to find out what really limits the quality of growing nanomesh films, it was necessary to perform STM observations *during* borazine exposure close to the reported optimal nanomesh formation conditions (e.g. 1050 K [6]). Exposing a clean Rh(111) surface to borazine at 978 K, we verified that, also at such a high temperature, the overlayer assembled via the two-dimensional nucleation-and-growth mode, in this case, with compact and well-separated *h*-BN islands that immediately adopted a regular nanomesh structure. However, under these conditions, the average density of the islands was so low, e.g. 3 islands/ μm^2 , that it was difficult to capture the interesting stages of the process in well-resolved STM images. Therefore, the nucleation density was artificially increased by a seeding procedure, which consisted of first exposing the Rh surface to a low dose of 0.2 L borazine at room temperature, followed by a heating step to 978 K, which resulted in the formation of a comfortable density of 250 islands/ μm^2 of small *h*-BN islands (Fig. 4.3A). On this seeded surface, we continued the borazine exposure at 978 K, while imaging continuously by STM.

4.4.1 The growth unit

The first thing that was noticed was that the growth appeared to proceed by the addition of entire nanomesh units, or by rows of nanomesh units. This discretization of the growth process in nanomesh units is illustrated by Fig. 4.3B and C. (The movie can be found in [79]) Although this growth mode may seem natural at first sight, it is rather surprising, since each nanomesh unit contains 169 B-atoms and 169 N-atoms. A more careful inspection of the images revealed the presence of a highly mobile species at the edges of the *h*-BN islands. We interpret this as BN diffusing along the island perimeter, until it locally accumulated into a new, complete nanomesh unit cell. At this point, the atoms in this nanomesh unit were effectively immobilized in their new structure.

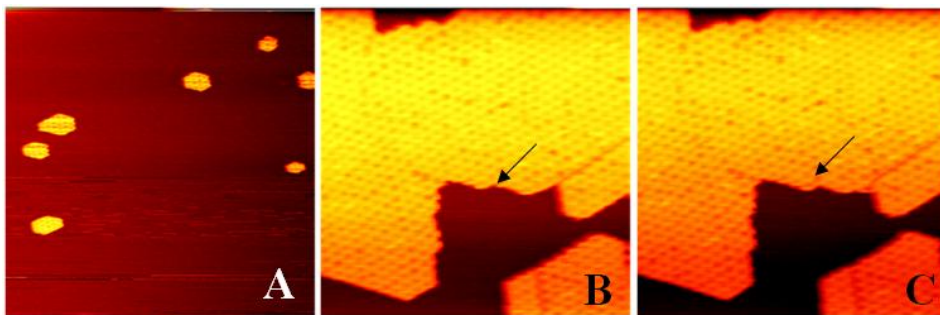


Fig. 4.3 (A) Rh(111) pre-seeded with nanomesh islands, by exposure to 0.2 L of borazine at room temperature, and subsequent annealing at 978 K. In this way, the nucleation density was artificially increased with respect to the natural density at 978 K. (B, C) Two subsequent STM images (17.5 s each) at 978 K during nanomesh growth on the pre-seeded surface at a borazine pressure of 3×10^{-9} mbar. As indicated by the arrow in (B) and (C), the growth unit here is one nanomesh unit. Image size: (A) $170 \times 170 \text{ nm}^2$, (B) and (C) $85 \times 85 \text{ nm}^2$, Sample voltage: $V_b = 1.0 \text{ V}$. Tunneling current $I_t = 0.05 \text{ nA}$.

4.4.2 Nanomesh island shape

After the pre-seeded Rh sample had been annealed at 978 K (see previous section), the observed equilibrium island shape (Fig. 4.4A) was a quasi-hexagon, with three short and three long edges, corresponding to a higher-energy and a lower-energy termination of the island, respectively. The shape of the islands is the two-dimensional Wulff shape [81]. We associate the difference with the two different ways the edges can be terminated:

either with B atoms or with N atoms. In ref. [24], the lower-energy edge on Ni(111) was speculated to be N-terminated. The ratio E_L/E_H between the (free) energies of the two edges can be calculated from their length ratio to be 0.9 ± 0.1 .

4.4.3 Nanomesh growth along different edges

When borazine was deposited, the island rapidly evolved into a (truncated) triangular growth shape (Fig. 4.4B). New nanomesh units formed naturally at kinks, which made these kinks advance along the island perimeter (Fig. 4.4). Although the kinks were found to advance with equal speeds along the two types of edges, the rates at which new kinks formed were different. The low-energy (longer) edges formed fewer kinks per unit length and time than the high-energy (shorter) edges. This is why the inequivalence between the two types of edges was emphasized by the growth, making the growth shape deviate even further from an equal-sided hexagon than the equilibrium shape from which the growth started. For a quantitative analysis we have used part of the seeding and growth experiments described in section 4.4.4. Images at the beginning and end of the analyzed episodes are shown in Fig. 4.6. Table 4.1 lists the kink creation rates measured for the short and the long edges of the island marked by the circle in panels A and B of Fig. 4.6. The table shows that the kink creation rates on the two types of edges differed by a factor of approximately 40, even though the bare Rh that surrounded this island was connected, so that the concentrations of BN experienced by all island edges must have been similar. The lower kink creation rate on the low-energy edge is easy to understand. The size of a complete nanomesh unit cell is so large, that the energy of a kink along a low-energy edge will be relatively close to the energy of one unit cell length of the high-energy edge (see the inset in Fig. 4.4C). Similarly, a kink along a high-energy edge will introduce an extra energy close to that for one unit cell length of the low-energy edge. The corresponding difference in kink energy will naturally make the kink creation rate lower on the low-energy edge.

On both types of edge, a kink can be regarded as a connection between a segment of high-energy and an equally long segment of low-energy edge. In view of this equivalence and of the fact that the energy is not changing with the position of the advancing kinks, we should expect the BN deposition to make existing kinks move equally fast along the two types of edges. Indeed, the measured rates at which kinks were observed to

advance along short and long edges were equal within the statistical error margin of the measurement, as shown in Table 4.1.

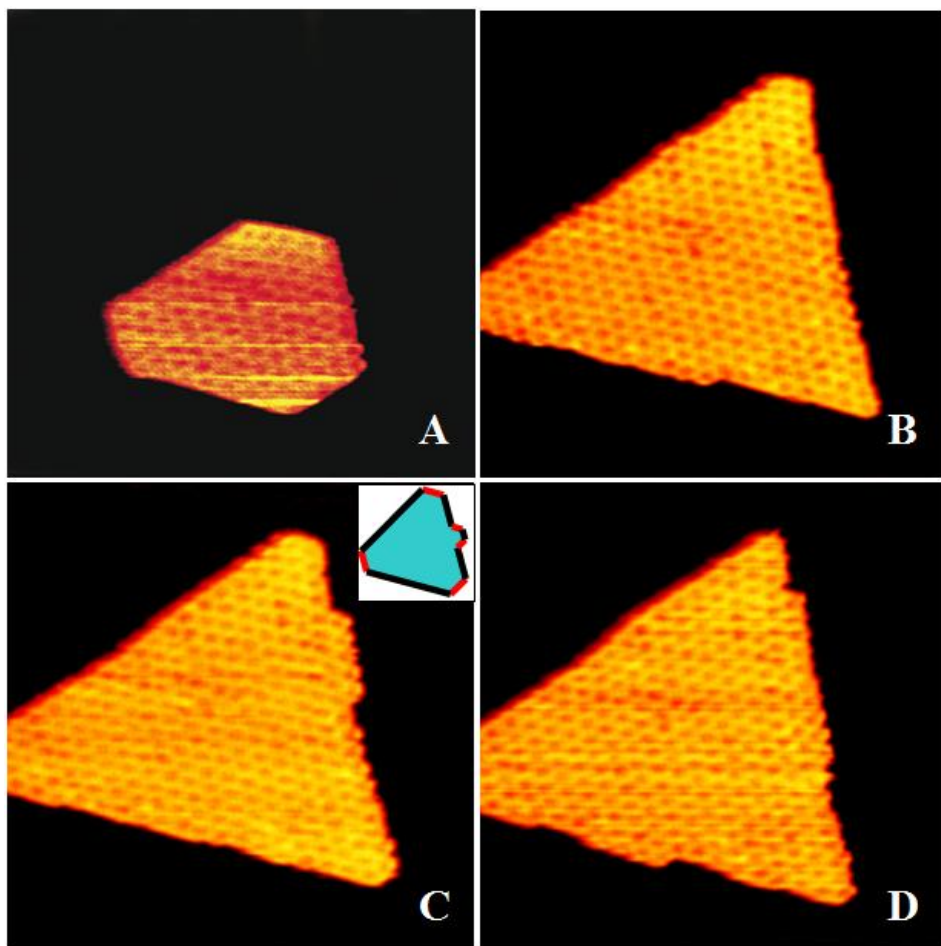


Fig. 4.4 STM images of an *h*-BN island, recorded at 978 K, while borazine was being deposited onto the Rh (111) surface; the images were selected from Movie 2 [79]. (A) The initial equilibrium island shape was obtained by exposing the clean Rh(111) surface to 0.2 L of borazine at room temperature, and subsequent annealing at 978 K. (B) Image after 368 s of borazine exposure at 2.5×10^{-9} mbar at 978 K; the island shape had become triangular, within the first 60 s. (C) After 421 s, new kinks had formed on the right edge, while the kink at the bottom edge had advanced to the right corner. The inset is a sketch, indicating the two types of edges, the red ones having the higher energy. (D) After 473 s, the two kinks on the right edge had advanced and new kinks had formed on the lower edge.

4.4.4 Growth barriers of the nanomesh structure at various sites

In this section, we use our STM movies to determine the growth rates of the nanomesh overlayer at various sites that play a special role in the growth process. The ratios between these rates allow us to determine the edge energies and corner energies of the *h*-BN structure.

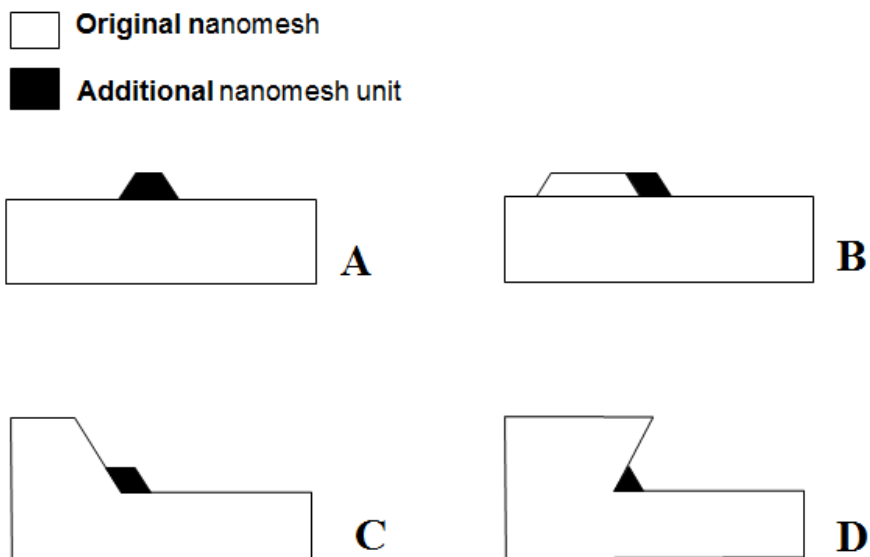


Fig. 4.5 Sketches of the essential steps in the growth of the nanomesh structure on different edge and corner sites. Note that the growth proceeds in complete unit cells of the nanomesh pattern. (A) Addition of the first unit cell of a new nanomesh row on a straight edge, involving the introduction of two kinks. This process costs less energy on high-energy edges, where the new unit introduces two additional low-energy edge segments. (B) advancement of an existing kink. The total edge energy remains unchanged in this process, so that it should have the same rate on low- and high-energy edges. (C) Addition of a nanomesh unit in 120° corner. . This process differs from kink advancement, because two additional corners are created by this process. (D) Addition of a nanomesh unit in a 60° corner.

In addition to the low- or high-energy straight edges (Fig. 4.5A, B), there are further sites from which the nanomesh structure can nucleate and grow. For example, Fig. 4.5C

sketches the filling of a 120° corner. Although this may look similar to the advancement of an existing kink (Fig. 4.5B), since no new edges are introduced, the nucleation in the corner does require the introduction of two extra corners, one concave and the other convex. This is reflected in the filling rate for 120° corners in Table 4.1, which is higher than the creation rate for new kinks on straight edges (both short and long), but lower than the rate at which kinks advance along straight edges. The filling rate for 120° corners was measured from the edges of the corner indicated by the circle in panels C and D of Fig. 4.6. These STM images were taken continuously, while the borazine pressure was kept at 3×10^{-9} mbar. The borazine pressures in the A-B and C-D series have been equal and also the kink advance rates measured in both series on the low-energy edges have been close to identical. This indicates that the BN concentrations have been similar for the two cases, which is why we can safely compare all rates from the two series in Table 4.1. Fig. 4.5D shows that the filling of a 60° corner replaces two low-energy sections by one high-energy section, provided that the edges of this corner are indeed low-energy edges. The measurement in Table 4.1 shows that this makes the filling rate for these corners somewhat lower than that for 120° corners. For completeness, we can also imagine a corner with two high-energy edges, but such a configuration would be filled very quickly, because two complete high-energy edges can then be replaced by one low-energy edge.

From the rates in Table 4.1, we can easily compute the differences in the activation barriers for the processes considered, according to the corresponding Boltzmann factors. For example, the ratio between two rates R_1 and R_2 provides us with the difference between the energy barriers E_1 and E_2 between processes 1 and 2, via $R_2/R_1 = e^{(E_1 - E_2)/k_B T}$. Here, T is the temperature of the sample, k_B is Boltzmann's constant and we have assumed the pre-exponential factors for the two processes to be identical. We justify the latter assumption in two steps. First of all, the processes considered in Fig. 4.5 and Table 4.1 all proceed in the same units, namely the units of the nanomesh pattern. Secondly, in the experiments used for the rate measurements, the borazine pressure was constant, and the measured growth rates did not change significantly with time, showing that the surface concentration of BN has been constant and equal for the different edges and corners. Since we can only determine energy differences from the ratios between the rates, the energy barriers in Table 4.1 are all expressed relative to the energy barrier for the fastest process, namely the advancement of a kink along a low-energy (i.e. long) straight island edge.

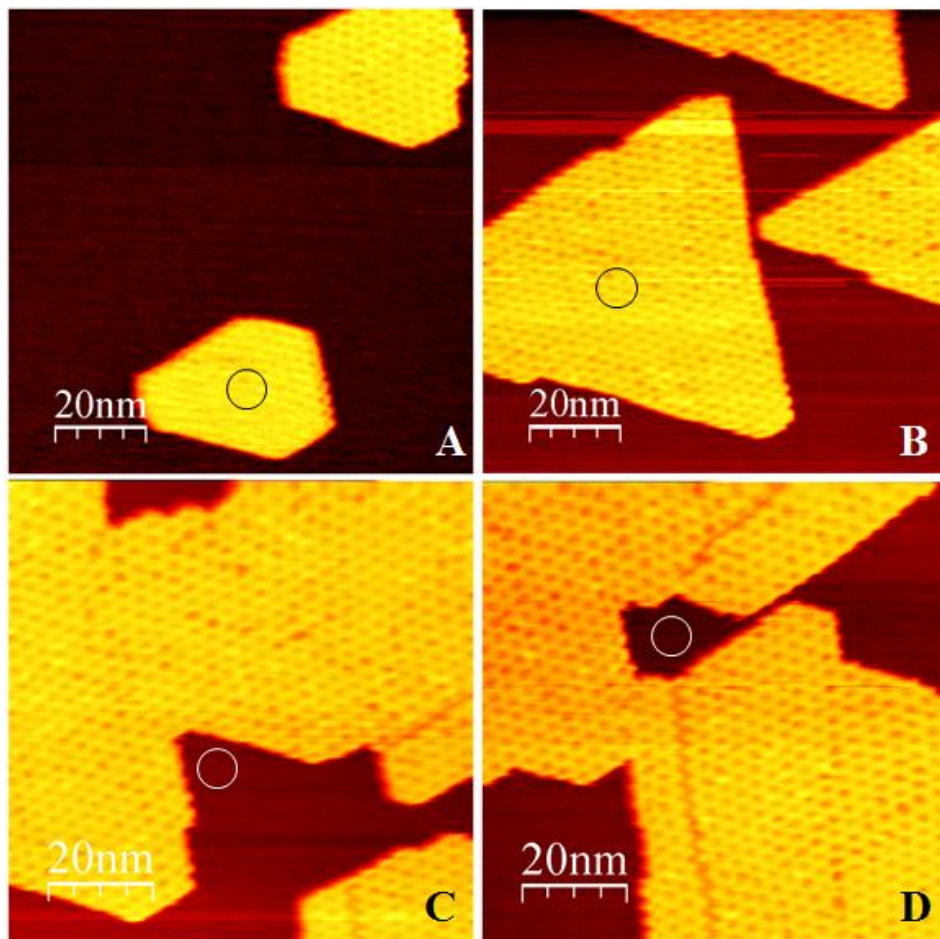


Fig. 4.6 First and last images in the two episodes (A-B and C-D) of an STM movie [79] of the high-temperature growth of the nanomesh structure on Rh(111) that have been used for the quantitative growth rate analysis. In A-B, the island marked by the circle was used. The Rh around the island was connected, so that the edges of the island were all exposed to the same densities of B and N atoms. In C-D, the growth rates of the edges around the circle were analyzed. The borazine pressure was 3×10^{-9} mbar and the sample was at 978 K.

Episode A-B was measured with 35 to 52.5 s per frame. Episode C-D with 17.5 s per frame. Image sizes were $100 \times 100 \text{ nm}^2$ for A-B and $85 \times 85 \text{ nm}^2$ for C-D. Sample voltage: $V_b = 1.0 \text{ V}$. Tunneling current $I_t = 0.05 \text{ nA}$.

	Rate (nanomesh units / site / second)	Relative energy barrier (eV)
Kink creation (short edges)	0.011 ± 0.002	0.15
Kink advancement (short edges)	0.058 ± 0.02	0.013
Kink creation (long edges)	0.00028 ± 0.00008	0.47
Kink advancement (long edges)	0.069 ± 0.008	0
120° corner filling	0.028 ± 0.005	0.077
60° corner filling*	0.019 ± 0.004	0.11

*

The data in the last line of the table were obtained on a 60° corner, accompanied by a domain boundary (see text)

Table 4.1 Rates of various basic processes involved in the growth of the nanomesh overlayer, measured at a borazine pressure of 3.0×10^{-9} mbar and at a temperature of 978 K. The margins reflect the statistical uncertainties. The energy barriers have been obtained from the rates using the procedure explained in the text and are expressed with respect to the energy barrier for the advancement of kinks along long (low-energy) edges.

The equality of the kink advancement rates of the different edge types shows that the corresponding activation energies have been equal to within statistical error, as expected (see above). The factor 40 difference in kink creation rate between the high- and low-energy edges shows, that the formation energy for a new kink is 0.32 eV higher on a low-energy edge than on a high-energy edge. Let us look in more detail at this difference. If we regard the edge of an *h*-BN island energetically as a straightforward sum of edge and corner energies, the energy involved in the addition of a ‘single-nanomesh-unit’ kink pair along a straight, low-energy island edge amounts to $2E_H - E_L + 2E_{-120} + 2E_{120} - 3E_{nm}/2 + \Delta E_{nm}^{kink-pair}$. In this expression, E_L and E_H are the (free) energies per unit length for the low- and the high-energy edges; for convenience we have expressed the length in units of the lattice constant of the nanomesh pattern. The energy change indicates that we are adding two kinks, i.e. two edge units of the high-energy orientation; but due to the 120° angles that these edge units make with the original edge, the total length of low-energy edge is reduced by one unit. E_{-120} and E_{120} are the corner energies for the two additional convex and the two additional concave 120° corners. E_{nm} is the amount by which the total (free) energy is lowered by the incorporation of 169 B and 169 N atoms in a unit cell of the *h*-BN structure. The factor 3/2 appears because the shape defined by

the two high-energy edges and one unit of the low-energy edge is actually 3/2 times the size of a single nanomesh unit. Finally, $\Delta E_{nm}^{kink-pair}$ is the (free) energy barrier associated with the accumulation of the 211 B atoms and 211 N atoms in this initial kink pair structure. On the high-energy edge, the corresponding energy is to $2E_L - E_H + 2E_{-120} + 2E_{120} - 3E_{nm}/2 + \Delta E_{nm}^{kink-pair}$. We see that in this description, the difference in energy barrier can be related directly to the difference in formation energy of high- and low-energy edges: $3(E_H - E_L) = 0.32$ eV. Since we also know the ratio between these energies from the equilibrium shape (see above), we can now calculate the two energies to be $E_H = 1.1$ eV and $E_L = 0.96$ eV. Even though these are crude estimates, in view of the combination of the error margins on the energy difference and on the energy ratio, it is clear that the edge free energies of the *h*-BN overlayer on Rh(111) are rather low, certainly if we realize that these energies are expressed per unit of length of the nanomesh pattern; per unit cell length of the overlayer itself, the edge energies are as small as 82 meV and 74 meV. For 120° corner filling, the activation energy is expected to be $E_{-120} + E_{120} - E_{nm} + \Delta E_{nm}^{120^\circ}$. The fact that the observed rate for the filling of 120° corners is lower than the kink advancement rate, which should have an activation energy of $-E_{nm} + \Delta E_{nm}^{kink-adv}$, where we expect the two activation energies, $\Delta E_{nm}^{120^\circ}$ and $\Delta E_{nm}^{kink-adv}$, to be close to identical, shows that $E_{-120} + E_{120}$ is nonzero and positive. We find $E_{-120} + E_{120} = 76$ meV, which shows that the corner energy is of the same order of magnitude as the edge energy of a single lattice spacing of the *h*-BN overlayer. We estimate that the energy associated with the filling up of a 60° corner is actually negative. This should make the rate of filling up of such corners very high. Indeed, we have not observed such corners in our movies, except in cases, where they were accompanied by a defect, such as the domain boundary, clearly visible at the 60° corner that is partly filled up in Fig. 4.6D.

4.5 Conclusions

In this chapter we have investigated the growth of *h*-BN from borazine deposited on Rh(111) at various temperatures. Deposition at room temperature and at 627 K did not yet lead to the formation of *h*-BN. Instead, higher-temperature deposition, e.g. at 865 K, or higher-temperature annealing after low-temperature deposition was required to form

h-BN. The borazine was concluded to start decomposing at a temperature between 762 and 806 K.

Borazine deposition at high temperatures, close to the reported optimal conditions, e.g. at 978 K, was found to lead to nanomesh patches that were well-aligned with the Rh(111) substrate. To our surprise, we observed a large growth unit of the overlayer of a full period of the nanomesh superstructure, which contains as much as 169 BN units.

After initial nucleation, the growth of the *h*-BN nanomesh structure can be separated into two steps: creation of new kinks and advancement of existing kinks. The kink creation rate is different for B-terminated and N-terminated edges, while the advancement rate is similar for both. This is explained by comparing the local structures of the kinks on these edges. From the observed growth rates and equilibrium shapes we have determined that the edge energies are 82 and 74 meV per BN lattice unit for the high- and low-energy edges, respectively, and that the sum of the energies for a 120° and a -120° corner is 76 meV.

Chapter 5 Adsorption and decomposition of borazine

5.1 The breaking of B-N bonds

The observation of two different types of island edges implies that B-N bonds are broken at the growth temperature. This is illustrated in Fig. 5.1, which shows that even though it is technically possible to construct a layer of *h*-BN without breaking the B-N bonds in the deposited borazine molecules, the edges of the resulting islands would all be equivalent, terminated by both B- and N-atoms (the outer contour of the island in Fig. 5.1. Different edges, e.g. terminated exclusively by either B-atoms or N-atoms, can only be obtained by interrupting the layer along another direction, as indicated by the red line in Fig. 5.1. Such a termination had already been suggested for BN-islands on Ni(111) [24]. This edge direction is further supported by the observed orientation of the nanomesh pattern in the islands. This can be concluded from a comparison with the atomically resolved images of the nanomesh structure and with supporting theory, in refs. [11, 14]. An *h*-BN island, with a straight edge along the direction of the red line in Fig. 5.1, cannot be created by combining the (BN)₃ rings of the borazine molecules, as building blocks. The breaking of the B-N bonds forms a necessary step in the process. The observed, compact island shapes is an indication of the B-N bond decomposition. This step probably requires a high temperature, as is suggested by the aggregates observed in Fig. 4.2A. These only started rearranging into compact shapes, with the preferred edge orientations (Fig. 4.2B), at temperatures between 762 K and 806 K.

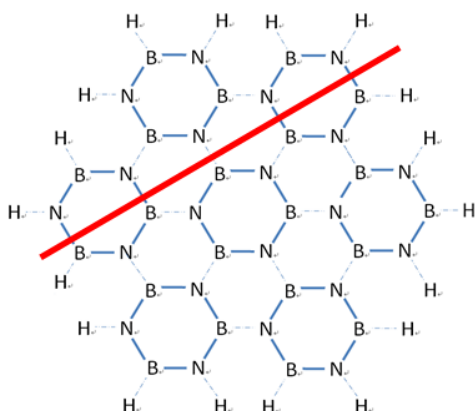


Fig. 5.1 Sketch indicating how an *h*-BN overlayer can be formed without breaking the B-N bonds, by combining the intact (BN)₃ rings originating from the borazine molecules. The solid blue lines denote the bonds in the original molecules; the dashed ones are new, and have formed in combination with the loss of hydrogen. The solid red line shows that only by cutting the B-N bonds the island develop can two different types of edges, as seen in the STM images (e.g. Fig. 4.4) either N- or B-terminated.

5.2 Desorption of borazine molecules and B and N atoms

In section 4.3 it was already mentioned that, after a borazine exposure at a temperature of 672 K a pressure of 3.7×10^{-10} mbar for 10 minutes, no change was detected on the Rh surface. The same exposure at room temperature gave a very noticeable structure. Only when the pressure of the borazine was increased to 1.5×10^{-9} mbar, small islands were formed on the surface. The complete absence of borazine or BN islands on the surface at the lower pressure requires desorption of borazine molecules under those conditions. The density of borazine on the surface must have remained at an equilibrium value that was a function of the borazine pressure. Only when this density exceeded a critical value, as was the case at the higher borazine pressure, nucleation of the *h*-BN islands started, and further deposited borazine could attach onto the newly formed islands. The consumption of borazine by the BN growth must have reduced the density of borazine molecules on the surface.

A similar scenario must apply to B and N adatoms. At a higher temperature of 978 K, a clean Rh surface was first exposed to $\sim 5 \times 10^{-9}$ mbar of borazine for 3 minutes, which did not result in deposition of either borazine or *h*-BN on the surface. An exposure to a higher borazine pressure of 5×10^{-8} mbar for 3 minutes resulted in nucleation at a density of $3/\mu\text{m}^2$. As we had concluded before, borazine had already decomposed at this temperature. This must also have been the case during the lower-pressure exposure. The absence of nucleation at the lower pressure then implies that the fragments of the borazine molecule, i.e. either separate B and N adatoms or BN-units, can also desorb from the Rh(111) surface at 978 K.

5.3 From which borazine is the *h*-BN overlayer formed?

In the previous section we have learned that borazine molecules as well as B and N adatoms can desorb from the metal surface. In this section, we investigate which landing sites of the borazine molecules contribute to the growth of the *h*-BN. The method consists of measuring the rate at which vacancy islands in the *h*-BN overlayer fill up. We can safely assume that the chemical potential, or the density of B and N atoms inside a vacancy island, is uniform, as long as the geometry of the island is not so complex that it would influence the diffusion of the surface species. When we assume that only those borazine molecules that land on the bare metal surface can stick decompose and contribute to the formation of *h*-BN, the time dependence of the total area of the vacancy island can be calculated to satisfy:

$$\frac{dA}{dt} = -\frac{A}{D} I \lambda = \frac{A}{D} \lambda \frac{P}{\sqrt{2\pi m k_b T}} = -\alpha A P \lambda \quad \text{Eq. 5.1}$$

Here, A is the area of the vacancy island; P is the impinging borazine pressure. t is in seconds; λ represents the efficiency effective number of the B and the N atoms from the borazine contributing to the *h*-BN overlayer per impinging borazine molecule. D represents the areal density of B and N atoms in the *h*-BN overlayer and the impingement rate of ethylene I is expressed in terms of the borazine gas pressure P , the (gas) temperature T , and the mass m of a borazine molecule, using standard kinetic gas

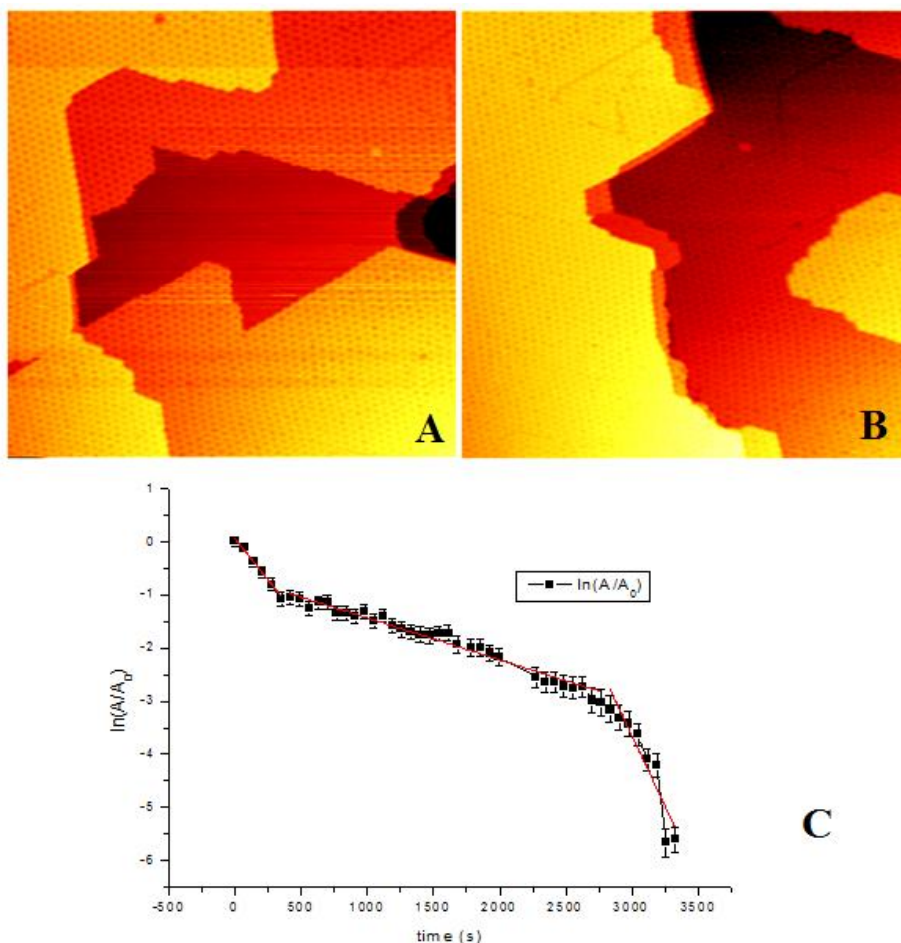


Fig. 5.2 STM images ($170 \times 170 \text{ nm}^2$) at the beginning (A) and end (B) of the filling up of a vacancy island in a *h*-BN overlayer on Rh(111) at a sample temperature of 978 K. The borazine pressure in the vacuum chamber was 3.2×10^{-9} mbar. (C) Time dependence of the area of the vacancy island, relative to the area in image (A). The slopes of the three linear fits to the early, intermediate and late stages of the process are $-3.1 \times 10^{-3} \text{ s}^{-1}$, $-0.79 \times 10^{-3} \text{ s}^{-1}$ and $-5.1 \times 10^{-3} \text{ s}^{-1}$ respectively, corresponding to λ -values of 4.6, 1.2, and 7.6 in Eq. 5.2. As argued in the text, the values that exceed 3 indicate that a significant supply of B and N atoms originates from the lower Rh terrace to which the vacancy island is connected.

theory. The part that has surely remained unchanged during deposition has been combined in the constant α . Based on this differential equation, we expect exponential decay of the uncovered area. Solving this differential equation, we obtain:

$$\ln\left(\frac{A}{A_0}\right) = \alpha P \lambda t \quad \text{Eq. 5.2}$$

Before testing this prediction experimentally, we first calibrated the relation between the measured borazine pressure and the impinging flux of borazine molecules, by exposing a clean Rh surface to a low dose of 2.1×10^{-7} mbar s of borazine at room temperature. We trust that this temperature is low enough to disable decomposition and desorption of the deposited molecules and we assume the resulting coverage to be low enough to avoid reflection of borazine molecules impinging on other borazine molecules. From the coverage of adsorbed borazine molecules visible in the STM image we obtain $\alpha = 2.1 \times 10^5$ an impingement rate on Rh(111) equivalent to 0.65 monolayers of *h*-BN per 10^{-6} mbar s of borazine exposure, where 1 monolayer is defined as a completely filled *h*-BN overlayer. Armed with this calibration, the λ -factor in Eq. 5.2 can be accurately calculated.

We discuss the analysis of the area of the four vacancy islands, shown in Fig. 5.2, Fig. 5.3 and Fig. 5.4. The data in the first two figures were extracted from the experiment at 978 K, discussed above, while the data in Fig. 5.4 had been measured at a somewhat lower temperature of 865 K. Each of the figures shows the first and last images of the episodes that have been analyzed and the graph in each figure is a semilogarithmic plot of the relative area of vacancy islands. The two plots in Fig. 5.4 are for the two vacancy islands in the field of view. The prediction of Eq. 5.2 should result in straight lines in these plots, with a negative slope from which the value of λ can be determined directly. Even though we can fit straight lines to the four semilogarithmic area-versus-time plots, three of the curves deviate noticeably from linear behavior and become steeper towards the end.

5.3 From which borazine is the h-BN overlayer formed?

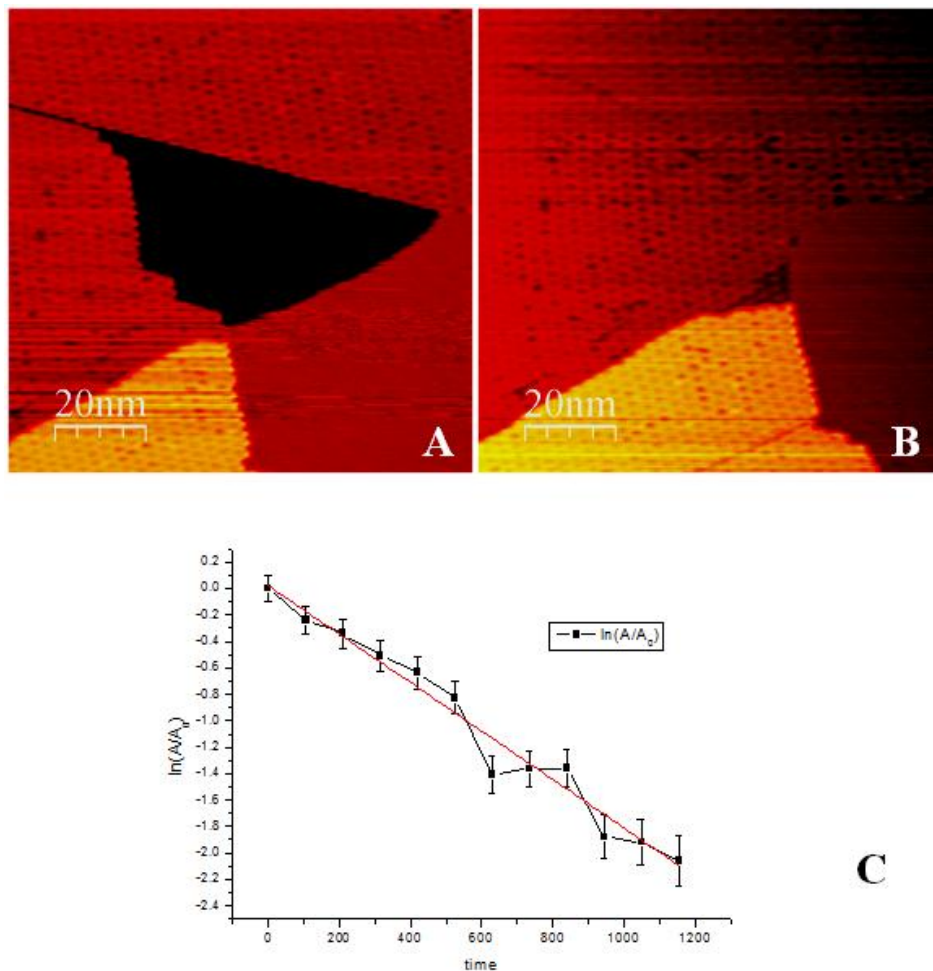


Fig. 5.3 STM images ($100 \times 100 \text{ nm}^2$) at the beginning (A) and end (B) of the filling up of a vacancy island in an h-BN overlayer on Rh(111) at a sample temperature of 978 K. The borazine pressure in the vacuum chamber was 1.5×10^{-9} mbar. (C) Time dependence of the area of the vacancy island, relative to the area in image (A). The slope of the linear fit of $-1.8 \times 10^{-3} \text{ s}^{-1}$ corresponds to a λ -value of 5.7 in Eq. 5.2. As argued in the text, this value, which is higher than 3, indicates that a significant supply of B and N atoms originates from the higher Rh terrace on the right, to which the vacancy island is connected.

The λ -values obtained from the straight-line fits to the data in Fig. 5.2 and Fig. 5.3 are higher than 3, namely 4.6 and 7.6 for the initial and late stages in Fig. 5.2 and 5.7 for the entire fit in Fig. 5.3C. We ascribe these high values to the fact that the two vacancy islands in these figures were both connected to a part of the bare Rh surface that was either one atomic layer higher or lower, of which the area had not been counted as part of the vacancy island. We had initially assumed exchange of B and N between the two Rh levels to be strongly suppressed, but the high λ -values indicate that both vacancy islands had been filling up with a significant supply of B and N from the other Rh level.

The two vacancy islands in Fig. 5.4 were both fully enclosed by the *h*-BN overlayer, so that for these vacancy islands there had been no additional sources of B or N atoms. If we fit straight lines to the area plots for these two islands, we indeed find λ -values below 3, namely 1.2 for the upper island and 1.0 for the lower one. As already mentioned, both plots curve downward. The slopes of the final parts of both curves correspond to λ -values of 3.0, indicating that only in the final stages, when the vacancy islands are close to being filled completely, all B and N atoms from the borazine molecules that impinge on the remaining bare Rh ‘enclaves’ get fully incorporated into the *h*-BN overlayer. The fact that the two curves start out with much more modest slopes shows that in larger vacancy islands, a significant fraction of the supplied borazine molecules (or B and N atoms) is desorbed rather than incorporated. The corresponding finite residence time of the diffusing surface species – adsorbed borazine or B and N adatoms – implies that it can only reach the edge of the vacancy island over a finite distance. In other words, there is a finite, effective capture zone inside the contour of each vacancy island. Borazine impinging within this zone is fully incorporated at the edge and contributes to the filling up of the vacancy island, whereas borazine that impinges on the Rh but closer to the center, i.e. outside the capture zone, is destined to desorb. This scenario naturally explains the curvature of the measured area plots and suggests that we should modify the expected growth law according to:

$$\frac{dA}{dt} = -3\alpha wLP \quad \text{Eq. 5.3}$$

Here, L is the length of the inner contour of the vacancy and w is the width of the capture zone, which is determined by the diffusion coefficient and the residence time and should therefore depend on the substrate temperature. From this we obtain:

$$A(t) = A_0 - 3awP \int_{t_0}^t L(t) dt \quad \text{Eq. 5.4}$$

We can check the validity of Eq. 5.4 by integrating it numerically. The only free fitting parameter is then the width w of the capture zone. The result of this procedure for the upper and lower vacancy islands of Fig. 5.4 is shown by the blue dots in panels C and D. The best-fit values of w are 0.8 nm and 1 nm respectively. For both vacancy islands, this simple model provides an excellent description of the way they fill up as a function of time. The fact that the best-fit values of capture zone widths are nearly identical provides extra confidence that the Eq. 5.3 provides a meaningful description of the process. The capture zone width is surprisingly small, which shows that at 865 K, most of the borazine that impinges on the Rh(111) surface desorbs already within a small number of diffusion steps on the surface.

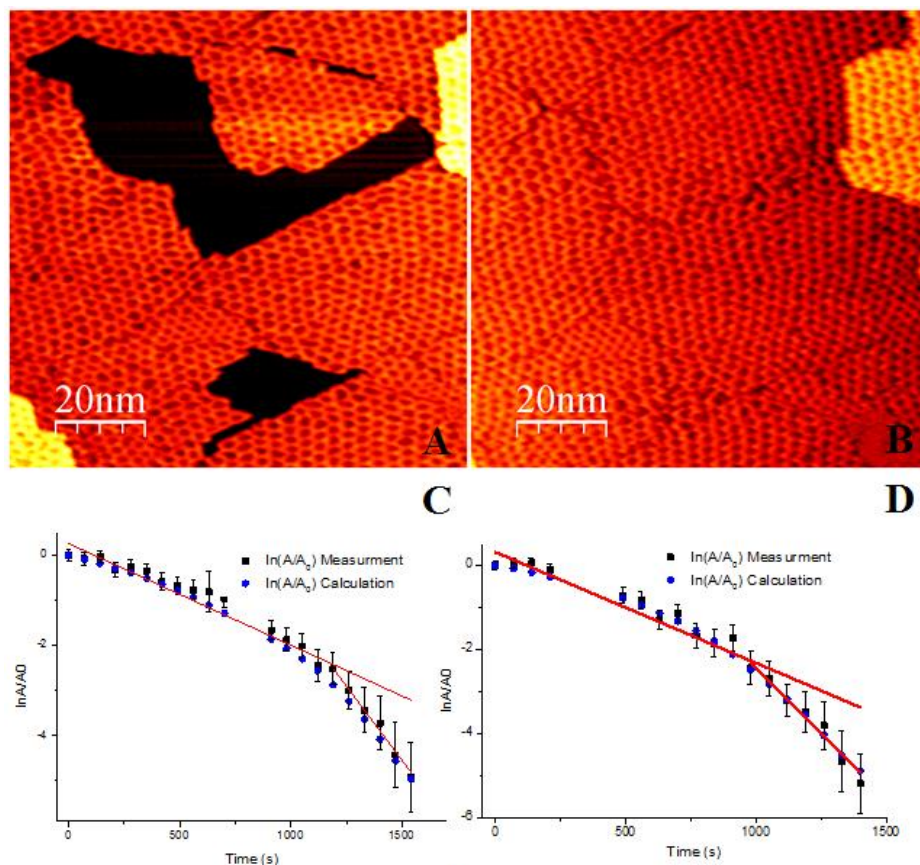


Fig. 5.4 STM images ($100 \times 100 \text{ nm}^2$) at the beginning (A) and end (B) of the filling up of two vacancy islands in an *h*-BN overlayer on Rh(111) at a sample temperature of 865 K. The borazine pressure in the vacuum chamber was 1.0×10^{-8} mbar. In (C) and (D), the black squares are the time-dependent areas measured directly from the images for the upper and lower vacancy islands, relative to their starting sizes in image (A). The linear fits for the full ranges in C and D have slopes of $-2.25 \times 10^{-3} \text{ s}^{-1}$ and $-2.64 \times 10^{-3} \text{ s}^{-1}$, corresponding to λ -values of 1.0 and 1.2 in Eq. 5.2. The slopes of the final sections of the two curves both correspond to $\lambda=3$, showing that all borazine impinging on the enclosed Rh is consumed in the final stages. The blue circles in (C) and (D) are the areas numerically calculated using Eq. 5.4 with finite capture zone widths of $w = 0.8 \text{ nm}$ and 0.1 nm respectively

5.4 Discussion

The conclusion that the capture zone has a width in the order of 1 nm at 865 K seems to be in conflict with the fit in Fig. 5.3, in which the value of λ corresponds to a large capture zone, larger than that of the enclosed Rh terrace and even including part of the Rh surface on another terrace. A possible explanation would be that the higher sample temperature at which the experiment shown in Fig. 5.3. was performed makes the decomposition of borazine possible at the bare Rh, while at 865 K an edge of *h*-BN of a step of Rh may be needed for the decomposition of borazine. So the B and N supply would be much higher at 978 K.

5.5 Conclusion

In this chapter, the desorption and decomposition of borazine during growth conditions were investigated. From the formation of compact islands, we determined the decomposition temperature of borazine on Rh(111) to be between 762 K and 806 K. Borazine only decomposes on Rh surface, while molecules landing on *h*-BN do not contribute to the growth. From *h*-BN formation at 865 K, we learned that the effective capture zone for borazine molecules is 1 nm or less around the *h*-BN edge. At 978 K, the capture zone is much wider and the B and the N atoms can diffuse to higher or lower Rh terraces. This implies that at 865 K an edge of *h*-BN or a step of Rh may be needed for the decomposition of borazine, while at 978 K borazine can decompose on a Rh terrace.

Chapter 6 Defects in the nanomesh lattice

6.1 Structure and formation of domain boundaries

All defect lines that we have encountered in the previous chapters on *h*-BN formation can be viewed as domain boundaries in the overlayer that derive from the problem to match the lattices of neighboring *h*-BN domains. These domains have nucleated independently in the early stages of the growth. The pre-seeding technique, where the initial nucleation had taken place during the warming up of the Rh surface after borazine exposure at room temperature, led to a wide distribution of domain orientations (see e.g. section 4.2). At a modest growth temperature of 865 K on such a pre-seeded surface, the *h*-BN domains could not reorient and the domain boundaries were mainly orientational misfit boundaries. On the atomic scale, the lattice cannot be continuous at such boundaries and unsaturated or hydrogen-terminated B- and N-atoms must be the consequence.

When the nanomesh structure was grown at 978 K, all domains were found to have the same orientation (within one degree). Even though orientational misfit boundaries cannot occur under these conditions, the nanomesh structure still exhibited defects lines at nearly all locations where growing *h*-BN patches encountered and merged. This is illustrated in Movie 3 [79] and in Fig. 6.1A-C. The reason for this is simply that the probability for any two islands to match, even when they have precisely the same orientation, is as low as 1/144. This is because each nanomesh unit cell covers 12×12 unit cells of the underlying Rh(111) surface, leading to 144 translational domains. A more detailed inspection showed that most defect lines appeared as a row of elongated,

compressed, and/or skewed nanomesh rings (Fig. 6.1D). This probably means that, in most cases, the islands attach to each other by forming a fully continuous, albeit somewhat distorted, *h*-BN network, without any dangling bonds. Like in any moiré pattern, the precise nanomesh period is very sensitive to small lattice distortions. For example, a local 4% stretching of the *h*-BN film would already be sufficient to double the size of a nanomesh unit. This effect makes the nanomesh pattern a highly efficient magnifying glass for modest variations in the lattice constant as shown in section 2.3.

In addition to the translational phase differences, we sometimes observed 180° misoriented islands, as had also been found for *h*-BN on Ni [24]. When such islands encountered properly oriented islands, strongly visible defect lines were introduced between them, probably involving dangling bonds in the *h*-BN lattice. This was to be expected, since a continuous network without dangling bonds would have required the formation of N-N bonds or B-B bonds.

In summary, the defects in a completely filled *h*-BN layer can be classified into three types: boundaries between two differently oriented domains, boundaries between domains of which one is 180° misoriented, and translational boundaries between domains with the same orientation. The first case only occurs when the *h*-BN domains originate from nuclei that are formed by warming up a Rh surface that is pre-exposed to borazine at a low temperature, such as room temperature. By necessity, orientational domain boundaries have dangling bonds, as is illustrated by the interrupted network in Fig. 6.1D. Also the boundaries between 180° misoriented domains come with a high density of dangling bonds. Translational boundaries between domains with the same orientation seem to avoid dangling bonds altogether and rather introduce elastic distortions in the overlayer lattice to accommodate the mismatch.

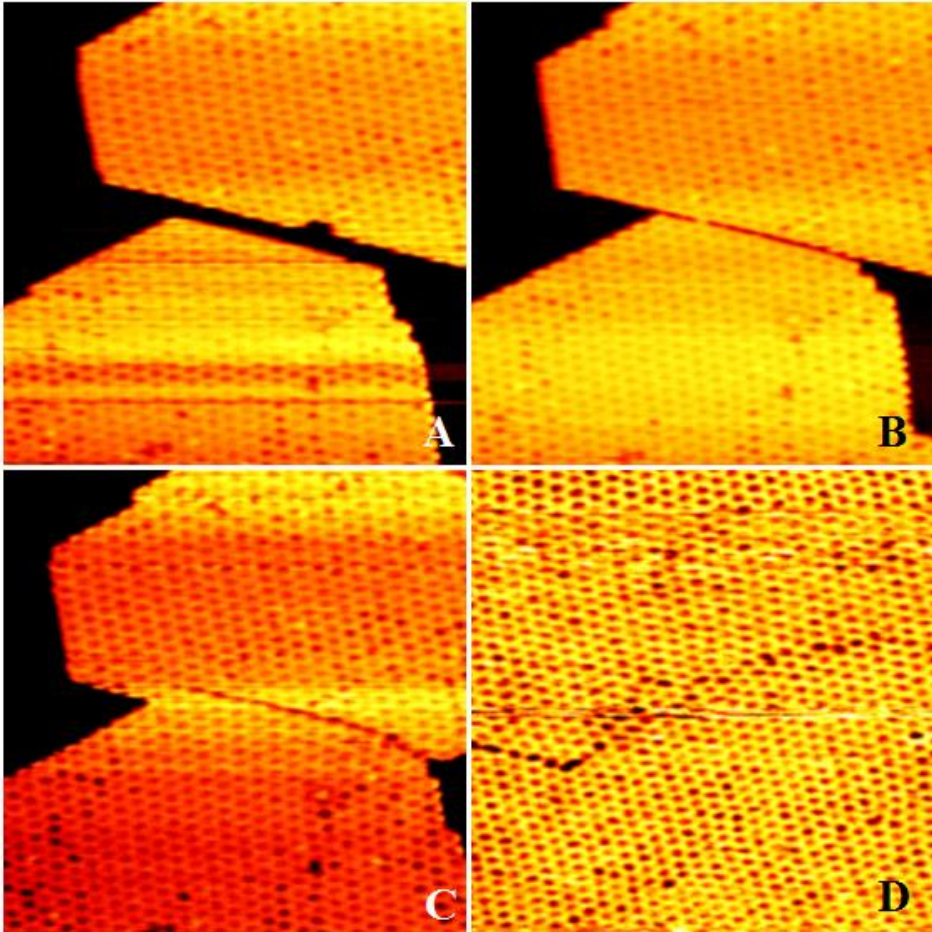


Fig. 6.1 (A-C) Three subsequent STM images from Movie 3 [79], which show the formation of a defect line in the *h*-BN nanomesh overlayer during growth in 1.2×10^{-9} mbar of borazine at 978 K. The two merging islands share the same orientation, but have a translational mismatch, which remains visible, after coalescence, as a row of deformed nanomesh unit cells. These lines were surprisingly immobile, as is illustrated in (D), which shows an STM image taken after the deposition had been completed and the fully *h*-BN covered Rh surface was heated further to 1135 K.

All images are $70 \text{ nm} \times 70 \text{ nm}$, and have been taken at $I_t = 0.05 \text{ nA}$ and $V_b = 1.2 \text{ V}$ (A-C) and 8.4 V (D), and at a rate of 1 image/52.5 s.

6.2 Removal of domain boundaries

Several experiments were performed to investigate whether the domain boundaries can be removed at high temperatures. As discussed in section 4.2 (Fig. 3.1C and D), the *h*-BN overlayer was capable of removing some of the shorter defect lines in the nanomesh structure. However, these domain boundaries were relatively short, typically not longer than one unit of the nanomesh lattice. Whether also longer domain boundaries could be removed was explored, using the network of orientational boundaries, shown in Fig. 4.2D, as a starting situation. In this experiment, the temperature was slowly ramped from 865 K to 1160 K. As shown in Fig. 6.2 and Fig. 6.3A, indeed the density of domain boundaries was reduced when the temperature was raised. In the process, the *h*-BN layer developed vacancy islands (Fig. 6.2B and C), which is the consequence of the area that has become available due to the removal of some of the domain boundaries (Fig. 6.2D), in particular those boundaries that separated *h*-BN domains with a large difference in orientation. The removal of domain boundaries and the clustering into vacancy islands of the area that is freed up in the process both require mobility inside the *h*-BN lattice.

From Fig. 6.3A, we can see that from 865 K where the layer was deposited to ~930 K the reduction of the domain boundary is modest. This is because the mobility of the inside the *h*-BN lattice is still low. From 1060 K to 1160 K the reduction was also low. This is because the low-angle domain boundaries remained immobile at much higher temperatures, even up to 1160 K, at which the *h*-BN layer began to disappear (desorb or dissolve). Similar STM observations were obtained when the sample of Fig. 6.1 was heated up, after the surface had been fully covered by *h*-BN at 978 K: all domain boundaries remained unchanged and static until the *h*-BN layer started to disappear at 1160 K. This absence of defect mobility is illustrated by Fig. 6.1D, which was recorded at 1135 K. Fig. 6.3B and C shows that the angle distribution of the moiré structure is wider at lower temperature. At 865 K the full width at half maximum (FWHM) of the Gauss fit is 23° (Fig. 6.3). A simple calculation of the moiré structure (see Chapter 2) shows that this angular width corresponds to a variation in orientation angle of the *h*-BN of no more than $\pm 1^\circ$ with respect to the Rh(111) substrate. With only one exception on a total of 70, all

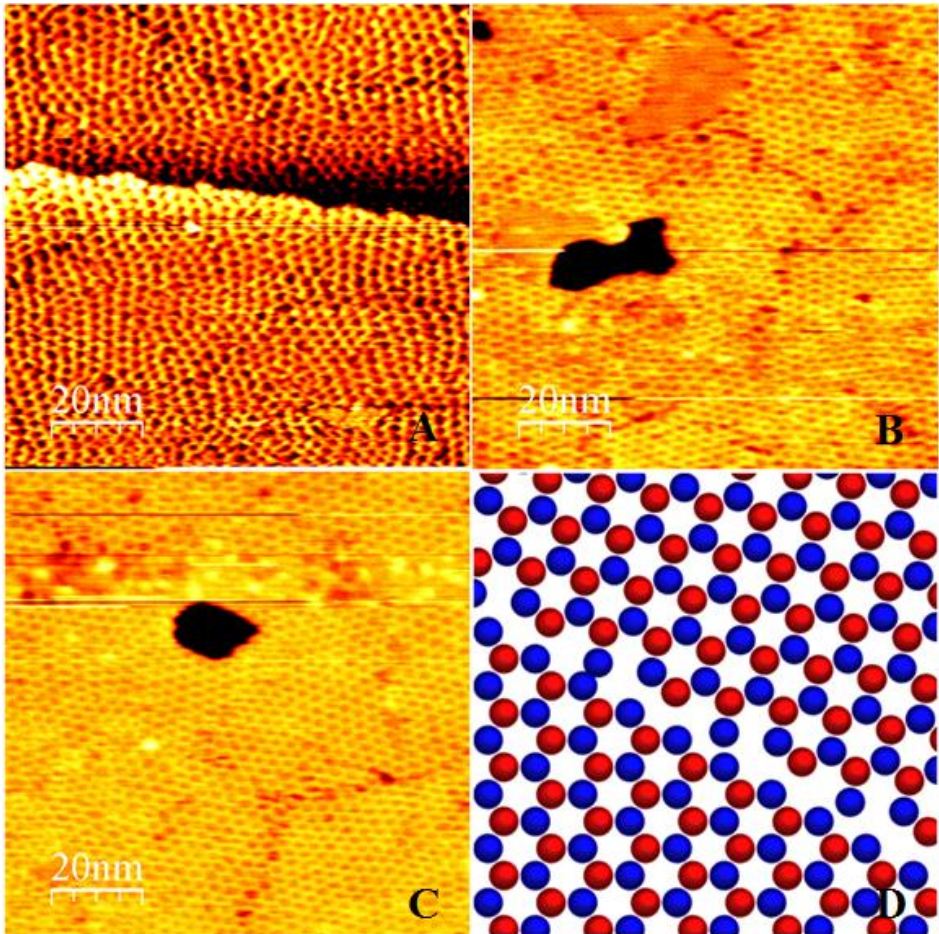


Fig. 6.2 (A - C) Three STM images taken while the sample shown in Fig. 4.2D was heated up. (A) Initial situation at the growth temperature of 865 K, with the surface fully covered by a heavily defective *h*-BN layer. (B) At 1050 K, the domains had become larger, and their orientations differed less from each other than at the lower temperature. The *h*-BN layer exhibited a certain density of vacancy islands. (C) At 1118 K, the domains had become even larger and the orientations had become more similar. Nevertheless, small-angle domain boundaries remained and they were stable until the *h*-BN layer disappeared at 1160 K. (D) Ball model of a high-angle (20°) domain boundary between two *h*-BN patches. The blue and the red balls are the boron and the nitrogen atoms. In the boundary region, the local B and N densities are somewhat lower than in perfect *h*-BN. The vacancy islands in the *h*-BN layers in (C) and (D) are the material deficit that results from the removal of the high-angle boundaries. All images are $100 \text{ nm} \times 100 \text{ nm}$ and have been taken at $I_t = 0.05 \text{ nA}$ and $V_b = -0.2 \text{ V}$, 6.7 V, 8.2 V for A – C, respectively.

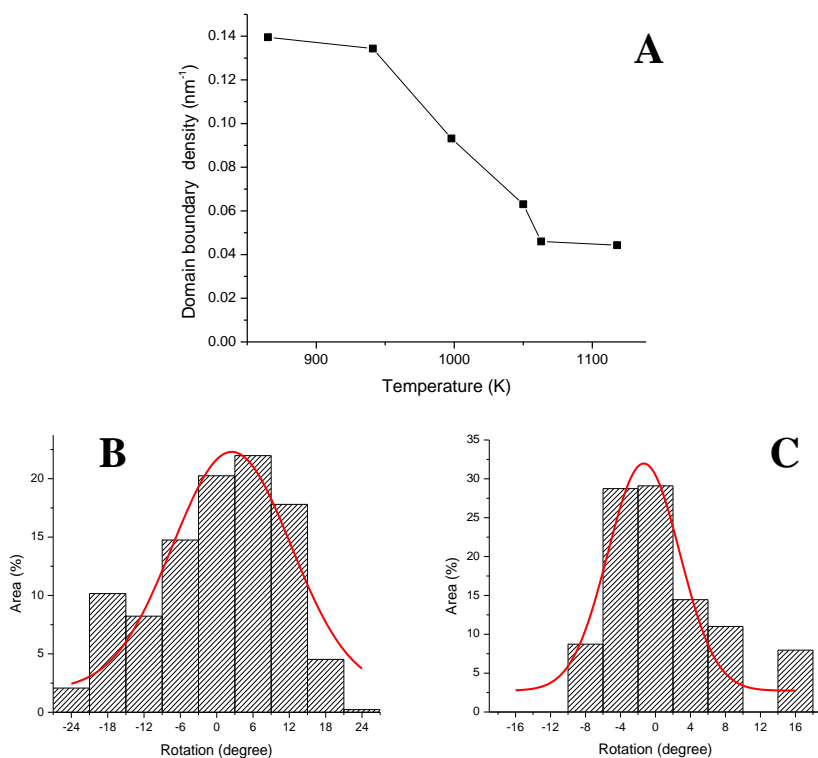


Fig. 6.3 (A) Temperature dependence of the domain boundary density, obtained from the experiment shown in Fig. 6.2. (B and C) Distributions of the rotation angle of the moiré structures observed at 864 K and 1118 K, respectively. Characteristic STM images at these two temperature are shown in Fig. 6.2. The full width at half maximum of the two Gauss fits are 23° and 9.7° for panel B and C, respectively. The asymmetry and offset with respect to 0° were caused by a modest thermal drifting during the STM measurement.

domains were misoriented by less than 2° . At 1118 K, the FWHM of the moiré structure was 9.7° which corresponds a range of rotation angles of $\pm 0.37^\circ$ between *h*-BN and Rh(111). All domains in our STM images at this temperature were misoriented by less than 1.2° . These observations indicate that the mobility of the higher-angle domain boundaries is much higher than that of lower-angle grain boundaries. The large difference in mobility of high- and low-angle domain boundaries is very similar to that

observed for high- and low-angle grain boundaries in three-dimensional crystalline solids. Motion of a low-angle boundary is dictated by the discrete-dislocation character of the boundary structure and transport that therefore necessarily takes place in part along the boundary, whereas high-angle boundaries can move by transfer of atoms directly over the boundary [82, 83].

6.3 Conclusion

Our observations demonstrate that the structural quality of an *h*-BN nanomesh film cannot be improved by post-deposition treatments. At best the high-angle domain boundaries can be removed, but they are only formed when the *h*-BN is nucleated at low temperatures. As shown in Fig. 6.3, the post-deposition annealing temperature should be higher than 950 K to suppress the fraction of wrongly oriented domains. But even at temperatures higher than 1050 K the low-angle and translational boundaries cannot be removed, once formed. Thus, the defect lines remaining after deposition at temperatures above 950 K should be viewed as a fossil of the initial configuration of *h*-BN nuclei and their density directly reflects the nucleation density. To improve the quality of the film further, the only way is, therefore, to lower the density of such nuclei as much as possible. Nucleation-and-growth theory predicts that the nucleation density should be a function of the ratio F/D , where F is the flux of impinging borazine molecules, and D is the two-dimensional diffusion coefficient for these molecules (or their fragments) on the surface [84]. Therefore the best recipe is to combine a low flux and a high diffusion coefficient. It is for the latter reason (high D) that a high temperature is a prerequisite. When the diffusion length has become so high that the nucleation is dominated by defects in the Rh substrate, the F/D argument no longer applies and a further increase in temperature will not significantly improve the film quality. Possibly, this limiting situation has been reached at the typical growth temperature of 1050 K for *h*-BN nanomesh films on Rh(111).

PART II

Graphene formation on Rh(111)

Chapter 7 Introduction to Part II

7.1 General background

Graphene, single-layer graphite, has drawn great attention recently, both because of its special properties, and because of its potential applications, for example, in future-generation electronics [35, 36]. However, reproducibly manufacturing high-quality graphene has remained a challenge. To date, most high-quality graphene, for example for use in experiments requiring high carrier mobilities, is still obtained from graphite, for example, by the ‘scotch-tape’ method [43]. Most methods to assemble graphene directly result in material with a high defect density, caused by multilayer growth [56, 66], chemical contamination [85]. These imperfections seriously influence the properties and the stability of graphene.

Chemical vapor deposition (CVD) of hydrocarbon molecules on transition metals (TMs) provides a practical method for graphene production [25, 51-58]. Since newly arriving hydrocarbon molecules do not stick to or decompose on graphene, CVD may lead to the formation of precisely a single graphene layer, when dissolution and segregation of carbon can be ignored. However, one can also exploit the temperature dependent solubility of carbon in TMs to produce graphene from segregated carbon [51, 53, 57, 59, 60]. The graphene formation process typically takes place at high temperatures, at which the interaction between carbon and TMs is very complex. An essential part of the process, such as the carbon segregation, may be taking place while the metal substrate is cooled down. Often the properties of graphene are measured only at room temperature or below. From such “after-growth” observations it is very difficult to distinguish which source of carbon, segregated or directly deposited, has been responsible for the formation of the graphene layer, and what the precise nucleation and growth mechanisms have been. This is why only a limited number of experiments have been devoted to the kinetic processes of this system [51, 53]. In addition, most of the

experimental methods that can be used *in-situ*, i.e. under growth conditions at high temperature, do not have atomic resolution. Obviously, atomic-scale measurements during graphene growth are really necessary, as they are essential for understanding the nucleation and growth mechanisms, which in turn form the basis for strategies for improving the quality of grown graphene.

7.2 Experimental method

In this part, the formation of graphene on Rh (111), deposited by CVD, was investigated. The main goal was to understand the mechanisms behind graphene formation on transition metals (TMs). This allows us to construct the optimal recipes for producing high-quality graphene, or graphene that satisfies other, special requirements (e.g. multilayer, islanded, etcetera). The main experimental method is a special Scanning Tunneling Microscope (STM), which is applied under actual process conditions, i.e. at elevated temperatures and during substantial variations in temperature. This STM, which has been optimized for (fast) scanning and variable-temperature operation [33, 34], has enabled us to follow the reaction and growth of graphene *in-situ*. Due to its lattice mismatch with Rh(111), graphene forms moiré patterns on this substrate, which work as a 'magnifying glass' for atomic defects in the graphene. In this way, atomic-scale information about the graphene overlayer has been acquired, even from STM images without direct atomic resolution. The system chosen as an example of CVD on TMs is ethylene deposition on Rh (111). The interaction between carbon and Rh can lead to carbide formation [72], carbon dissolution [73] and graphene formation [61], as is also typical for the behavior of carbon on other TMs. Actually, carbon is the main contaminant in purified Rh crystals. Possibly, because this system is so complex, there are relatively few reports about graphite formation on Rh [58, 61]. This complexity makes Rh a good example for demonstrating, in general, the interaction between carbon and TMs. The 3-fold symmetry of the (111) surface was chosen to make it work as a template for graphene crystallization.

7.3 This part of the thesis

This part is organized as follows. The parameters that can influence graphene and carbide formation will be discussed in Chapter 8. We address not only the conventional growth parameters, in this case the temperature and the ethylene pressure, but also the influence of the starting situation. Armed with this information, we propose a first recipe for growing high-quality graphene. In Chapter 9, we further optimize this recipe by controlling the dissolved carbon in the bulk. We conclude that the final quality of the graphene overlayer is limited by the formation of special double layer Rh island structures. Based on the appearance of these structures, we conclude in Chapter 10 that Rh atoms saturate the edges of graphene during growth. In Chapter 11, we provide a detailed, quantitative analysis of various aspects of the growth kinetics. Chapter 12 presents experimental evidence to settle the controversy on the structure of graphene on Rh. Chapter 13 combines all the knowledge acquired in this investigation into one overall picture. This picture can be adapted easily to graphene formation on other TMs and is therefore useful in interpreting this class of growth systems in general and in optimizing growth recipes for each of these cases.

Chapter 8 Parameters influencing Graphene and Carbide formation

8.1 Introduction

The traditional parameters which are used to control the quality of graphene, formed by chemical vapor deposition (CVD), are gas pressure, substrate temperature, heating rate and cooling rate. In this chapter, ethylene deposition on Rh (111) is taken as an example. *In-situ* scanning tunneling microscopy (STM) measurements under various growth conditions and at temperatures up to 1100 K were performed, revealing the processes of graphene formation at the atomic level. We will start the discussion with the influence of the temperature on the formation of graphene and carbide. Then we will introduce a new degree of freedom, demonstrating that by separating the stages of nucleation and further growth and by controlling other growth parameters, we obtain graphene of higher quality, while avoiding carbide formation.

8.2 The temperature dependence of graphene and carbide formation

In order to obtain a first impression of the temperature dependence of graphene formation, we exposed the Rh surface to a high dose of ethylene at room temperature and slowly heated up the sample, while the surface was monitored continuously with STM. The initial, saturated layer of ethylene was obtained by exposing the freshly cleaned Rh(111) surface [73] in the UHV chamber to 3×10^5 mbar s of ethylene gas at room temperature. The result of this exposure is a pronounced, atomic-scale roughness,

decorating the entire surface (Fig. 8.1A), that we associate with the disordered overlayer of ethylene molecules. During the initial stages of the temperature ramp, clusters formed without any preference for specific edge orientations (Fig. 8.1B). These clusters grew in size when the temperature was increased. Even though we have directly observed the motion and coalescence of the clusters, the drifting during temperature changes makes it difficult to conclude that this was the sole ripening mechanism. Previous research showed ethylene decomposition on Rh to proceed in various stages at different temperatures up to ~800 K [61, 86]. Based on this, we interpret the irregular structures in Fig. 8.1B to be clusters of carbon or CH_x . At around 870 K, some islands were observed with a hexagonal shape, and the characteristic moiré pattern inside, indicating that, at this temperature, graphene had already been formed, and that the domains were large enough to appear as moiré patterns. The restructuring of the overlayer into graphene necessarily should start with small domains, smaller than one unit of the moiré pattern ($2 \times 12 \times 12$ carbon atoms). Ripening processes make some domains grow at the expense of others, to become larger than this size. Because any ripening process requires the relocation of many C atoms, this ripening should be relatively slow [87]. The combination of this slow ripening with the fast temperature ramp up to 870 K of 0.2 K/s, implies that the moiré pattern observed at 870 K is a sign that graphene formation had started already at a temperature below 870 K. Indeed, Fig. 8.1C shows our lowest-temperature observation of a moiré pattern, at 808 K, (temperature ramp rate was 0.05 K/s) close to the temperature range of 700-800 K, necessary for complete decomposition of ethylene [61, 86]. Up to 969 K, the ripening of the graphene islands continued, making the islands larger, more compact and more hexagonal (Fig. 8.1D). Also, the orientations of different domains became similar. Nevertheless, we still observed more than a single moiré pattern at this high temperature, which indicates that several overlayer orientations may have similarly low energies.

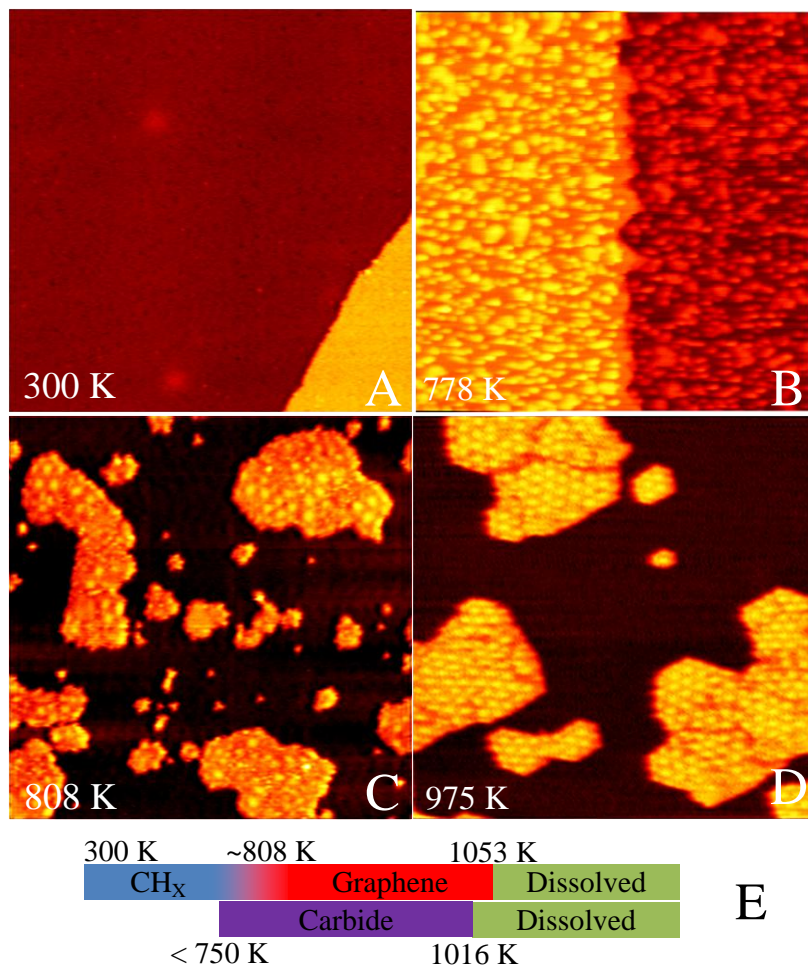


Fig. 8.1 STM images measured during continuous heating from 300 K to ~1000 K, after room temperature ethylene deposition. Panels A, B and D are from one series of experiments. (A) The Rh(111) surface directly after exposure to 3×10^{-5} mbar s of ethylene at room temperature. A mono-atomic step on the Rh surface crosses the image. The saturated ethylene adsorbed layer causes the rough appearance of the upper and lower terraces. (B) At 778 K, the overlayer organized into irregular clusters, but no moiré pattern was found at this temperature. (C) Starting from 4×10^{-7} mbar s ethylene exposure at room temperature, this image shows the lowest temperature where the moiré pattern of graphene was found. (D) At 975 K, the graphene had ripened into larger islands, with similar orientations. (E) Temperature ranges for the observed stability of graphene and carbide on Rh(111).

The STM images all have a size of $85 \text{ nm} \times 85 \text{ nm}$. They have been taken at sample voltages of $V_b = 0.05 \text{ V}$, 1.16 V , 1.43 V , and -1.84 V for panels A, B, C and D, respectively, and at a tunnel current of $I_t = 0.05 \text{ nA}$.

In a separate experiment we found that the graphene overlayer dissolved into the Rh substrate, starting at a temperature of ~ 1050 K. The information obtained from these heating experiments can be cast in the form of the upper temperature bar in Fig. 8.1E, displaying that, from 808 K to 1053 K, graphene can be formed on a Rh surface. This 250 K temperature range for stable graphene on Rh is much wider than the 50 K window that has been reported previously [88]. This process, combining adsorption of ethylene at room temperature with a subsequent temperature ramp, also yields a lower graphene formation temperature than the temperature of ~ 1100 K, reported in case ethylene was dosed directly at high temperature [89].

Similar to the case of *h*-BN nanomesh formation on Rh(111) [20], the quality of the graphene overlayer is limited by defects in the form of two different classes of domain boundaries. One class results from the merger of neighboring graphene islands with different orientations. On the atomic scale, this type of domain boundary must involve defects with respect to the hexagonal structure of perfect graphene, for example arrays of pentagons and/or heptagons [54] instead of the normal hexagons. The other class of domain boundaries originates from the merger of islands with precisely the same orientation. Due to the mismatch in lattice spacing between the overlayer and the substrate, there are still 288 translationally inequivalent possibilities to position the graphene on the Rh(111). This makes the probability for a perfect fit lower than 0.4%, so that most of these mergers will be accompanied by a phase defect line in the moiré pattern. Although such lines may look 'dramatic', we speculate that this phase defect is not leading to dangling bonds, i.e., the defect is present only in the period and the superstructure but not in the topology of the graphene network [54]. Since both classes of defects derive from the boundaries between individual graphene islands, the defect density is completely determined by the initial nucleation density of the growing overlayer.

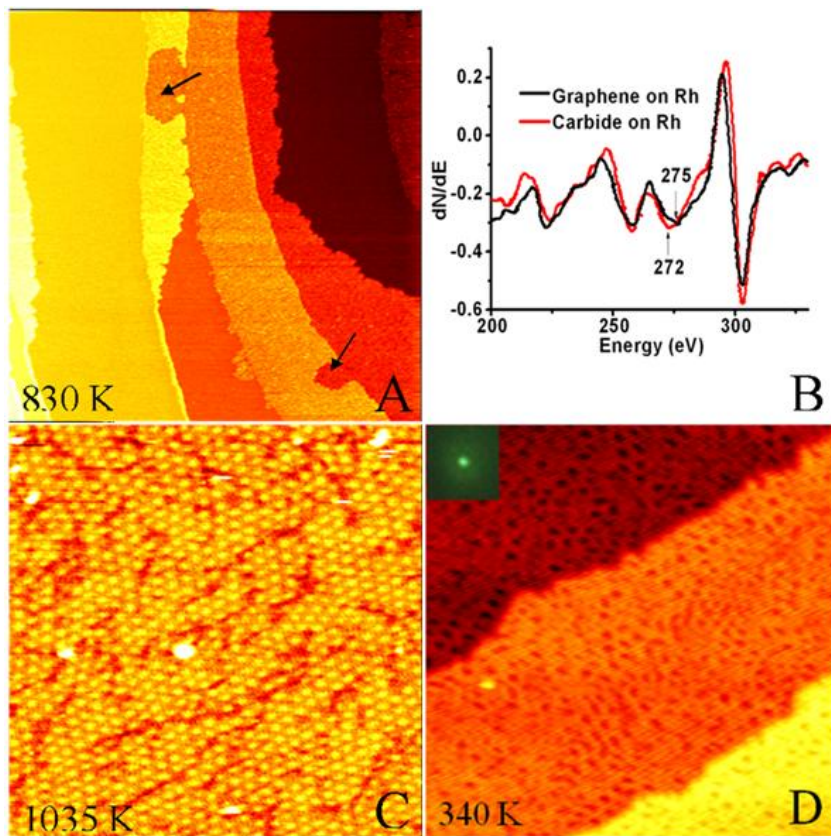


Fig. 8.2 Direct ethylene deposition at different temperatures. (A) An STM image measured at 830K, during deposition of ethylene. We interpret the rough layer that started to grow from the Rh steps as a carbide film (see text). Before nucleation of the film, the Rh steps were modified, as is indicated by the arrows. Nucleation started when the ethylene pressure reached 4.4×10^{-8} mbar. (B) Comparison between two Auger electron spectra of Rh(111); red: with a single-monolayer carbide covered Rh, formed by ethylene deposition at 750K, and black: with single-layer graphene. (C) A STM image of graphene-covered Rh, which was achieved by direct ethylene deposition at a pressure of 3.5×10^{-7} mbar and a temperature of 1035K. The image was taken at the growth temperature. The ‘defect’ lines in the image were formed already before the graphene overlayer nucleated. We associate these lines with dissolved carbon atoms. (D) STM image of the sample of (C), after it was cooled to 340 K. The moiré pattern of the graphene was deformed. The inset in (D) shows one integer-order Rh LEED spot (same view as in inset of fig. 1C) and the near absence of superstructure spots around it, recorded at room temperature.

The STM images all have a size of $85 \text{ nm} \times 85 \text{ nm}$. They have been taken at sample voltages of $V_b = 2.79 \text{ V}$, 2.52 V , and 3.74 V for panels A, C, and D, respectively, and at a tunnel current of $I_t = 0.05 \text{ nA}$.

In a first attempt to reduce the nucleation density, we increased the diffusion coefficient of adsorbed carbon atoms by exposing a clean Rh sample directly to ethylene at elevated temperatures, e.g. 750 K and 830 K. As predicted by nucleation theory [84], the high diffusion coefficient together with the low deposition rate should result in a lower nucleation density. With STM it was seen that an overlayer formed, starting from the steps on the Rh surface, and proceeding until it covered the entire surface. As can be seen in Fig. 8.2A, this overlayer had a structure that was different from that of graphene. After the entire surface had been covered by this layer, we heated the sample to higher temperatures, while monitoring the structure with the STM. It was found that the overlayer did not transform into the graphene structure even up to the temperature of 1016 K, at which it disappeared. The stability of the structure indicates that it did not consist of CH_x clusters, which would otherwise have transformed into graphene at and above 808 K. We interpret the disappearance again as the dissolution of the deposited material into the Rh substrate. The fact that the dissolution temperature differs significantly from the value of 1050 K, mentioned above for graphene, indicates that in this case the overlayer was not graphene. Auger electron spectroscopy (AES) (Fig. 8.2 B) on this layer shows that the KLL of C peak had shifted from 272 eV to 275 eV and the MNN peak of Rh had also undergone a change in shape and position. Both shifts indicate the formation of a new compound [90]. We suggest that this is a rhodium carbide overlayer. Comparing this AES spectrum with a reference spectrum taken on a one-monolayer graphene-covered Rh surface (Fig. 8.2B), we see that the C-to-Rh peak ratios for these two cases were similar. Assuming that the Rh peak in the AES spectrum of graphene-covered Rh corresponds to effectively one atomic layer of Rh, we find that the C-to-Rh ratio in the carbide must have been in the order of 2:1. In analogy to the temperature bar for a graphene overlayer, the lower bar in Fig. 8.1E shows the growth and stability regime of a carbide layer on Rh(111).

Attempts were also made to deposit ethylene directly onto Rh, at an even higher temperature, still within the range where both graphene and carbide layers are stable (see the two bars in Fig. 8.1E), e.g. at 982 K. Here we observed regions similar to Fig. 8.2C and other regions similar to Fig. 8.2A, i.e. both graphene and carbide were present on the surface. Interestingly, there is a narrow temperature window, between 1016 K and 1053 K, in which a carbide layer is no longer stable, but a graphene monolayer is. In order to explore this window, we held the Rh at 1028 K, while dosing again with ethylene. Indeed, a graphene layer was observed to form at this temperature. It covered the entire

surface without a trace of carbide (Fig. 8.2C). However, the moiré pattern of the graphene overlayer became distorted during the slow cooling down, after the deposition, as shown in Fig. 8.2D. The low-energy electron diffraction (LEED) pattern that was taken afterwards at room temperature showed a weak Rh(111) pattern on a strong, diffuse background (inset Fig. 8.2D). We attribute the deterioration of the overlayer during the cooling down to segregation. It is known that carbon, which dissolves into the near-surface region of the Rh at the growth temperature, can segregate back to the surface when the temperature is decreased [73]. This segregation could lead to the nucleation of islands of a second graphene or carbide layer, between the original one and the Rh substrate, which will locally push up the graphene overlayer and distort it. We can exclude the alternative explanation that the deterioration of the graphene during cooling was caused by the differential expansion coefficient between graphene and the Rh substrate (in this temperature regime graphene has a negative expansion coefficient) [refs], since other experiments, in which the role of segregated carbon could be minimized (see below), showed that the quality of the graphene was not affected solely by large changes in temperature.

8.3 The crucial role of the history of the sample

The above experiments demonstrated that the temperature window for producing graphene by direct deposition is quite limited, and graphene formed in this temperature window distorts when the substrate is subsequently cooled to room temperature. On the other hand, the first experiment, which started with deposition at room temperature, showed a wider temperature window for graphene formation (upper bar in Fig. 8.1E), starting below and ending above the carbide window (lower bar in Fig. 8.1E). The lower onset temperature may be beneficial since it will eventually lead to a lower strain level in the graphene, once it is cooled down to room temperature, since there is a significant difference in thermal expansion between the graphene overlayer and the Rh substrate [91, 92]. The lower temperature is also helpful in reducing the level of carbon dissolution into the Rh substrate. The differences between the two experiments in Fig. 8.1 and Fig. 8.2A further suggest that the choice made by the growing overlayer between carbide and

graphene, in the temperature interval from 800 K to 1016 K, is fully determined by the structure of the early overlayer nuclei; in other words, graphene patches will continue to grow as graphene, whereas carbide patches will continue to grow as carbide. In turn, this suggests a refinement of our approach, namely to separate the stage of nucleation from that of further growth. For example, one could start with the graphene-seeded Rh surface from the first experiment, and expose that to further ethylene deposition under different conditions, in order to obtain full coverage by graphene. One may expect nucleation and growth of the graphene overlayer to follow well-known rules, in which the nucleation density is determined by F/D , where F is the flux of arriving atoms and D is their surface diffusion coefficient [84]. If the deposition is carried out very slowly, so that the number determined by F/D is smaller than the existing seed density on the surface, the newly arriving carbon atoms will all be incorporated onto the edges of growing graphene islands, thus preventing them from forming new nuclei [93]. The presence of the graphene seeds on the surface should have the additional effect that newly arriving carbon atoms have a strongly reduced probability to dissolve into the Rh, again because they will be incorporated in the graphene overlayer on a much shorter timescale, due to the difference in the rates of diffusion of the carbon atoms into the bulk and over the surface, which should be expected to be significant. On a non-seeded surface, dissolution has to compete only with the rather rare processes of nucleation of either graphene or of carbide. How 'difficult' graphene nucleation is on a hot Rh surface is evidenced by our findings in a separate experiment, on a clean Rh surface: at 1028 K, an ethylene pressure of to 3.5×10^{-7} mbar was required to observe the first graphene nuclei in our STM images.

The suggested approach, of ethylene deposition at high temperatures onto a Rh surface that has been pre-seeded with graphene by low-temperature deposition, was successful. Fig. 8.3 shows the result obtained at a growth temperature of 975 K; even more informative is the corresponding STM movie, which can be found online. Starting with the end situation of the first experiment (Fig. 8.1D), ethylene was deposited, at a pressure of 3×10^{-9} mbar, which was increased at the end of the procedure to 1×10^{-8} mbar, simply to accelerate the process. The newly arrived carbon atoms continued with the structure and orientation of the graphene that was already present, until the entire surface was covered by graphene. When a new kink formed at a concave corner between two differently oriented domains, it showed a preference for following the graphene domain which had the same, or a similar orientation, as the Rh crystal. In this way, the metal

substrate guided the orientation of the graphene layer, and the density of domain boundaries became lower than that expected from the initial configuration of the graphene seeds. After this sample had been cooled down to room temperature, neither STM nor LEED (insert of Fig. 8.3B) showed a deformation of the moiré pattern. The LEED pattern showed that the graphene layer had a preferred orientation; otherwise, a ring of intensity should have been observed around the integer-order maxima from the Rh, rather than the six superstructure spots that are clearly present in the LEED pattern. Although the superstructure spots are not very sharp, the orientation difference between graphene domains is seen to be minor, because the moiré pattern is an amplifier of all variations in position and orientation. The bright regions, indicated by black arrows in Fig. 8.3B, were formed in the final stage of the deposition. They will be explained in Chapter 10.

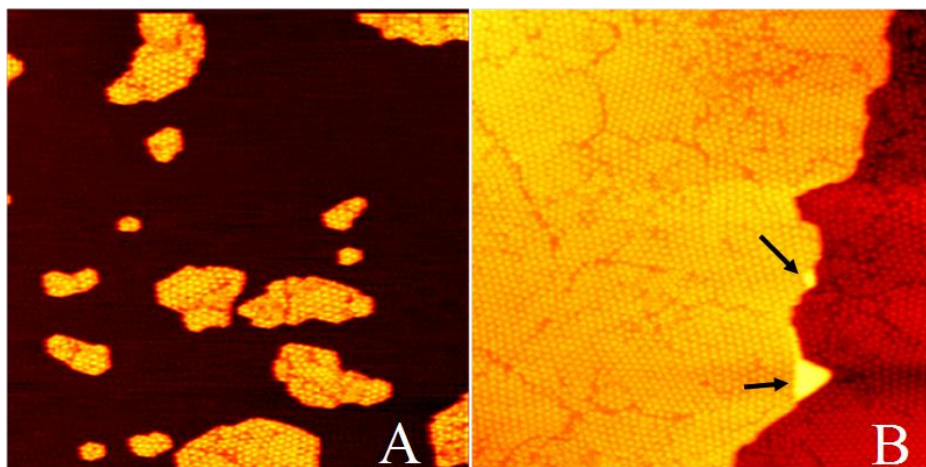


Fig. 8.3 STM images of graphene formation, starting with a seeded surface. (A) The graphene-seeded Rh surface achieved by annealing a pre-deposited sample from room temperature to 975 K. Most of the graphene islands had same orientation. But superstructure domain boundaries can be found within individual islands. (B) Graphene-covered Rh, after ethylene deposition at 975K on the seeded surface, at pressures ranging from 3×10^{-9} to 1×10^{-8} mbar over a period of 76 minutes. During this procedure, The domain boundary density became $\sim 30\%$ lower than that in the starting situation. (A). Two Rh double-layer defects are indicated by the arrows. The inset in (B) shows the superstructure spots around one Rh LEED spot.

All images are $160 \text{ nm} \times 160 \text{ nm}$ and have been taken at a sample voltage of $V_b = -1.84 \text{ V}$ and a tunneling current of $I_t = 0.05 \text{ nA}$.

8.4 Conclusion

In this chapter we have measured the formation and dissolution temperatures for both graphene and carbide. Although graphene can be formed at 800 K by ethylene exposure at room temperature and annealing, direct exposure of ethylene of the Rh surface at 800 K – 1000 K results in carbide formation. Ethylene exposure of Rh at 1035 K provided a graphene layer at high temperature, but the moiré structure was distorted during cooling of the sample. To solve these problems, a new element was introduced, which is the initial nucleation stage. It determines nearly completely the phase in which further C is incorporated, graphene or rhodium carbide, and it determines the variation in orientation of the growing graphene patches. We demonstrate that by separating the stages of nucleation and further growth and by controlling other growth parameters, we obtain graphene of higher quality, while avoiding carbide formation and controlling the dissolving of C.

Chapter 9 Towards the optimal growth recipe

9.1 Introduction

In the previous chapter, it was shown that the deposition of ethylene can be controlled to form exclusively graphene rather than carbide, and to bring the process to a lower temperature. In this chapter we show that as an alternative to direct deposition, also the segregation of dissolved carbon atoms could be used in a controlled way, in order to form graphene. By cooling down the sample very slowly, the effective flux of segregated carbon is kept low. These carbon atoms also tend to follow the structure and orientation of the pre-existing seeds; if these have the graphene structure, this procedure results in the growth of graphene. After the segregation has come to an end, the coverage of the graphene overlayer can be brought to completion by a final ethylene exposure. This lower process temperature will be associated with a lower density of C dissolved in the substrate and, if it is of any importance, also with a lower strain due to the differential thermal expansion between the graphene overlayer and the Rh substrate [91, 92].

9.2 Using segregated carbon to form graphene

This alternative procedure using segregated carbon to form graphene was also successful, as is shown in Fig. 9.1A, where a part of the surface was followed from 862 to 829 K. This is very promising for achieving 2D single crystalline graphene, using

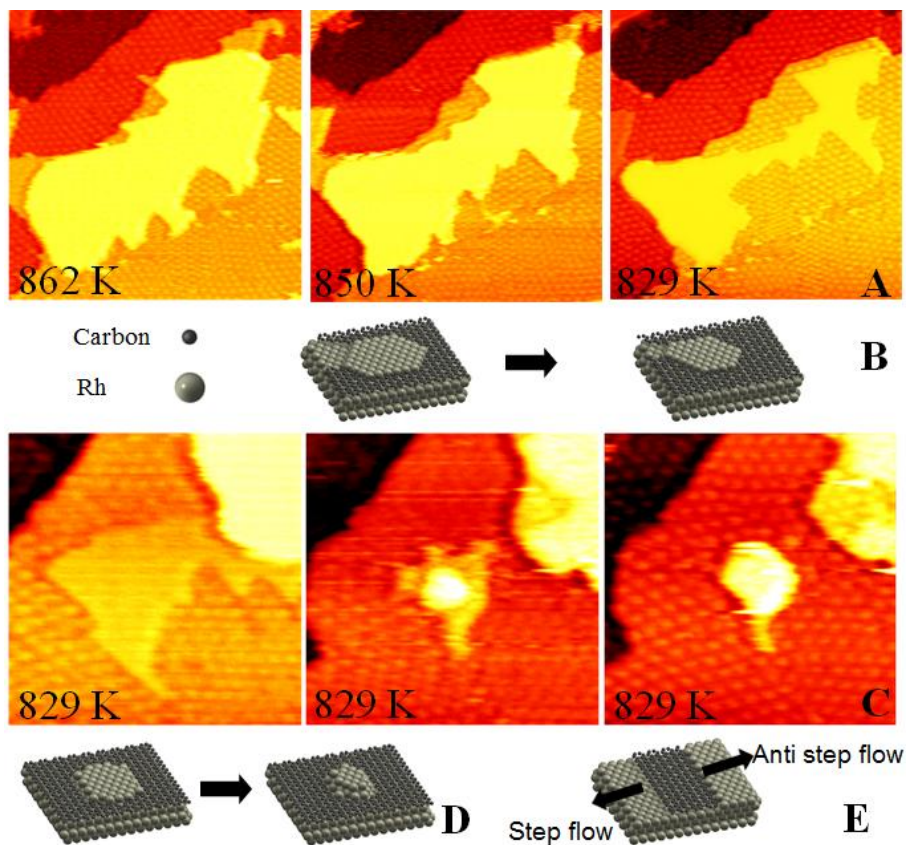


Fig. 9.1 Graphene formation by dissolved carbon and Rh double layer defect formation. (A) STM images of the same area during the cooling down of a Rh sample, partly covered by graphene, after adsorption of ethylene at room temperature and annealing to 977K. The Rh island indicated by the red arrow is in the same atomic level as the graphene indicated by black arrow. They seem to be in different levels because of the sample voltage setting. The segregated carbon followed the orientation of the existing graphene. Image size: $100 \times 100 \text{ nm}^2$. (B) A simple atomic model of the graphene formation by segregated carbon. The Rh island became smaller, because Rh diffused away via the small opening in the graphene layer. (C) Graphene growth, by adding more ethylene while the sample was held at 829K. These images show how a Rh island, enclosed by graphene, was pushed into a double layer island with half of the original area. Growth of the graphene stopped after the whole island had become a double layer. Image size: $50 \times 50 \text{ nm}^2$. (D) A sketch of the formation of the Rh double layer island. (E) The concept of step flow and anti step flow. In the latter case, Rh atoms have to move to the upper atomic level, in order for the surface to accommodate the additional carbon.

dissolved carbon. One difference, relative to deposited carbon, is that the graphene layer also chose the growth direction (Fig. 9.1E) where the Rh step has to retract, to allow further graphene growth. To emphasize that this proceeds against the direction of regular step-flow growth, we refer to this as 'anti-step flow'; in some papers it is called 'growth by etching step edges' [94]. In this temperature regime, Rh atoms should be expected to diffuse much faster over the surface than the carbon atoms can in graphene. When sites become temporarily available, as a result of step fluctuations of the Rh, newly arriving carbon atoms may fill up the vacant sites, the strong cohesion in the graphene preventing the Rh step from fluctuating completely back to its original shape and location. This anti-step-flow mechanism resulted in a large number of Rh islands enclosed by graphene.

9.3 Further ethylene deposition

Fig. 9.1C shows one of Rh islands enclosed by graphene, to which more ethylene had been added. The carbon introduced by the ethylene deposition was found to also be accommodated via the anti-step-flow mechanism, instead of forming graphene on top of the enclosed Rh. In this stage, Rh atoms were pushed up and nucleated a higher atomic layer; the graphene stopped growing when the complete enclosed Rh island had a double-layer height (Fig. 9.1A). The reason that, in Fig. 9.1A, the Rh did not become a double-layer structure, is that, in that case, there was a narrow passage in the graphene layer, through which the Rh could diffuse away. In separate experiments, in which the Rh was exposed to ethylene at a low temperature of 864 K, the growth of graphene, both at the free edges of graphene islands ('step-flow' growth) and growth against the Rh steps ('anti-step-flow') was observed. At this temperature, the growth rates for these two mechanisms were comparable. At the higher temperatures of the experiments discussed before, e.g. at 975 K, the anti-step-flow growth rate was much lower than the step-flow growth rate. That the mechanism was still active is illustrated by the appearance of double-layer defects in the final stages of the graphene growth, as is indicated by the two arrows in Fig. 8.3B. The temperature dependence of the ratio between the two growth rates can be explained as follows. Assume that decomposition of ethylene or the growth of graphene has a lower energy barrier at the step edges of Rh than on the terraces. At 864 K, the resulting higher decomposition or growth rate of ethylene at the Rh step

makes the amount of carbon atoms available for anti-step-flow higher than that for step-flow growth. At 975 K, all ethylene on the Rh terraces rapidly decomposes, which means that the carbon production rate is not limited, at that temperature, by the decomposition, but by the deposition of ethylene. Since the steps represent a much smaller effective area than the terraces, and the anti-step-flow requires an additional process of moving Rh atoms, the ratio between anti-step-flow and step-flow should become low at high temperatures. Nevertheless, anti-step-flow will still occur, and it will lead to Rh double-layer defects. The only way to reduce their density is by further elevating the temperature or by making the average distance between the graphene nuclei larger than the average distance between the steps on the Rh substrate.

9.4 Conclusion

Our attempts to use segregated C plus further ethylene deposition at low temperature to form a complete, undistorted graphene overlayer were successful. The added graphene follows the graphene phase and orientation of the initially present nuclei. This procedure forms a very promising route for achieving 2D single-crystalline graphene. However, the low growth temperature results in a high growth rate of graphene in the anti-step-flow direction. This results in many Rh double-layer defects, which form holes in the final graphene overlayer.

Chapter 10 Rh island formation induced by graphene growth

10.1 Introduction

One of the interesting phenomena already mentioned in the previous chapter was the formation of double-layer Rh island structures by an enclosing graphene monolayer. The origin of these structures will be discussed in more detail in the present chapter.

10.2 Experiment

In Fig. 10.1 and Fig. 10.2, two examples are given of the condensation of Rh adatoms into Rh islands. The sample was prepared by graphene seeding (annealing a pre-deposited sample from room temperature to 975K) and further ethylene deposition, as in previous chapters. The STM images are from the same sequence as the one shown in Fig. 8.3. The images and cross sections in Fig. 10.1 and Fig. 10.2 show that the average height of those Rh areas that were fully enclosed by the growing graphene, increased gradually, as the graphene growth made these areas shrink. This gradual increase in height suggests that the enclosed Rh areas carried a mobile, two-dimensional (lattice) gas of some species other than carbon, of which the density increased as the areas were forced to shrink. Eventually, the density of this mobile overlayer reached a critical value, at which an island was nucleated on each of the enclosed Rh areas. This mobile surface species cannot have originated from the residual gas, because of the low base pressure of the UHV chamber and the high purity of the ethylene gas. The only possibility is that it consisted of Rh adatoms created by the anti-step flow mechanism (Chapter 9), prior to the closure of the perimeter of a hole in the graphene overlayer. The

final height of the islands, at the point where the graphene front came to a standstill, fitted reasonably with the height expected for two layers of Rh (Fig. 10.1(C & D) and Fig. 10.2(C & D)), supporting our conclusion that they consisted completely of Rh and that the mobile overlayer, present before this nucleation, also consisted of Rh adatoms, confined by the surrounding graphene edges. Since graphene prefers Rh steps as nucleation sites, geometries in which Rh adatoms are confined by graphene should occur frequently. The confinement can easily lead to situations in which the local density of Rh adatoms is significantly above the equilibrium Rh adatom density on Rh(111) at the graphene growth temperature.

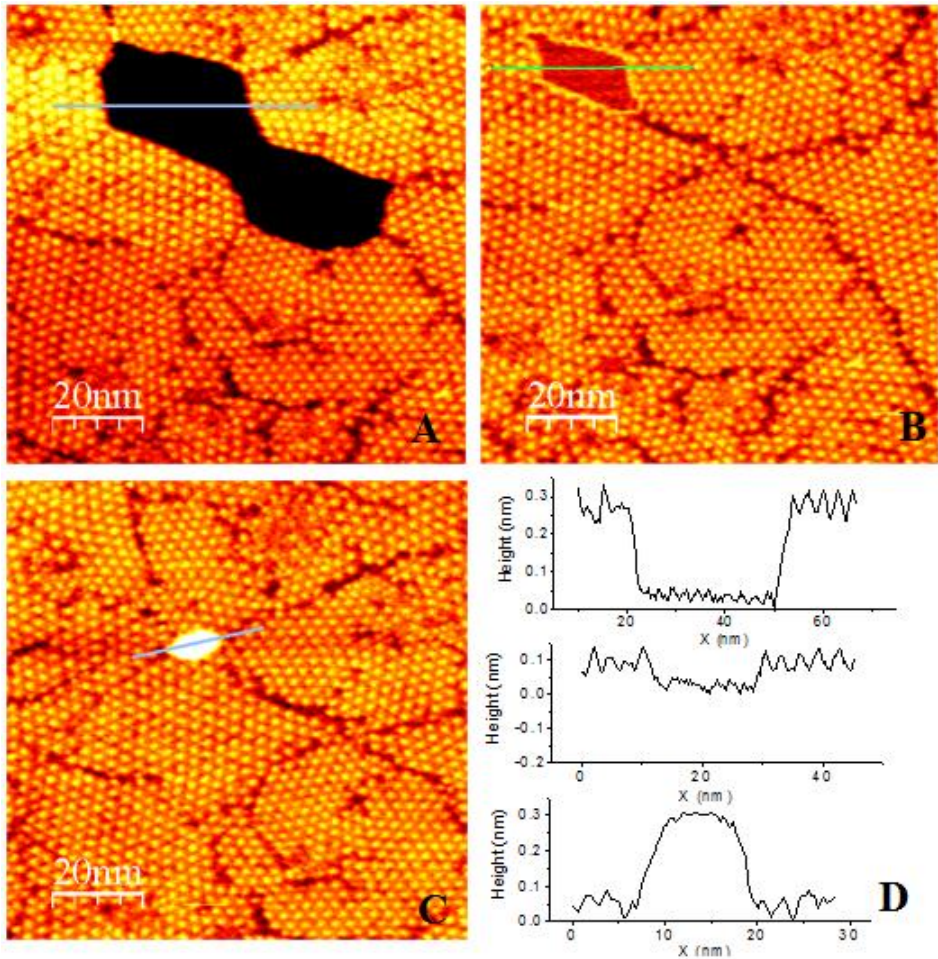


Fig. 10.1 STM images of confinement and nucleation of Rh adatoms due to graphene growth. (A) The starting situation of the graphene overlayer that encloses a bare region of Rh substrate. The concentration of Rh adatoms is still low. (B) The same area after 367 seconds of ethylene deposition at two pressures, of 0.56×10^{-8} and 1.4×10^{-8} . The apparent height of the enclosed Rh area increased, which we attribute to the increase in the concentration of Rh adatoms. (C) The final state of the vacancy island: a two-layer high Rh island has been formed by the adatoms. (D) Height profiles along the lines in images A, B, and C (top to bottom). With respect to the original level of the enclosed Rh area, the heights have increased by almost zero in A, approximately 0.2 nm in B, and 0.5 nm, corresponding to 2 layers of Rh in C. The STM images all had a size of $100 \text{ nm} \times 100 \text{ nm}$, and have been taken at a sample voltage of $V_b = -1.84 \text{ V}$ and a tunneling current of $I_t = 0.05 \text{ nA}$.

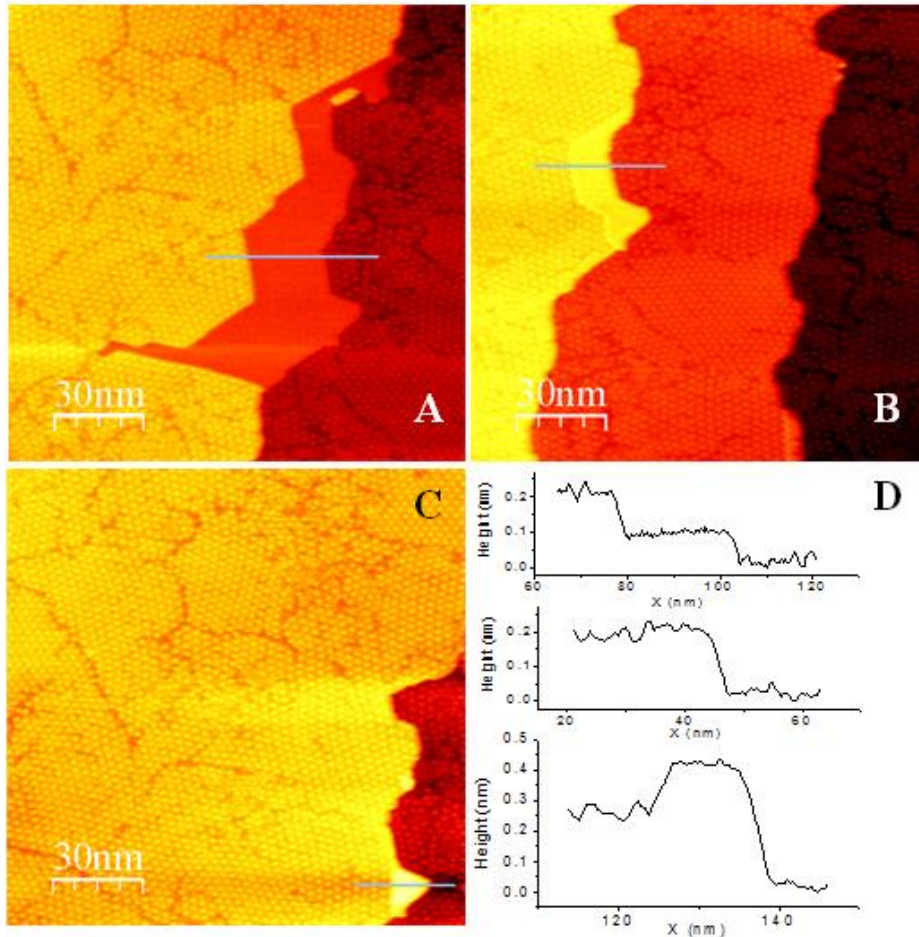


Fig. 10.2 STM images of confinement and nucleation of Rh adatoms due to graphene growth. (A) The starting situation of the graphene overlayer. The concentration of Rh adatoms is still low. (B) The same area after 761 seconds of ethylene deposition at pressures varying from 1.4×10^{-8} to 7.8×10^{-8} mbar. The apparent height of the enclosed Rh area increased, which we attribute to the increase in the concentration of Rh adatoms. (C) The final state of the vacancy island: a two-layer high Rh island has been formed by the adatoms. (D) Height profiles along the lines in images A, B, and C (top to bottom). With respect to the original level of the Rh substrate, the height of the enclosed Rh area had increased from almost 0.06 nm in A, approximately 0.2 nm in B, and 0.5 nm, corresponding to 2 layers of Rh in C.

The STM images all have a size of $150 \text{ nm} \times 150 \text{ nm}$, and have been taken at a sample voltage of $V_b = -1.84 \text{ V}$ and a tunneling current of $I_t = 0.05 \text{ nA}$.

10.3 Tunneling current vs. adatom density

In an attempt to analyze the observations more quantitatively, we first calculate the relation between the density of Rh adatoms and the apparent height in the STM images. We start from the following, simple expression for the tunneling current I over a flat piece of Rh surface.

$$I = Ae^{-\sqrt{\phi}S} \quad \text{Eq.10.1}$$

A is a constant, ϕ is the mean work function, S is the distance between tip and sample and the units have been chosen such ϕ (eV), S (Å) as to avoid additional factors in the exponent. In order to incorporate the effect of a sub-monolayer quantity of mobile Rh adatoms, we make several simplifying assumptions. Firstly, we assume that the work function above an adatom is identical to that above a flat part of the Rh surface. Secondly, we assume that each individual adatom locally changes the tunneling current as if it were a portion of a flat Rh surface, one atomic layer above the original surface. Our third assumption is that the tip exhibits a negligible force on the Rh adatoms, so that the average adatom density directly below the tip is equal to that elsewhere on the investigated Rh surface. Our final assumption is that the diffusion rate of the Rh adatoms is too high for the STM feedback loop to react to individual hopping events of Rh adatoms into and out of the tunneling gap. The consequence of the latter assumption is that the height to which the feedback loop regulates the tip is the one that corresponds with the time-averaged value of the tunneling current. This average tunneling current on a surface with a coverage θ of Rh adatoms can be written as:

$$I = (1-\theta)Ae^{-\sqrt{\phi}S} + \theta Ae^{-\sqrt{\phi}(S-H)} \quad \text{. Eq. 10.2}$$

H is the effective height of an adatom, which we associate with the interlayer spacing of the Rh crystal. When the STM is running in the constant current mode, the tip will withdraw over an additional distance h with respect to the initial tip-surface separation S_0 over a piece of Rh terrace without Rh adatoms, in order to compensate for the current increase caused by diffusing adatoms. This gives the following condition on h .

$$Ae^{-\sqrt{\phi}S_0} = (1-\theta)Ae^{-\sqrt{\phi}(S_0+h)} + \theta Ae^{-\sqrt{\phi}(S_0+h-H)} \quad \text{Eq. 10.3}$$

Solving it provides us with the following relation between the apparent height h and the Rh adatom coverage θ :

$$h = \frac{\ln[(1-\theta) + \theta e^{\sqrt{\phi}H}]}{\sqrt{\phi}} \quad \text{Eq. 10.4}$$

Substituting the values $\Phi = 5.4$ eV [95, 96] for the work function and $H = 2.2$ Å for interlayer spacing of Rh(111), we obtain the solid line in Fig. 10.3.

In the above calculation, it was assumed that the work function (apparent barrier) is constant. In reality the work function is known to depend on the distance between tip and sample, and on the roughness of the sample [97]. Both of these factors actually lower the apparent barrier. We therefore should anticipate an increase the tunneling current in the presence of adatoms. In an attempt to incorporate this effect, we assume that the apparent barrier is lowered from the original value of Φ_0 to Φ_1 , when the tip is above an adatom. This leads to a modest modification of Eq. 10.4

$$Ae^{-\sqrt{\phi_0}S_0} = (1-\theta)Ae^{-\sqrt{\phi_0}(S_0+h)} + \theta Ae^{-\sqrt{\phi_1}(S_0+h-H)}$$

$$\theta = \frac{1 - e^{\sqrt{\phi_0}h}}{1 - e^{(\sqrt{\phi_0} - \sqrt{\phi_1})(S_0+h) + H\sqrt{\phi_1}}} \quad \text{Eq. 10.5}$$

Strictly speaking, in the first term on the right side the barrier should be increased with respect to Φ_0 , but this increase is more modest than the decrease of Φ_1 with respect to Φ_0 [97]. So we here took the work function in the first term as Φ_0 . The precise value of Φ_1 and S_0 does not influence the discussion below. So we took estimated values for them. The result for a Φ_1 -value of 4.5 eV and S_0 of 0.5 nm is shown in Fig. 10.3 as the dashed curve. Of course, Eq. 10.5 properly accounts for variations in the barrier only for low coverages, where h is still small. At coverages approaching unity, Eq. 10.4 should be more appropriate. In other words, we should expect behavior that follows the dashed curve for low θ -values and crosses over to the solid curve at higher θ .

10.4 Models

We confront the two model calculations in Fig. 10.3 with the measured heights of the enclosed Rh region shown in the images of Fig. 10.1 and Fig. 10.2. From the final state (Fig. 10.1C), with a double-layer Rh island, tightly surrounded by graphene, we precisely know the excess amount of Rh. We assume that in the earlier stages precisely the same amount of Rh was distributed evenly over the bare Rh region in the form of mobile adatoms. This enables us to directly calculate the surface coverage θ in each of the earlier stages from the observed area of the enclosed Rh region. The results of this analysis, combined with the measured apparent heights of the Rh are plotted in Fig. 10.3 as the red and black squares. It is quite obvious that the experimental data do not fit either of the two model calculations very well. Most notably, the two sets of data from different areas do not coincide. Both of the experimental data exhibit a significant offset along the horizontal axis with respect to both calculations that cannot be improved by modifying the functional form of the relation between the apparent barrier and the tip-sample distance. What the experimentally determined heights strongly suggest is that the density of Rh adatoms was close to zero in the initial stages, e.g. in Fig. 10.1A. This is surprising, since this would imply that the density varied more strongly than inversely proportionally to the available area. Closer inspection of the images revealed that the graphene edge, i.e. the inner contour of the enclosed Rh area, was decorated by a protrusion. If this decorating line were to consist of Rh atoms, we could easily explain the θ -offset in the experimental data in Fig. 10.3. Assuming that at each stage, the inner contour of the graphene was decorated by a single row of Rh atoms with an interatomic distance of 0.269 nm, typical for Rh, we recalculated the coverages of the enclosed Rh areas with the remaining, mobile Rh adatoms. This procedure resulted in the red squares in Fig. 10.4. Also data for the Rh region in Fig. 10.2; in that case only part of the Rh region is enclosed by a (decorated) graphene edge, the remainder of the contour being a step in the Rh itself. The same procedure brings these data (black squares) nicely in line with those from the enclosed Rh area in Fig. 10.1. Both data sets are in nearly quantitative agreement with the two model calculations.

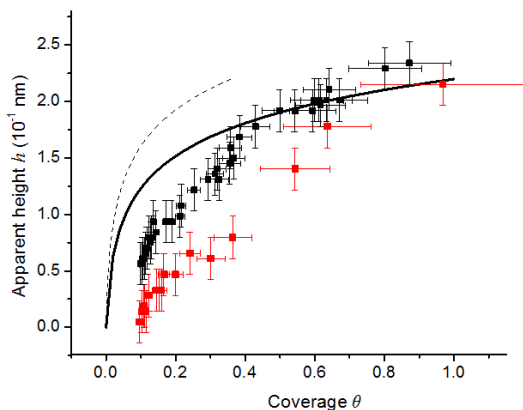


Fig. 10.3 Comparison between the experiment of Fig. 10.1 and two simple model calculations for the relation between the apparent height in the STM images and the density of adatoms. The solid line is from Eq. 10.4 and the dashed line is from Eq.10.5, in which the work function reduction due to the reduced tip-sample distance is considered. A more complete description should lie between these lines. The experimental heights, obtained from the region considered in Fig. 10.1 and in Fig. 10.2, are plotted as the red and black squares with error bars.

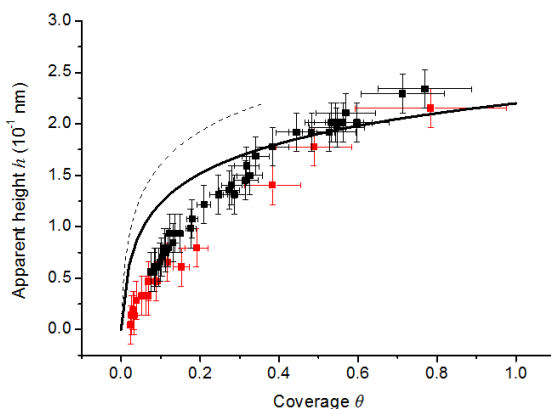


Fig. 10.4 Relation between the apparent height in STM and the density of adatoms. The solid line is from Eq. 10.4. The dashed line is from Eq. 10.5. The red squares are experimental data from the enclosed Rh area in Fig. 10.1, and the black ones are from the enclosed Rh area in Fig. 8.2. The Rh adatom density was calculated assuming that the graphene edges were all decorated by a single row of Rh atoms with an inter-atomic distance of 0.269 nm. Of the enclosed Rh area in Fig. 10.2, only the graphene edge is considered to be covered by a Rh line, rather than the entire contour around the Rh area.

10.5 Conclusion

The analysis presented in this chapter demonstrates that the edges of the growing graphene are saturated by one atomic line of Rh. Apparently, the bonding to the graphene edge makes the free energy for a Rh atom at the edge lower than that of a Rh adatom. Interestingly, this line of Rh does not have the properties of bulk Rh. We do not observe nucleation of Rh islands at the Rh-decorated graphene edges, even though the edges might seem to present an excellent nucleus. We ascribe this behavior to the strong bonding that the edge Rh atoms have to the carbon atoms at the graphene edge. We also suggest that this line of Rh may play a role in the energy barriers for graphene attachment and detachment [51, 53, 98].

Chapter 11 Growth kinetics

11.1 Introduction

Chemical vapor deposition (CVD) of hydrocarbon molecules on transition metals (TMs) provides a practical method for graphene production [25, 51-58, 99]. Detailed insight in the basic steps of the growth process of graphene will prove essential for developing procedures for the production of high-quality graphene. In order to acquire such insight, direct observations and measurements at the elevated process temperatures would be very helpful. Based on more traditional measurements after cool-down of graphene samples, it is difficult to reconstruct the processes that have taken place at high temperature. However, it is technically challenging to perform atomic-scale observations at high temperatures, and because of this difficulty, only a few reports exist of this type. Using low energy electron microscopy (LEEM), McCarty *et al.* [51, 53, 98] have performed some wonderful, *in-situ* work. They have investigated the growth of graphene from various sources, i.e. CVD, sublimation, segregation on Ru and Ir. One of the important conclusions from that work is that graphene growth is fed by the supersaturated, two-dimensional gas of C adatoms rather than by direct exchange between the C dissolved in the substrate and the graphene. The growth speed of the graphene v scales nonlinearly with the concentration of carbon adatoms C on the metal surface, according to

$$v \propto \left[\left(\frac{C}{C^{eq}} \right)^n - 1 \right] \quad \text{Eq. 11.1}$$

where $n=5$ and C^{eq} is the equilibrium density of carbon with respect to the graphene islands. The growth speed was equated to $v = \frac{1}{L} dA/dt$, where A and L are the area and perimeter of a graphene island or of a bare region of the metal substrate that is enclosed by growing graphene. The temperature-independent value of 5 for n was interpreted as

an indication that five carbon atoms are needed to form a cluster, before they can be incorporated into the graphene structure.

In this chapter, we use high-temperature scanning tunneling microscope (STM) movies to reveal the microscopic details of the growth kinetics of graphene on Rh(111). Clear evidence will be provided that on this surface the growth proceeds in unit cells of the moiré pattern between the overlayer and the substrate, which are much larger than a 5-atom C cluster. We continue to show that the addition of moiré unit cells that involve the creation of new kinks is associated with a higher energy barrier than the advancement of a kink position. Kink creation has lower barrier at a concave corner in the graphene than on a straight edge, which makes the growth speed of graphene much faster at the inner contour of a graphene vacancy island than at the outer contour of a compact graphene island. We also show that the rate at which new kinks are created at a concave corner depends on the corner angle.

All measurements were performed in an ultrahigh vacuum (UHV) system with a variable-temperature STM (prototype of the commercial VT-STM of Leiden Probe Microscopy BV). [33, 34]. The base pressure of the system was 4×10^{-11} mbar. Sample temperatures were measured by a K-type thermocouple, spot-welded directly onto the Rh single crystal. Gas pressures were measured by an ionization gauge. The sensitivity of the ionization gauge for ethylene of 2.3, relative to that for N_2 , is taken into account in all reported pressure values. The clean Rh(111) surface [73] was exposed to 1.3×10^{-5} mbar s of ethylene at room temperature, and was heated to 975 K. Graphene islands were formed on the surface with a density suitable for further *in-situ* STM measurements. On this graphene-seeded surface, which was held at 975 K throughout the rest of the experiment, STM images were recorded continuously over a period of 76 minutes, while the surface was exposed to further ethylene at pressures increasing from 1.3×10^{-10} to 1.5×10^{-8} mbar. The entire STM movie can be found online [100]. For this chapter, we have analyzed three selected episodes from the STM movie, during which the ethylene pressure was at a constant value of 5.7×10^{-9} mbar. The STM images at the start and end of each of the three episodes are shown in Fig. 11.1. In this chapter, we report images and quantitative data extracted from a single movie, but note that we have repeated the procedure several times, each time with fully equivalent results.

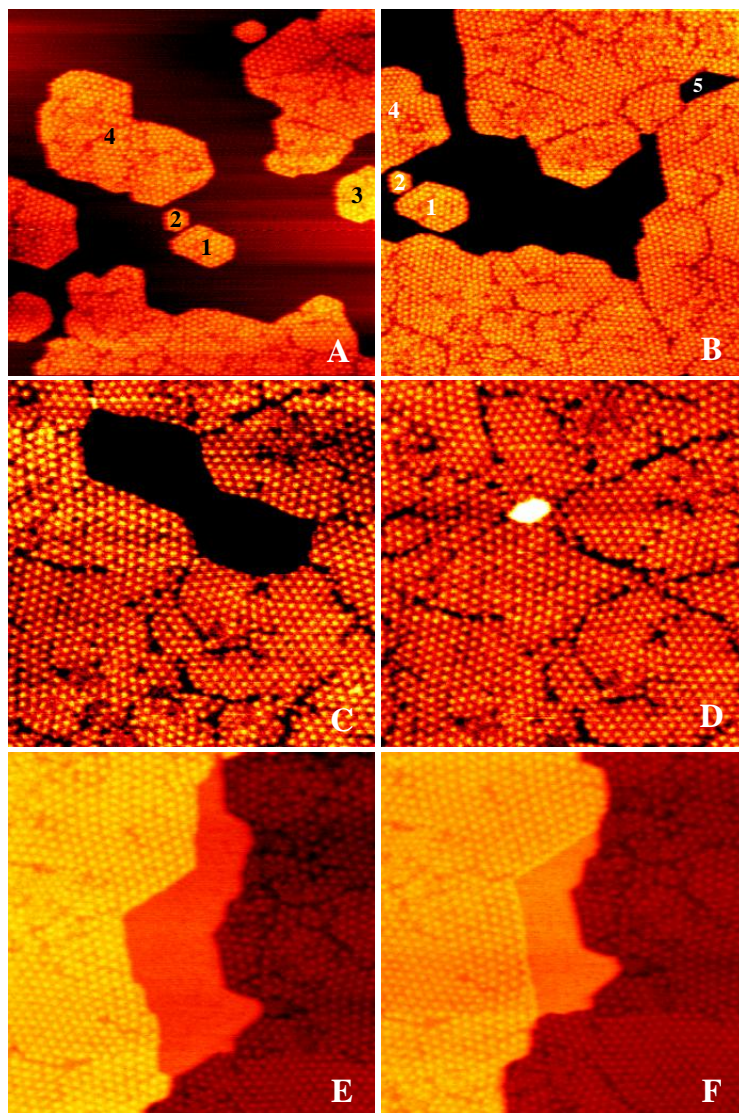


Fig. 11.1 Six snapshots from an STM movie [100], during the growth of graphene at 975 K on a graphene-seeded Rh(111) substrate at a constant ethylene pressure of 5.7×10^{-9} mbar. Frame to frame analysis was performed for the 865 s period between panels A and B, the 524 s period between C and D, and the 236 s period between E and F. The average edge advancement rates the 4 graphene islands and 1 vacancy island in A and B (labeled 1 to 5) are discussed in the text.

All images were taken at a sample voltage of $V_b = -1.84$ V and a tunneling current of $I_t = 0.05$ nA. The image sizes are 160×160 nm² for panels A and B and 100×100 nm² for panels C to F.

11.2 How the moiré pattern influences the growth

Fig. 11.2 (A-C) shows three subsequent STM images from the movie [101]. The structure that is clearly visible is the 2.9 nm moiré pattern between the aligned lattices of the graphene and the Rh. What is demonstrated by Fig. 11.2 and is observed throughout the entire movie is that the advancement of the edges appears to proceed stepwise, in units of this moiré lattice. Entire rows of such units are added. Also within the rows, the growth appears to proceed in moiré units. It starts along an edge by the creation of a new kink (or kink pair), which has a width that corresponds to the full period of the moiré lattice. After this, the new kink rapidly progresses along the edge, moving by single or multiple moiré units from image to image. This growth in moiré lattice units (288 C atoms when the graphene lattice is aligned with the Rh lattice) is reminiscent of the growth of hexagonal boron nitride on Rh(111) [20]. The rate-limiting step in the formation of a single moiré unit most probably does not involve the simultaneous arrival of 288 atoms. Otherwise, the growth rate should be exceptionally non-linear with respect to the ethylene pressure, which is in conflict with our observations and with the $n=5$ of ref. [98]. This contradiction is resolved by a growth scenario, in which C edge adatoms first need to form a cluster of a certain critical size, e.g. 5, after which the remainder of the moiré unit is formed rapidly. If this is indeed the case, it should be possible to observe intermediate configurations with incomplete moiré lattice units. Indeed, occasionally such configurations were observed, as is illustrated by Fig. 11.2D. Recent theoretical work [102] predicted that the lattice mismatch between graphene and the metal substrate influences the growth of graphene, which is now confirmed by this observation. In energy terms this implies that the energy landscape is modulated by the moiré structure: the lowest-free-energy configuration is that of an integer number of moiré units and the maximum-free-energy configuration is one in which a small number of atoms is added to that. Further addition of atoms lowers the free energy until the full 288 atoms have been added to complete the next moiré unit and the free energy is at a minimum again. The growth is then modulated in large, moiré units, but the critical nucleus is microscopic. The microscopic stable size can be 5 C atoms [98], or 24 C atoms (7 C₆ rings) as suggested by Wang *et al.* [103], and it can be different at various growth sites e.g. straight edges, corners, as discussed below. In this scenario, Eq.11.1 is still satisfied.

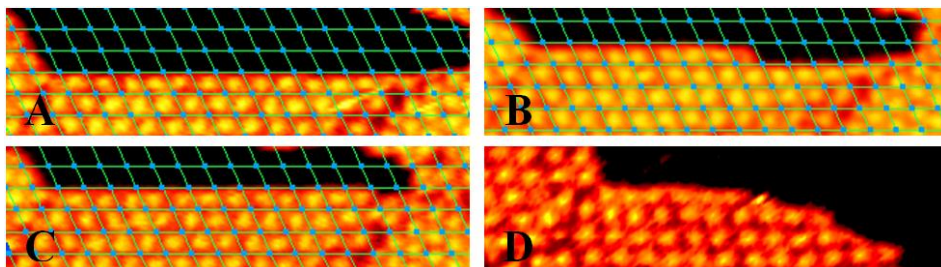


Fig. 11.2 Four snapshots from an STM movie [101], during graphene growth at 975 K on graphene-seeded Rh(111) at an ethylene pressure of 5.7×10^{-9} mbar. (A) – (C) are subsequent images (26.2 s each) of a graphene edge, starting out straight in (A), showing a kink in (B), which has advanced to the right in (C), all changes discretized in units of the moiré pattern. Panel (D) shows an incomplete moiré unit, as we observed occasionally. The grids in the image indicate the moiré pattern between graphene and the substrate. Image size: $55 \times 15 \text{ nm}^2$. Sample voltage: -1.84 V . Tunneling current: 50 pA .

All images were taken at a sample voltage of $V_b = -1.84 \text{ V}$ and a tunneling current of $I_t = 0.05 \text{ nA}$. The image sizes are $55 \times 15 \text{ nm}^2$.

In order to quantify the growth, we separate the process into two stages: kink creation and kink advancement, as shown in Fig. 11.3A. The former introduces one or more new kinks and the latter merely advances the position of an existing kink. Here we discuss direct measurements of the rates of kink formation, both on edges and at corners of the graphene overlayer and the rate of kink advancement. On internal edges of graphene vacancy islands, the creation and advancement of kinks was readily observed using STM, as shown in Fig. 11.2. On external edges of graphene patches we have hardly observed any kink; in most cases we could only observe the sudden addition of a complete row with the width of one unit cell of the moiré lattice. So, we derive the advancement rate from internal edges and use the row addition rate to get the kink formation rate. We restrict the analysis of kink formation at corners and of kink advancement to a single vacancy island (Fig. 11.1E to F) and to a limited time window, within which the change in geometry and the change in bulk C contribution (segregation) could at most have been very modest, which should result in a negligible variation in C adatom density on the metal surface. The advancement of a kink was measured to proceed at a rate of 1230 C atoms per image (26.2 s acquisition time per frame) with a surprisingly high standard deviation of 580 C atoms. If the kink were to advance by uncorrelated single-atom events, the standard deviation should have been $\sqrt{1230} = 35$.

The strong statistical variation indicates that the growth proceeds in units that are much larger than a single C atom or a 5-atom cluster, namely in units that are as large as $(580/35)^2 = 270$ atoms, fully consistent with a growth unit of 1 moiré unit cell (288 atoms). This indicates that graphene growth proceeds by the advancement of kinks that not only have a width of one complete moiré unit, but also advance effectively in steps of single moiré units.

The creation rate of new kinks at corners was found to depend on the corner angle, as shown in Fig. 11.3B. The maximum of 2 kinks/frame was still lower than the kink advancement rate of 4.3 moiré units/frame. The kink creation rate measured at the same ethylene pressure at straight edges was dramatically lower, namely 1.4×10^{-4} units/site/frame. Most kink creation events on straight edges were observed to take place at domain boundaries. We conclude that the creation of new kinks is the rate-limiting step and that this is easiest at concave corners. Even though this conclusion of growth by kink formation and advancement seems consistent with previous work [51, 98, 104], we should bare in mind that the kinks in the moiré pattern, discussed here, are much larger than the single graphene unit-cell kinks considered before.

The fact that the growth of graphene takes place at kinks in the moiré pattern should be reflected in the statistical variations in the filling rate of a graphene vacancy islands. This idea is tested in Fig. 4B, where we have plotted the time dependence of the difference in vacancy island area between subsequent frames (episode between panels C-D in Fig. 2). Below, we will discuss why this vacancy island fills up more or less exponentially with time. Fig. 11.4B shows that the filling up of the vacancy island displays significant variations, beyond the inaccuracies in the STM measurement. For example, in the first 250 seconds in Fig. 4B, the average number of C atoms added in the vacancy island between subsequent STM images is $N = 1910$, with a standard deviation of $\Delta N^{exp} = 1360$ C atoms. The experimental inaccuracy on N is no more than $\Delta N^{error} = 510$ C atoms. The extra variation $\Delta N = \sqrt{(\Delta N^{exp})^2 - (\Delta N^{error})^2}$ amounts to 1260 C atoms, which is a factor 29 larger than the expected number of \sqrt{N} , deriving from atom-by-atom statistics. This appears to support the notion that the effective growth unit is significantly larger than a single atom. However, assuming graphene to grow by building blocks of B C atoms, we expect the statistical fluctuation to be $\Delta N/N = 1/\sqrt{(N/B)}$, from which we obtain an estimate of $B = 840$ C atoms. This number is not only much larger than the 5-

atom unit of ref. [98], but also larger than the 288 C-atom size of the unit cell of the moiré pattern of graphene on Rh(111). We can easily understand this by realizing that growth only takes place at kink sites, the number of which K is also subject to statistical variations. The combined effect on the fluctuation in the number of atoms added between subsequent images is expressed by $\Delta N = \sqrt{(Rt\Delta K)^2 + (\Delta(Rt)\sqrt{K})^2}$. Here, R stands for the average rate at which C atoms attach to each kink, t is the time between images, and K is the average number of kinks within the inner contour of the vacancy island. Expressed in these quantities, $N = RtK$. The first term in the square root derives from the fluctuations in the number of kinks, while the second term represents the combination of the independent fluctuations in the advancement of K kinks. Both from individual images and from the ratio between the total filling rate and the observed advancement rate of single kinks we derive the same average number of kinks in the vacancy island of Fig. 11.1C and D of $K = 1.6$. Substituting this together with the measured values for Rt and $\Delta(Rt)$ in the expression for ΔN , we obtain an expected value for this fluctuation of 1700, which agrees reasonably well with the measured value of $\Delta N = 1260$. Note, that the main contribution to the statistical fluctuations in the filling rate result from the variation in the number of kinks.

Here we have concentrated on graphene regions that were aligned relatively well with respect to the Rh substrate. The orientation and period of the moiré pattern depends sensitively on the relative orientation of the graphene and the substrate. Also the energetic preference for forming complete moiré unit cells should be expected to depend significantly on the orientation. These aspects may influence the growth in a very complex way. Further experiments and theory are required to explore this in detail.

11.3 The influence of corner structure on kink creation

Our STM movies show that kinks are preferably created at corners and we already argued that this is because at concave corners the addition of a new moiré unit introduces only a single kink. The first image of a new kink usually shows it as either one

unit of the moiré pattern or a short row of such units, emanating from a corner. The further addition of moiré units does not involve extra kinks, which makes that a lower-energy process. In other words, the creation of new kinks is the rate-limiting step and this is easiest at concave corners. We now inspect the effect of the corner structure, in particular the corner angle, on the kink creation rate. In order to exclude systematic differences in our analysis, we only compared kink creation rates at the contour of a single enclosed Rh region, namely the one shown in Fig. 11.1E and F. Within this region, at each point in time the carbon adatom density must have been close to uniform, so that the corners in the contour experienced very similar supplies of carbon. In Fig. 11.3B, the dependence of the rate of kink creation on the angle of the graphene corner is shown, as was counted from the kink creation events recorded for each of six selected corners with different angles in the contour of the Rh region in Fig. 11.1E and F. The error margins reflect the limited number of in total 27 kink creation events that were counted. Fig. 11.3B shows that it is very difficult to create a kink at a corner with an opening angle larger than 120° and it suggests that there is a significant preference for kink formation at a 60° corner, which is a natural angle for the lattice of the graphene and that of the moiré pattern.

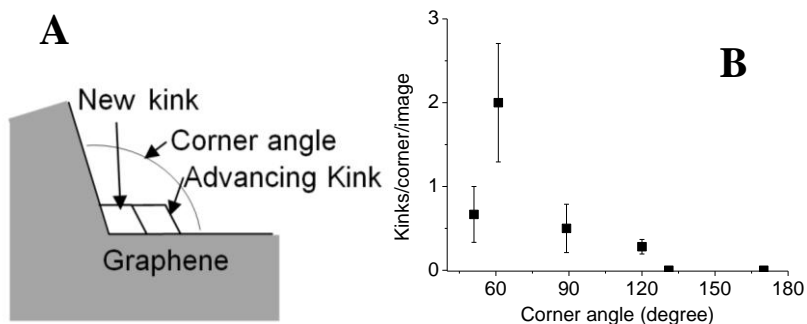


Fig. 11.3 (A) Sketch of kink creation at a concave graphene corner and subsequent kink advancement. The nucleation and growth units correspond to complete unit cells of the moiré pattern. Note that a new kink introduces two extra corners (one concave and one convex), whereas the advancement does not require the creation of further corners. (B) The measured average number of kink creation events per STM image as a function of the angle of the concave graphene corner, as measured from six corners in the graphene vacancy island of Fig. 11.1E and F.

11.4 The influence of corner energy

A problem arose when the kink creation rate (unit/frame/site) was measured, as shown in Fig. 11.3. The local structure for a kink advance is very similar as kink creation at a 120° corner. But our counting shows that the kink creation rate for 120° is 0.28 ± 0.09 unit/frame/site, while the kink advance rate is 4.75 ± 0.4 unit/frame/site. Actually, it is faster than kink creation on a corner of any angle. This can be explained by the fact that the first kink created at the corner introduces two new corners for the advance of the kinks. This means the very detailed structure, in this case corner energy of graphene, has an influence on the growth.

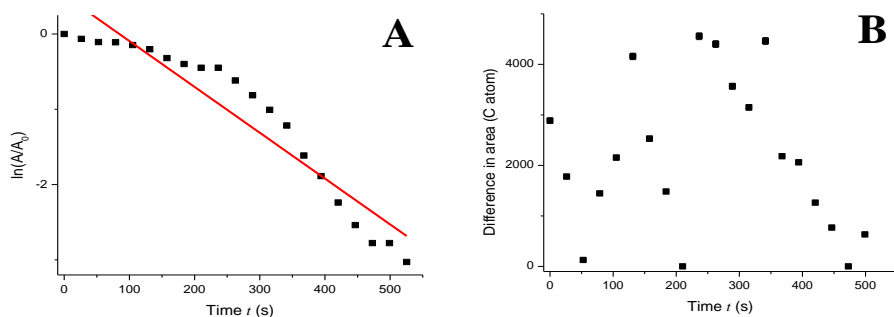


Fig. 11.4 (A) Semi-logarithmic plot of the time dependence of the area A of the enclosed Rh region in the episode between images C and D of Fig. 11.1. The linear fit to the logarithm of the area has a slope of $-6.1 \times 10^{-3} \text{ s}^{-1}$. (B) Difference in area between subsequent frames for the same episode. The error deriving from atom-by-atom statistics margins is within the symbol size.

11.5 Difference between growth at external and internal graphene edges

For the episode between panels A and B in Fig. 11.1, the average edge advancement rates $|dA/Ldt|$ of the four graphene islands and the one graphene vacancy island (labeled 1 to 5) were determined to be 1.9 ± 0.7 , 0.2 ± 0.3 , 1.7 ± 1.5 , 3.2 ± 0.5 , and $49 \pm$

27 pm/s respectively. In spite of the large error margins, we can draw two conclusions. Firstly, island 2 grew at a much lower rate than the others. In fact, the size of island 2 remained unchanged during the entire 865 s period that it was in view of the STM. Secondly, the edge of the vacancy island (labeled 5) advanced much more rapidly (more than 20 times) than the rest. As these have been truly simultaneous observations, with all island and vacancy structures exposed to equal ethylene fluxes, we assume that the concentrations of C adatoms near their edges should have been nearly equal. Therefore, we have to ascribe the differences in growth rate to differences in the edge configurations. The most important geometrical difference between graphene islands and vacancy islands within the graphene overlayer is that the contour of a vacancy island naturally contains concave corners (i.e. with angles below 180°), which can be of decisive importance. Adding the first new moiré unit requires the introduction of two new kinks along a straight step section, whereas it only requires a single kink at a concave corner. If we assume that the kink formation energy determines the rate at which new rows of moiré unit cells are initiated this rate should be significantly higher at concave corners than at straight steps or convex corners and, thus, there should be a large systematic difference in growth rate between graphene islands, with only straight steps and convex corners, and graphene vacancy islands, with primarily concave corners. This scenario also naturally explains why small graphene islands, such as island 2, grow even more slowly. To understand the latter observation, we assume that all graphene edges are populated by the same density S^{edge} of mobile C edge adatoms, in equilibrium with the C adatom density S on the surrounding metal substrate. The start of a new moiré unit cell requires the simultaneous presence of m C atoms, where m could be equal to the number $n = 5$, mentioned above. When the edge of the island is significantly shorter than am/S^{edge} , where a is the lattice constant of the graphene, the average number of C adatoms on the island edge is insufficient to get the process started, which leads to a significant suppression of the growth rate for the smaller islands. By contrast, the step advancement rate should be independent of size for the large graphene islands, as seems consistent with other work [98].

11.6 From which carbon does graphene grow?

Since the edge growth speeds were so different in Fig. 11.1, one may ask whether the edges were fed from the same source of carbon. As ethylene molecules only decompose on the bare Rh surface [51, 58], the carbon supply should become lower while the graphene coverage is increasing. In order to understand this, we first consider the assumption that in a graphene vacancy carbon adatoms cannot diffuse out of the enclosed Rh areas and the fraction of carbon escaping into the Rh substrate is negligible. Then, the total flux F of carbon atoms deposited on an enclosed Rh region should be simply proportional to the area A of this region, the impingement rate I of ethylene molecules, and the average number λ of carbon atoms deposited per impinging ethylene molecule. Since carbon is not accumulating in the enclosed area, e.g. in the form of new graphene nuclei, we can equate the flux of deposited carbon atoms to the rate at which the Rh area fills up with graphene:

$$\frac{dA}{dt} = -\frac{A}{D} I \lambda = -\frac{A}{D} \lambda \frac{P}{\sqrt{2\pi m k_b T}} = -\alpha A P \lambda$$

Here, D represents the areal density of carbon atoms in the graphene overlayer and the impingement rate of ethylene I is expressed in terms of the ethylene gas pressure P , the (gas) temperature T , and the mass m of an ethylene molecule, using standard kinetic gas theory. The part that has surely remained unchanged during deposition has been combined in the constant α , which equals $7.5 \times 10^4 \text{ mbar}^{-1} \text{ s}^{-1}$ for ethylene gas at 293 K. Based on this differential equation, we expect exponential decay of the uncovered area:

$$\ln\left(\frac{A}{A_0}\right) = -\alpha P \lambda t \quad \text{Eq. 11.2}$$

We have tested this in Fig. 11.4A by plotting the time dependence of the measured area of the enclosed Rh regions during the episode between Fig. 11.1C and D on a semi-logarithmic scale. From the slope of the straight-line fit in Fig. 11.4A, of $-6.1 \times 10^{-3} \text{ s}^{-1}$, and the ethylene pressures, we obtain an average value of $\lambda=14$. This λ -value suggests that each ethylene molecule that impinged on the Rh surface was accompanied by the addition of an average of 14 C atoms to the growing graphene layer. This greatly

exceeds the two C atoms in an ethylene molecule. Several sources of systematic error may have influenced the value of λ determined here. For example, the difference in position between the pressure gauge and the sample may have led to a systematic over- or under-estimate of the local pressure at the Rh substrate. Similarly, the presence of the STM tip may have reduced the ethylene pressure locally, precisely in the field of view of the STM. Whereas the tip-effect could only *reduce* the apparent λ , the geometry of our UHV system is such that the first effect cannot lead to an apparent *increase* of λ by more than a factor 2. Therefore, we are forced to conclude that the extra atoms must have come from the C that was dissolved in the Rh substrate during earlier stages of the deposition. The segregation of dissolved C adds a memory effect to the effective flux of C to the surface. In the early stages of graphene growth, the adatom density is high, resulting in a high rate of C dissolution. By contrast, the final stages, e.g. when the vacancy islands in the graphene are filling up, are characterized by much shorter adatom residence times and, hence, much lower adatom densities. During these stages, the dissolved C will partly re-surface and contribute to the growth rate of the graphene. We suggest that this effect is causing the high λ -value derived above.

11.7 Conclusion

In conclusion, we have shown that the moiré pattern plays an important role in the growth of graphene on Rh(111). Graphene has a preference to form complete moiré unit cells, which modulates the growth. After reaching the critical nucleus for the addition of one moiré unit, which we speculate to be a small number of added C atoms, the remaining atoms follow to quickly complete the rest of the moiré unit. By direct measurements of the rates at which moiré units are added at different sites we have drawn the following conclusions. Growth proceeds by kink creation and kink advancement, with kink creation being the rate limiting step. After a kink unit has been created on the edge of graphene, a full row of new moiré units quickly follows. It is easier to create a kink at concave corners of graphene. For this reason, the average growth rate in vacancy islands is much higher than that of compact islands. Because kink creation is the limiting step for graphene growth, differences in kink creation barrier also result in different C adatom densities during graphene growth, which has an effect on the flux of C dissolving into or segregating out of the Rh substrate.

Chapter 12 The structure of graphene on Rh

12.1 Introduction

It has been proposed that on Ru(0001) graphene is supported by a Ru 'nail' structure, with one nail under each unit cell of the moiré pattern, as sketched in Fig. 12.1 [94]. The nails have a height of one atomic layer of Ru. This support structure enables the graphene to avoid or reduce interaction with the Ru substrate, where the lattice mismatch would make this interaction unfavorable. Not only is this structure of interest in view of the competing interactions that are at play, but also because of the application potential, with this structure serving as a scaffold for the formation of nanopatterns, e.g. regular arrays of metal nanoparticles.

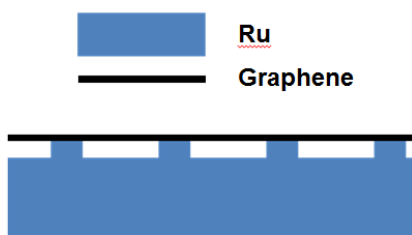


Fig. 12.1 Sketch of the 'nails' under the graphene layer on Ru(0001). Ru forms monolayer high nails on the Ru surface that support the graphene structure and reduce unfavorable interaction between the graphene and the Ru substrate [94].

Our *in-situ* growth movies of graphene on Rh(111), as illustrated by the STM images in Fig. 10.1 and Fig. 10.2, seem to indicate that the graphene layer forms on top of the Rh crystal, without the intervention of a nail structure. Nevertheless, one could still imagine that additional Rh atoms could have crept under the graphene layer to form the nails directly after the graphene had formed. In order to exclude such a scenario, we have performed a separate experiment, which has enabled us to put an upper limit on the amount of Rh incorporated as nails below a graphene island.

12.2 Experiment

The geometry that we have chosen for this experiment is that of a vacancy island in the Rh substrate, partly covered by graphene. In order to create such a geometry, we first bombarded the clean Rh(111) surface by 400eV Ar⁺ ions for 10 minutes at room temperature, and slowly warmed up the sample to 800 K. An STM measurement was performed to monitor the size and density of the vacancies on the sample. If the annealing temperature is too low or the annealing time is too short, the typical size of the vacancy islands will be small, which will result in a larger error margin in this experiment. On the other hand, if the annealing temperature is too high or the time is too long, the vacancy islands will become impractically large for our STM observations. After cooling to room temperature, we exposed the Rh sample with its vacancy islands to 2.5×10^{-7} mbar s of ethylene gas. Again the sample was slowly annealed, this time to 870 K, in order to form graphene islands within the Rh vacancy islands. Then the temperature was reduced to 745 K, to avoid further ripening of the Rh vacancy islands. Fig. 12.2A shows the typical geometry that was obtained by this preparation procedure.

In order to explore the possible presence of Rh atoms that were supporting the graphene in the Rh vacancy islands, we exposed the surface to O₂ at 745 K, thereby removing the graphene layer (Fig. 12.2B-D). It is safe to assume that it is very difficult for Rh adatoms to diffuse out of a vacancy island in the Rh substrate. So, if there were Rh nails under the graphene patch, we should expect to observe a reduction of the area of the Rh vacancy island upon removal of the graphene, when the Rh atoms that were originally in the nails would join the inner edge of the Rh vacancy island.

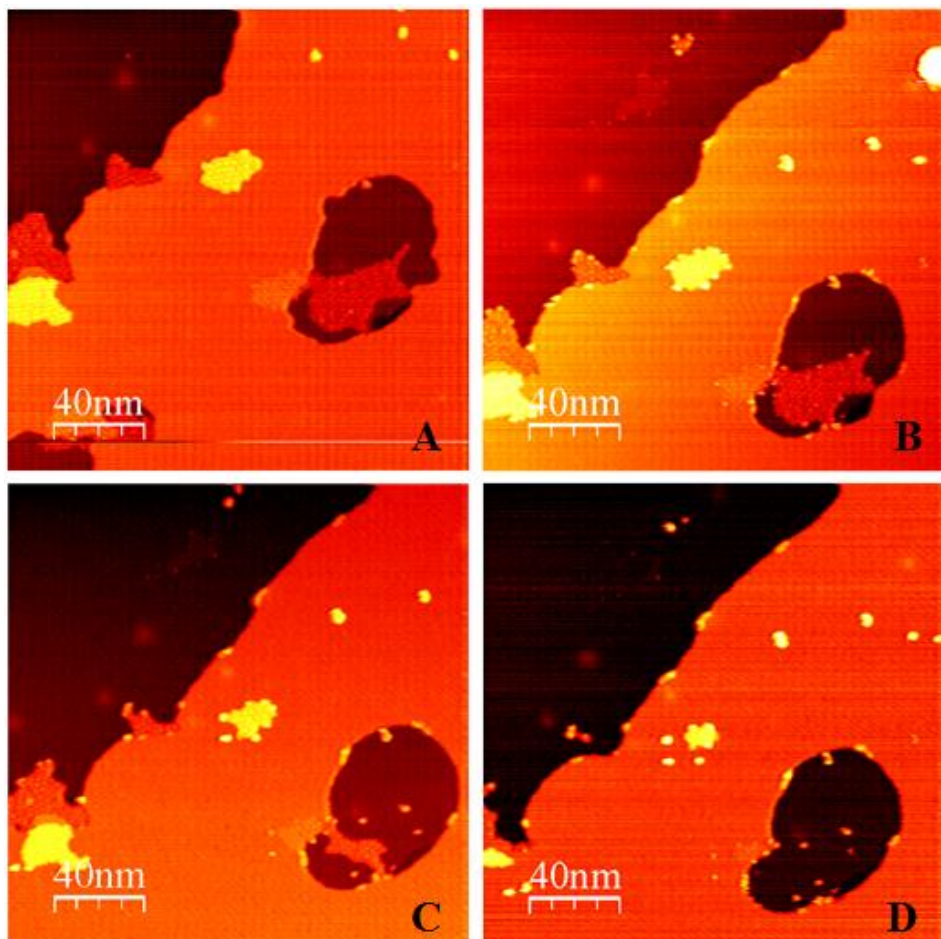


Fig. 12.2 Four snapshots from an STM measurement, in which a Rh vacancy island with a graphene patch inside was exposed to O_2 at 745 K. (A) The initial situation of this structure. (B) 160 Seconds after the start of the exposure part of the graphene island was reacted away. (C) After 251 s, most of the graphene island was removed. (D) Complete removal of the graphene patch was obtained after 319 seconds. The sizes of all images are $200 \times 200 \text{ nm}^2$; they have been taken at a sample voltage of $V_b = -0.75 \text{ V}$ and a tunneling current of $I_t = 0.05 \text{ nA}$. The frame rate was 22.8 s/frame.

12.3 Result and conclusion

In Fig. 12.3, the development with time of the area of the Rh vacancy island and that of the graphene patch in Fig. 12.2 are shown. Several STM images were measured before and after the oxygenation process, to test for systematic errors, for example, ripening of the Rh island. After O₂ had been admitted into the chamber (the increase of the green line in Fig. 12.3A), the area of graphene reduced to zero, while the area of the Rh vacancy remained very close to its original value. We note that the measured Rh area exhibits a minor, systematic error, which is presumably due to the nonlinear behavior of the STM piezo element. The modest variation in the Rh vacancy island area (black line) closely resembles the variation in measured position of the island along the horizontal axis (fast scan direction) of Fig. 12.2, including two abrupt jumps that we made to correct for the drift, one at 25 s and the other at 300 s. In order to provide an upper estimate for the number of Rh adatoms (nails) under the graphene, we fit the observed Rh vacancy island areas with the following expression.

$$A_V(t) = [\overline{A_V} - (A_{G0} - A_G(t)) \times P] \times [1 + (D(t) - \overline{D}) \times L] \quad \text{Eq. 12.1}$$

$A_V(t)$ is the expected area of the Rh vacancy island at time t ; $\overline{A_V}$ is the average area of the vacancy before O₂ exposure; A_{G0} is the initial area of the graphene patch; $A_G(t)$ is the remaining area of graphene at time t ; P is the fraction of graphene area that is supported by extra Rh atoms (nails). The second factor between square brackets corrects for the nonlinear piezo effect. Here, $D(t)$ is the distance between the center of the Rh vacancy island and the middle of the (horizontal) scan range at time t . \overline{D} is the average position of the vacancy island, prior to O₂ deposition; L indicates the strength of the image distortion, which we assumed to vary linearly with position within the image. The best-fit value for L was $8.3 \times 10^{-4} \text{ nm}^{-1}$. Calculations for three values of P , namely 0%, 5%, and 10%, are shown in Fig. 12.3B. It is very clear that the best fit is obtained for 0% Rh, i.e. complete *absence* of nails under the graphene, even though 5% Rh would still fall within the measurement accuracy. Note, that 5% would correspond to a nail size of only 6 Rh atoms, which we cannot imagine to be energetically favorable. We therefore conclude that when graphene is formed on Rh(111) the substrate remains flat and does not develop a supporting 'nail' structure.

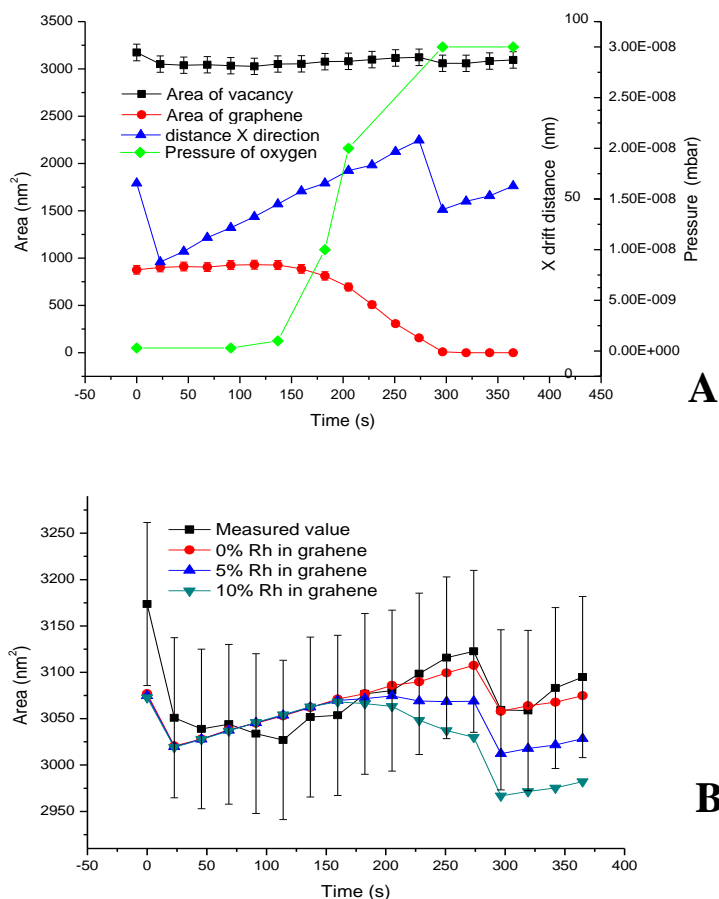


Fig. 12.3 (A) The measured areas of the Rh vacancy island (black) and the graphene patch (red) of Fig. 12.2 as a function of time. The graphene area reduced to zero when O₂ was admitted to the chamber, while the area of the Rh vacancy island did not change significantly. As explained in the text, the residual variation of the Rh vacancy is attributed to the combination of a nonlinearity of the STM scan piezo element and the drifting of the imaged vacancy island along the fast (horizontal) scan direction (blue). The green line is the pressure in the vacuum chamber, not corrected for the specific sensitivity of the pressure gauge to O₂. (B) Fits of the measured area of the Rh vacancy island, obtained with Eq.12.1 for three different values of the assumed coverage of Rh ‘nail’ atoms. The fits take the effect into account of the piezo nonlinearity. The best fit is obtained for 0% Rh, i.e. for the complete absence of nails below graphene on Rh(111).

Chapter 13 A universal description of graphene formation on transition metals

In the previous chapters, the interaction between carbon and Rh (Fig. 8.1E) has been described. Based on the experimental observations, we have been able to develop a recipe for obtaining high-quality graphene. In brief, it was found that the growth form (carbide or graphene) obtained by exposure of Rh(111) to a carbon-containing precursor gas is determined by the starting situation in the temperature range of 750 to 1016 K. Exposure to ethylene at temperatures above 1016 K can lead to full coverage of graphene, but also results in a high density of carbon atoms that have dissolved in the Rh substrate before the onset of graphene formation. These dissolved carbon atoms then segregate during cooling and destroy the high-quality graphene structure on top. Our optimized recipe is to

- (i) first pre-expose the Rh surface to ethylene at a low temperature, e.g. room temperature;
- (ii) heat up the sample, in order to form graphene nuclei;
- (iii) expose the sample at elevated temperature to further ethylene at a low pressure, in order to cover the entire surface with graphene.

The rationale behind this recipe is provided by the combination of the direct STM observations reported in part II and the considerations published by McCarty *et al.* [53], which can be combined into the following, new physical picture. In Fig. 13.1, the black line represents the density of carbon adatoms on the Rh surface, dictated by equilibrium

with carbon dissolved in the bulk. The shape and position of this line is determined by the carbon concentration in the substrate, and by the dissolution energy of carbon [53]. The solid red line represents the carbon adatom density deriving from equilibrium with the graphene islands. The point where the black line crosses the solid red line gives the dissolution temperature of graphene. We now add the solid blue line, which represents the carbon adatom density which would establish equilibrium with the carbide islands. It must be higher than the one for graphene, because a lower dissolution temperature for the carbide, at comparable carbon concentration in the bulk, has been observed. The dashed red and blue lines are the supersaturation necessary for observable nucleation of graphene and carbide. The reason that the dashed blue line (carbide) has been drawn lower than the dashed red (graphene) line is that direct deposition of ethylene between 750 K and 975 K leads to the carbide phase. The physics behind this could be that the critical nucleation size for graphene is larger.

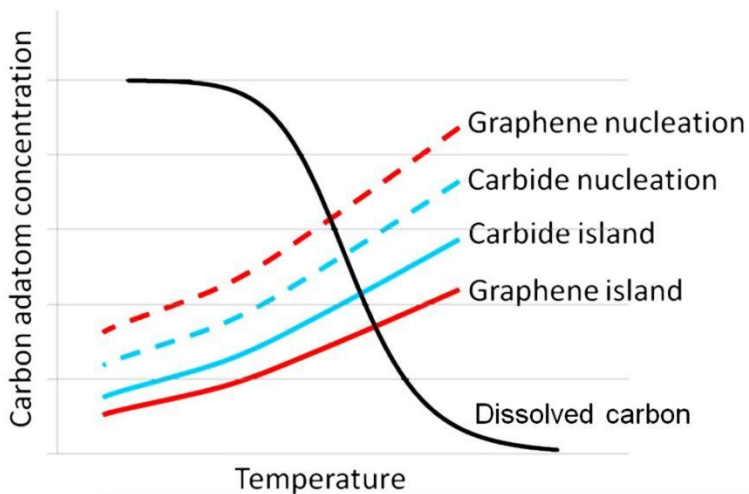


Fig. 13.1 Schematic diagram, showing the temperature dependence of various equilibrium adatom concentrations of carbon on the metal surface. The black line is the carbon adatom concentration, which is in equilibrium with carbon in the bulk. The solid red line is the adatom concentration for equilibrium with graphene islands (after [53]); the solid blue line is the adatom concentration for equilibrium with carbide islands; the locations where the solid lines cross the black line are the dissolution temperatures for graphene and carbide; the dashed red and blue lines indicate the supersaturation levels required for nucleation of graphene and carbide, respectively, on a clean metal surface.

Now let us use this simple picture to explain the complexity of the observed nucleation and growth phenomena. We start by discussing the competition between graphene and carbide formation. In the experiments where the surface is first exposed to ethylene at room temperature and then warmed up, clustering of CH_x must make the surface carbon concentration locally very high, beyond that shown by the dashed blue and red lines. Under such conditions, both carbide and graphene nuclei can be formed. With time, the carbide islands will disappear and the graphene islands will become larger, since they are energetically more favourable. This is also why the carbide may form first on metal surfaces, but after long periods of annealing (e.g., 400 minutes) at high temperature, it can transform to graphene [105]. In addition, ripening [87] is active to make the average size of the graphene islands continue to grow. When ethylene is subsequently deposited onto the seeded surface, as shown in Fig. 8.3, the system is kinetically trapped in a 'graphene-forming' mode. Now, graphene islands are already present and only a low carbon adatom density is needed to continue the growth. Because of the low ethylene pressure and the rapid incorporation of the deposited carbon into the graphene matrix, the density of adatoms cannot become high enough for nucleation of carbide (or new graphene islands). So all this taken together resulted in a surface fully covered by graphene.

Now we turn to the role of dissolved carbon atoms. When we exposed a clean Rh(111) substrate directly to ethylene at 1035 K, without the low-temperature seeding step, several dark spots appeared in the STM images, before the graphene was formed (Fig. 13.2A). Graphene formation only started when the ethylene pressure reached 3.5×10^{-7} mbar, which we associate with the dashed red line in Fig. 13.1. In the framework of Fig. 13.1, it is natural to ascribe the dark spots in Fig. 13.2 A to dissolved carbon atoms, because the supersaturation required for graphene nucleation is high enough for noticeable carbon dissolution. This dissolution leads to a relatively high concentration of carbon atoms in the substrate, close to the surface. Since the solubility of carbon in the Rh is a strong function of temperature, there is a strong driving force for the dissolved carbon atoms to segregate during cooling and accumulate between the Rh substrate and the graphene overlayer. The resulting accumulation layer distorted the regular graphene moiré patterns, as shown in the previous chapter. As can be seen in Fig. 13.2B, it was possible to partly re-dissolve these extra carbon atoms by heating the sample to the growth temperature. We speculate that this is only possible as long as the density of carbon in the accumulation layer is not sufficient for the formation of a second layer of

graphene. In the latter case, we should have observed the top graphene layer dissolve together with the accumulated (graphene) layer. Note, that the high concentration of dissolved carbon atoms led to a higher dissolution temperature (1118 K) of graphene for this sample, in agreement with our expectation from Fig. 13.1.

Fig. 13.1 shows that in order to have less C dissolved during the direct deposition, one should use a higher pressure. The argument for this counterintuitive approach is that by increasing the pressure the nucleation rate increases super-linearly, whereas the rate of dissolution will simply be proportional to the pressure. Following this idea, we have been able to improve the quality of the graphene overlayer on Rh as is demonstrated in Fig. 13.2C. The temperature of the clean Rh sample was first raised to 1028 K, after which the ethylene pressure was quickly increased to a high value of 3.9×10^{-6} mbar. The graphene layer that formed under these conditions covered the whole surface with a much lower defect density than the graphene structure shown in Fig. 8.2C. However, in spite of the high ethylene pressure used here, the moiré pattern still distorted due to segregated C when the sample was cooled to room temperature (Fig. 8.2D). The combination of the high solubility of C in Rh and the macroscopic thickness of our substrate (1 mm) made it practically impossible to completely avoid C dissolution at high temperatures and segregation of dissolved C during the cool-down.

One of the recipes reported for a single monolayer of graphene on Rh(111) is to expose the clean rhodium surface for 3 minutes to 2×10^{-7} mbar ethylene at an even higher temperature of 1100 K [89]. We have monitored this recipe with our STM at this high temperature, but graphene was not formed under these conditions and also not with longer exploring times up to 10 minutes. Instead, our images show that in this case a graphene layer was formed only after the exposure, during cooling of the sample, when the temperature had reduced to ~ 1000 K, showing that, in this recipe, the graphene film is assembled completely from segregated C. The STM images at room temperature did not show distortions, in accordance with the images in Wang et al. [89]. We attribute this absence of distortions to a nearly complete consumption of the dissolved C in the near-surface region by the graphene monolayer. The difficulty in this procedure is to precisely control the coverage, i.e., the total amount of segregated C. It is relatively easy to obtain large areas covered by graphene suitable for STM imaging or for a local spectroscopic measurement. But it is very difficult to reach full coverage of the surface with graphene of precisely one layer thickness, i.e., without any excess C.

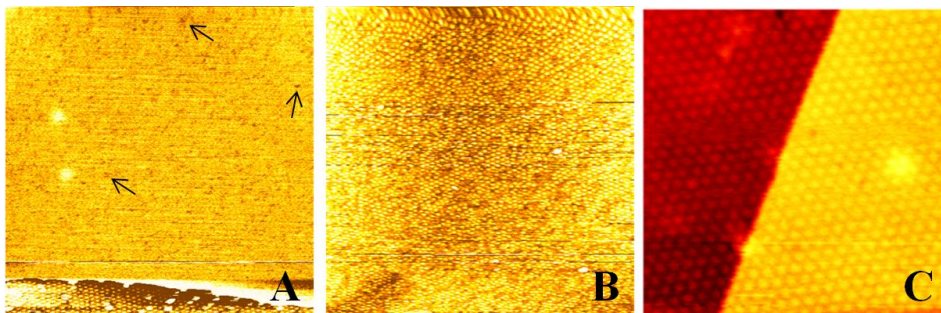


Fig. 13.2 (A) STM image before the whole surface was covered by graphene. Some dark points (indicated by the arrows), which can be caused by dissolved carbon, are visible. The temperature of the sample was 1035 K and the pressure of ethylene was 3.5×10^{-7} mbar. (B) STM image taken at 1025 K after the graphene-covered sample was cooled to room temperature and heated up again. The regular moiré structure partly reappeared during heating, after it had become distorted when the sample had been cooled to room temperature. (C) STM image of graphene-covered Rh, which was achieved by direct ethylene deposition and imaging at 1028 K. The pressure of ethylene was quickly raised to 3.9×10^{-6} mbar.

The image size is $170 \times 170 \text{ nm}^2$ for A and B, and $65 \times 65 \text{ nm}^2$ for C.

How to control the thickness of the graphene, in particular how to avoid the nucleation of the second layer below the first layer, now seems evident: after the (first) graphene layer has been formed on the metal surface, the nucleation of a second layer can be avoided by cooling down the sample very rapidly. Also by choosing a metal with a low solubility for C, for example, Cu, nucleation of the second layer can be further suppressed. The two-step recipe, first nucleation and then growth, can be used to trap the system into a state with a lower amount of dissolved C in the metal substrate as demonstrated in section 8.3. This recipe is also useful to arrive at a low growth temperature at which a minimum of C dissolves into the substrate and the graphene overlayer grows with a low strain level. In the case of Rh, this recipe still resulted in a considerable density of translational defects, due to the relatively small domain size, but on other substrates, such as Ni(111), where there is no superstructure [26], we expect that this will not pose a problem.

In conclusion, the schematic diagram in Fig. 13.1 can explain all the experimental results. And it can easily be adapted to other CVD procedures on transition metals. The key elements that may vary from system to system are the stable phases, their formation

energies and step energies, the dissolution energy, and the critical nucleation size. It can also explain why the reported recipes are sometimes not very reproducible. For example, the carbon adatom density is a function of the bulk carbon concentration. In a non-equilibrium case, it also depends on the time during which the sample was held at elevated temperature, and the rate of increase or decrease of the temperature. These parameters vary from case to case and are often not specified.

The central message of this chapter is that by following an appropriate reaction path through the diagram in Fig. 13.1 one can control the formation of the three carbon phases: graphene, carbide, and dissolved carbon. Recipes for producing high-quality graphene should not only consider temperature and pressure, but also the initial situation, the rate of temperature increase/decrease, and the bulk carbon concentration.

References

1. Gilmer, G.H. and M.H. Grabow, *MOLECULAR-DYNAMICS STUDIES OF CRYSTAL-GROWTH AND THIN-FILMS*. Acs Symposium Series, 1987. **353**: p. 218-236.
2. Cheung, J.T. and H. Sankur, *GROWTH OF THIN-FILMS BY LASER-INDUCED EVAPORATION*. Crc Critical Reviews in Solid State and Materials Sciences, 1988. **15**(1): p. 63-109.
3. Rao, U.V.S., J.S. Kumar, and K.N. Reddy, *NUCLEATION, GROWTH AND CHARACTERIZATION OF THIN SOLID FILMS*. Progress in Crystal Growth and Characterization of Materials, 1987. **15**(3-4): p. 187-314.
4. Romeo, N., *QUASI-RHEOTAXIAL GROWTH OF LARGE CRYSTALLINE GRAIN THIN-FILMS ON LOW-COST SUBSTRATES FOR PHOTOVOLTAIC APPLICATIONS*. Progress in Crystal Growth and Characterization of Materials, 1984. **9**(1-2): p. 169-183.
5. Joyce, B.A., *GROWTH AND STRUCTURE OF SEMICONDUCTING THIN-FILMS*. Reports on Progress in Physics, 1974. **37**(3): p. 363-&.
6. Corso, M., et al., *Boron nitride nanomesh*. Science, 2004. **303**(5655): p. 217-220.
7. Novoselov, K.S., et al., *Electric Field Effect in Atomically Thin Carbon Films*. Science, 2004. **306**(5696): p. 666-669.
8. Novoselov, K.S., et al., *Two-dimensional gas of massless Dirac fermions in graphene*. Nature, 2005. **438**(7065): p. 197-200.
9. Laskowski, R., P. Blaha, and K. Schwarz, *Bonding of hexagonal BN to transition metal surfaces: An ab initio density-functional theory study*. Physical Review B, 2008. **78**(4): p. -.
10. Laskowski, R. and P. Blaha, *Unraveling the structure of the h-BN/Rh(111) nanomesh with ab initio calculations*. Journal of Physics-Condensed Matter, 2008. **20**(6): p. 064207.
11. Laskowski, R., et al., *Single-layer model of the hexagonal boron nitride nanomesh on the rh(111) surface*. Physical Review Letters, 2007. **98**(10): p. 106802.
12. Bunk, O., et al., *Surface X-ray diffraction study of boron-nitride nanomesh in air*. Surface Science, 2007. **601**(2): p. L7-L10.
13. Martocchia, D., et al., *h-BN on Rh(111): Persistence of a commensurate 13-on-12 superstructure up to high temperatures*. Surface Science, 2010. **604**(5-6): p. L9-L11.

References

14. Berner, S., et al., *Boron nitride nanomesh: Functionality from a corrugated monolayer*. *Angewandte Chemie-International Edition*, 2007. **46**(27): p. 5115-5119.
15. Müller, F., S. Hübner, and H. Sachdev, *Epitaxial growth of boron nitride on a Rh(111) multilayer system: Formation and fine tuning of a BN-nanomesh*. *Surface Science*, 2009. **603**(3): p. 425-432.
16. Goriachko, A., Y.B. He, and H. Over, *Complex growth of NanoAu on BN nanomeshes supported by Ru(0001)*. *Journal of Physical Chemistry C*, 2008. **112**(22): p. 8147-8152.
17. Goriachko, A. and H. Over, *Modern Nanotemplates Based on Graphene and Single Layer h-BN*. *Zeitschrift Fur Physikalische Chemie-International Journal of Research in Physical Chemistry & Chemical Physics*, 2009. **223**(1-2): p. 157-168.
18. Dil, H., et al., *Surface trapping of atoms and molecules with dipole rings*. *Science*, 2008. **319**(5871): p. 1824-1826.
19. Widmer, R., et al., *Electrolytic in situ STM investigation of h-BN-nanomesh*. *Electrochemistry Communications*, 2007. **9**(10): p. 2484-2488.
20. Dong, G.C., et al., *How Boron Nitride Forms a Regular Nanomesh on Rh(111)*. *Physical Review Letters*, 2010. **104**(9): p. 096102.
21. Preobrajenski, A.B., et al., *Monolayer h-BN on lattice-mismatched metal surfaces: On the formation of the nanomesh*. *Chemical Physics Letters*, 2007. **446**(1-3): p. 119-123.
22. Goriachko, A., et al., *Self-assembly of a hexagonal boron nitride nanomesh on Ru(0001)*. *Langmuir*, 2007. **23**(6): p. 2928-2931.
23. Morscher, M., et al., *Formation of single layer h-BN on Pd(111)*. *Surface Science*, 2006. **600**(16): p. 3280-3284.
24. Auwarter, W., et al., *Defect lines and two-domain structure of hexagonal boron nitride films on Ni(111)*. *Surface Science*, 2003. **545**(1-2): p. L735-L740.
25. Oshima, C., et al., *A heteroepitaxial multi-atomic-layer system of graphene and h-BN*. *Surface Review and Letters*, 2000. **7**(5-6): p. 521-525.
26. Oshima, C., et al., *A hetero-epitaxial-double-atomic-layer system of monolayer graphene/monolayer h-BN on Ni(111)*. *Solid State Communications*, 2000. **116**(1): p. 37-40.
27. Oshima, C., et al., *Hetero-epitaxial double-atomic-layer system of monolayer graphene monolayer h-BN on Ni(111) studied by HREELS*. *Microbeam Analysis 2000, Proceedings*, 2000(165): p. 313-314.
28. Paffett, M.T., et al., *Borazine adsorption and decomposition at Pt(111) and Ru(001) surfaces*. *Surface Science*, 1990. **232**(3): p. 286-296.
29. Čavar, E., et al., *A single h-BN layer on Pt(111)*. *Surface Science*, 2008. **602**(9): p. 1722-1726.

30. Preobrajenski, A.B., et al., *Influence of chemical interaction at the lattice-mismatched h-BN/Rh (111) and h-BN/Pt (111) interfaces on the overlayer morphology*. Physical Review B, 2007. **75**(24): p. 245412.
31. Martoccia, D., et al., *h-BN/Ru(0001) nanomesh: A 14-on-13 superstructure with 3.5 nm periodicity*. Surface Science, 2010. **604**(5-6): p. L16-L19.
32. Goriachko, A., A.A. Zakharov, and H. Over, *Oxygen-etching of h-BN/Ru(0001) nanomesh on the nano- and mesoscopic scale*. Journal of Physical Chemistry C, 2008. **112**(28): p. 10423-10427.
33. Hoogeman, M.S., et al., *Design and performance of a programmable-temperature scanning tunneling microscope*. Review of Scientific Instruments, 1998. **69**(5): p. 2072-2080.
34. Rost, M.J., et al., *Scanning probe microscopes go video rate and beyond*. Review of Scientific Instruments, 2005. **76**(5): p. 053710.
35. Castro Neto, A.H., et al., *The electronic properties of graphene*. Reviews of Modern Physics, 2009. **81**(1): p. 109-162.
36. Westervelt, R.M., *Applied physics - Graphene nanoelectronics*. Science, 2008. **320**(5874): p. 324-325.
37. Ponomarenko, L.A., et al., *Chaotic Dirac Billiard in Graphene Quantum Dots*. Science, 2008. **320**(5874): p. 356-358.
38. Geim, A.K. and K.S. Novoselov, *The rise of graphene*. Nature Materials, 2007. **6**(3): p. 183-191.
39. Zhang, Y., et al., *Experimental observation of the quantum Hall effect and Berry's phase in graphene*. Nature, 2005. **438**(7065): p. 201-204.
40. Charlier, J.-C., X. Blase, and S. Roche, *Electronic and transport properties of nanotubes*. Reviews of Modern Physics, 2007. **79**(2): p. 677.
41. Wallace, P.R., *The Band Theory of Graphite*. Physical Review, 1947. **71**(9): p. 622.
42. McClure, J.W., *Diamagnetism of Graphite*. Physical Review, 1956. **104**(3): p. 666.
43. Du, X., et al., *Fractional quantum Hall effect and insulating phase of Dirac electrons in graphene*. Nature, 2009. **462**(08522): p. 192-195.
44. Novoselov, K.S., et al., *Room-Temperature Quantum Hall Effect in Graphene*, 2007. p. 1379-.
45. Calogeracos, A. and N. Dombey, *History and physics of the Klein paradox*, 1999, Taylor & Francis. p. 313 - 321.
46. Schmid, M., et al., *Nanotemplate with holes: Ultrathin alumina on Ni₃Al(111)*. Physical Review Letters, 2007. **99**(19): p. -.
47. Lui, C.H., et al., *Ultraflat graphene*. Nature, 2009. **462**(7271): p. 339-341.

References

48. Emtsev, K.V., et al., *Towards wafer-size graphene layers by atmospheric pressure graphitization of silicon carbide*. *Nature Materials*, 2009. **8**(3): p. 203-207.
49. Hass, J., et al., *Highly ordered graphene for two dimensional electronics*, in *Appl. Phys. Lett* 2006, AIP. p. 143106.
50. Berger, C., et al., *Electronic Confinement and Coherence in Patterned Epitaxial Graphene*. *Science*, 2006. **312**(5777): p. 1191-1196.
51. Loginova, E., et al., *Factors influencing graphene growth on metal surfaces*. *New Journal of Physics*, 2009. **11**: p. 063046.
52. Martoccia, D., et al., *Graphene on Ru(0001): A 25x25 supercell*. *Physical Review Letters*, 2008. **101**(12): p. 126102.
53. McCarty, K.F., et al., *Kinetics and thermodynamics of carbon segregation and graphene growth on Ru(0001)*. *Carbon*, 2009. **47**(7): p. 1806-1813.
54. Coraux, J., et al., *Structural coherency of graphene on Ir(111)*. *Nano Letters*, 2008. **8**(2): p. 565-570.
55. Oshima, C. and A. Nagashima, *Ultra-thin epitaxial films of graphite and hexagonal boron nitride on solid surfaces*. *Journal of Physics-Condensed Matter*, 1997. **9**(1): p. 1-20.
56. Kim, K.S., et al., *Large-scale pattern growth of graphene films for stretchable transparent electrodes*. *Nature*, 2009. **457**(7230): p. 706-710.
57. Sutter, P.W., J.I. Flege, and E.A. Sutter, *Epitaxial graphene on ruthenium*. *Nature Materials*, 2008. **7**(5): p. 406-411.
58. Wintterlin, J. and M.L. Bocquet, *Graphene on metal surfaces*. *Surface Science*, 2009. **603**(10-12): p. 1841-1852.
59. Isett, L.C. and J.M. Blakely, *Segregation Isosteres for Carbon at (100) Surface of Nickel*. *Surface Science*, 1976. **58**(2): p. 397-414.
60. Yu, Q.K., et al., *Graphene segregated on Ni surfaces and transferred to insulators*. *Applied Physics Letters*, 2008. **93**(11): p. 113103.
61. Castner, D.G., B.A. Sexton, and G.A. Somorjai, *Leed and Thermal Desorption Studies of Small Molecules (H₂, O₂, Co, Co₂, No, C₂h₄, C₂h₂ and C) Chemisorbed on Rhodium (111) and (100) Surfaces*. *Surface Science*, 1978. **71**(3): p. 519-540.
62. Shelton, J.C., H.R. Patil, and J.M. Blakely, *Equilibrium Segregation of Carbon to a Nickel (111) Surface - Surface Phase-Transition*. *Surface Science*, 1974. **43**(2): p. 493-520.
63. Bertoni, G., et al., *First-principles calculation of the electronic structure and EELS spectra at the graphene/Ni(111) interface*. *Physical Review B*, 2005. **71**(7): p. 075402.

64. Karpan, V.M., et al., *Theoretical prediction of perfect spin filtering at interfaces between close-packed surfaces of Ni or Co and graphite or graphene*. Physical Review B, 2008. **78**(19): p. 195419.
65. Sutter, P., *EPITAXIAL GRAPHENE How silicon leaves the scene*. Nature Materials, 2009. **8**(3): p. 171-172.
66. Reina, A., et al., *Large Area, Few-Layer Graphene Films on Arbitrary Substrates by Chemical Vapor Deposition*. Nano Letters, 2009. **9**(1): p. 30-35.
67. Li, X., et al., *Large-Area Graphene Single Crystals Grown by Low-Pressure Chemical Vapor Deposition of Methane on Copper*. Journal of the American Chemical Society, 2011. **133**(9): p. 2816-2819.
68. Liu, W., et al., *Synthesis of high-quality monolayer and bilayer graphene on copper using chemical vapor deposition*. Carbon, 2011. **49**(13): p. 4122-4130.
69. Li, X.S., et al., *Large-Area Synthesis of High-Quality and Uniform Graphene Films on Copper Foils*. Science, 2009. **324**(5932): p. 1312-1314.
70. Bae, S., et al., *Roll-to-roll production of 30-inch graphene films for transparent electrodes*. Nat Nano, 2010. **5**(8): p. 574-578.
71. Yu, Q., et al., *Control and characterization of individual grains and grain boundaries in graphene grown by chemical vapour deposition*. Nature Materials, 2011. **10**(6): p. 443-449.
72. Chen, J.G., et al., *Controlling surface reactivities of transition metals by carbide formation*. Journal of Molecular Catalysis a-Chemical, 1998. **131**(1-3): p. 285-299.
73. Delouise, L.A. and N. Winograd, *Carbon-Monoxide Adsorption and Desorption on Rh(111) and Rh(331) Surfaces*. Surface Science, 1984. **138**(2-3): p. 417-431.
74. Rogers, G.L., *A Simple Method of Calculating Moiré Patterns*. Proc. Phys. Soc, 1959. **73**: p. 142-144.
75. Lee, K.H., et al., *Large-Scale Synthesis of High-Quality Hexagonal Boron Nitride Nanosheets for Large-Area Graphene Electronics*. Nano Letters, 2012. **12**(2): p. 714-718.
76. Giovannetti, G., et al., *Substrate-induced band gap in graphene on hexagonal boron nitride: Ab initio density functional calculations*. Physical Review B, 2007. **76**(7): p. 073103.
77. Ramasubramaniam, A., D. Naveh, and E. Towe, *Tunable Band Gaps in Bilayer Graphene–BN Heterostructures*. Nano Letters, 2011. **11**(3): p. 1070-1075.
78. Britnell, L., et al., *Field-Effect Tunneling Transistor Based on Vertical Graphene Heterostructures*. Science, 2012. **335**(6071): p. 947-950.
79. <http://link.aps.org/supplemental/10.1103/PhysRevLett.104.096102>.
80. Zhang, Z.Y. and M.G. Lagally, *Atomistic processes in the early stages of thin-film growth*. Science, 1997. **276**(5311): p. 377-383.

References

81. Venables, J.A., *Introduction to Surface and Thin Film Processes* 2000, Cambridge: Cambridge University press.
82. Turnbull, D. and R.E. Hoffman, *The effect of relative crystal and boundary orientations on grain boundary diffusion rates*. *Acta Metallurgica*, 1954. **2**(3): p. 419-426.
83. Couling, S.R.L. and R. Smoluchowski, *ANISOTROPY OF DIFFUSION IN GRAIN BOUNDARIES*. *Journal of Applied Physics*, 1954. **25**(12): p. 1538-1542.
84. Venables, J.A., *Introduction to Surface and Thin Film Processes* 2001, Cambridge: Cambridge University press.
85. Guo, H.L., et al., *A Green Approach to the Synthesis of Graphene Nanosheets*. *ACS Nano*, 2009. **3**(9): p. 2653-2659.
86. Dubois, L.H., D.G. Castner, and G.A. Somorjai, *The Chemisorption of Acetylene and Ethylene on Rh(111) - a Low-Energy Electron-Diffraction (Leed), High-Resolution Electron-Energy Loss (Els), and Thermal-Desorption Mass-Spectrometry (Tds) Study*. *Journal of Chemical Physics*, 1980. **72**(9): p. 5234-5240.
87. Ibach, H., *Physics of Surfaces and Interfaces*. Vol. 10. 2006, Jülich: Springer-Verlag Berlin Heidelberg. 525.
88. Rut'kov, E.V., A.V. Kuz'michev, and N.R. Gall, *Carbon interaction with rhodium surface: Adsorption, dissolution, segregation, growth of graphene layers*. *Physics of the Solid State*, 2011. **53**(5): p. 1092-1098.
89. Wang, B., et al., *Coupling Epitaxy, Chemical Bonding, and Work Function at the Local Scale in Transition Metal-Supported Graphene*. *ACS Nano*, 2010. **4**(10): p. 5773-5782.
90. Sinharoy, S. and L.L. Levenson, *The formation and decomposition of nickel carbide in evaporated nickel films on graphite*. *Thin Solid Films*, 1978. **53**(1): p. 31-36.
91. Röhrl, J., et al., *Raman spectra of epitaxial graphene on SiC(0001)*. *Applied Physics Letters*, 2008. **92**(20): p. 201918.
92. Zakharchenko, K.V., M.I. Katsnelson, and A. Fasolino, *Finite Temperature Lattice Properties of Graphene beyond the Quasiharmonic Approximation*. *Physical Review Letters*, 2009. **102**(4): p. 046808.
93. van Gastel, R., et al., *Selecting a single orientation for millimeter sized graphene sheets*. *Applied Physics Letters*, 2009. **95**(12): p. 121901.
94. Starodub, E., et al., *Graphene growth by metal etching on Ru(0001)*. *Physical Review B*, 2009. **80**(23): p. 235422.
95. Bertel, E., G. Rosina, and F.P. Netzer, *The structure of benzene on Rh(111): Coadsorption with CO*. *Surface Science Letters*, 1986. **172**(1): p. L515-L522.

-
96. Sellidj, A. and B.E. Koel, *Vibrational and electronic properties of monolayer and multilayer fullerene C60 films on rhodium (111)*. The Journal of Physical Chemistry, 1993. **97**(39): p. 10076-10082.
 97. Pitarke, J.M., P.M. Echenique, and F. Flores, *Apparent Barrier Height for Tunneling Electrons in Stm*. Surface Science, 1989. **217**(1-2): p. 267-275.
 98. Loginova, E., et al., *Evidence for graphene growth by C cluster attachment*. New Journal of Physics, 2008. **10**: p. 093026.
 99. Dong, G., *Graphene formation on metal surfaces investigated by in-situ STM*. New Journal of Physics, 2012.
 100. <http://iopscience.iop.org/1367-2630/14/5/053033/media>.
 101. Dong, G.C., et al., *Graphene formation on metal surfaces investigated by in-situ scanning tunneling microscopy*. New Journal of Physics, 2012. **14**(5): p. 053033.
 102. Wu, P., et al., *Lattice Mismatch Induced Nonlinear Growth of Graphene*. Journal of the American Chemical Society, 2012. **134**(13): p. 6045-6051.
 103. Wang, B., et al., *Size-Selective Carbon Nanoclusters as Precursors to the Growth of Epitaxial Graphene*. Nano Letters, 2011. **11**(2): p. 424-430.
 104. Luo, Z., et al., *Growth Mechanism of Hexagonal-Shape Graphene Flakes with Zigzag Edges*. ACS Nano, 2011. **5**(11): p. 9154-9160.
 105. Lahiri, J., et al., *Graphene Growth on Ni(111) by Transformation of a Surface Carbide*. Nano Letters, 2011. **11**(2): p. 518-522.

Summary

Two relatively new materials have been investigated in the research that led to this thesis: hexagonal boron nitride (*h*-BN) and graphene. They have a similar structure, namely that of a film with a thickness of precisely one atomic layer, in which the atoms are arranged in a honeycomb lattice. They both come with appealing physical properties and have the potential for being applied, for example in electronics, touch screens, sensors and as coatings (for a list, see 1.3.2.). In spite of their extremely small thickness, *h*-BN and graphene remain intact under ambient conditions, in liquids, and at high temperatures. The high appeal of graphene makes it today's "hottest" material.

The method used to produce these materials that is being reported in this thesis is called chemical vapor deposition (CVD). The basic principle is the same for both materials. A precursor gas is dosed onto a clean Rh surface, namely borazine (HBNH_3) for *h*-BN and ethylene (C_2H_4) for graphene. The Rh acts as a catalyst for the decomposition of the precursor molecules. After decomposition, the H atoms desorb, while B and N or C atoms stay behind on the Rh substrate and form single-layer *h*-BN and graphene. Once the Rh surface is covered by *h*-BN or graphene, it is no longer reactive, and further precursor molecules landing on it simply desorb again. In this way, the *h*-BN or graphene stops growing by itself at a thickness of precisely one atomic layer.

Growth of these overlayers on Rh(111) is used as a model system for the growth of *h*-BN and graphene on metal surfaces in general, which is considered as one of the candidate approaches towards mass production of these materials. Even though the formation of these materials on metal surfaces is, by now, fully established, the quality of the grown layers is not optimal. Non-idealities, such as lattice defects deriving from the finite grain size, variations in thickness (i.e. combinations of single-, double- and multi-layer structures), incomplete coverage and impurity problems, all make that realistic films do not have the special physical properties that have been measured for microscopic flakes. These non-idealities are a direct consequence of the atomic-scale nucleation and growth phenomena that are active during the formation of the monolayers. In this thesis, I report on the direct visualization of these phenomena in an attempt to understand the physics behind them, and to construct new 'recipes' to optimize the quality of CVD-grown *h*-BN and graphene.

Like most chemical reactions used in practical applications, CVD of *h*-BN and graphene is carried out at elevated temperatures. The most straightforward way to investigate such reactions would be to directly 'see', with full time resolution (ps) and full spatial resolution (pm), how the impinging molecules decompose and re-assemble into new combinations, and thus follow all relevant steps in extreme detail on the atomic scale. This dream scenario can be realized partly by using a so-called scanning tunneling microscope (STM), a powerful tool with which atoms and molecules can be imaged at material surfaces. Gerd Binnig and Heinrich Rohrer (at IBM Zürich) have been honored with the 1986 Nobel Prize in Physics, only a few years after their invention of this wonderful instrument. The working principle of an STM is to scan the contour of a surface, line by line, with a macroscopic metal wire that has a typical length of several millimeters and ends in a sharp tip, with a final radius of curvature of a few tens of nanometers. The tip is held at a fixed distance to the surface, in the order of half a nanometer, by applying a modest voltage between tip and surface and keeping the small electrical current constant that results from the quantum-mechanical tunneling of electrons between the two. When this is done with sufficient precision and stability, individual atoms and molecules can be visualized. How difficult this is, can be illustrated by the simple observation that the ratio between the millimeter size of the metal wire and the sub-nanometer distances between the atoms that are imaged is as extreme as that between the height of the Eiffel tower and the thickness of a human hair. Imaging surfaces and reaction steps with an STM at elevated temperatures is very challenging, because at high temperatures the atoms are very mobile. We could extend the above analogy by comparing high-temperature STM observations to an attempt to use the tip of the Eiffel Tower to image a single human hair, while both are subjected to a strong wind! This level of difficulty explains why STM measurements are performed usually only at or below room temperature. In case of chemical reactions and other high-temperature processes, one usually first runs the high-temperature process and then cools the specimen down, before inspecting its surface in detail with an STM. Although this type of "post-mortem" measurement can yield very relevant information on the reaction that took place, this information is rather indirect, which makes it very difficult to infer the detailed, atomic-scale processes that have been at work at the high temperature. Yet, it is precisely this type of insight that is crucial for a full understanding of and, eventually full control over the reaction. After years of optimization and experimentation, we now can perform STM measurements during the growth of materials at temperatures up to 1300 K. This is a wide temperature

range that encompasses many industrial chemical processes, as well as the new processes of CVD of *h*-BN and graphene, investigated in this thesis.

For both systems, the effect of temperature is explored by first exposing an atomically clean Rh(111) surface at room temperature to a sufficiently high dose of precursor molecules to form a saturated layer of adsorbed molecules, after which the Rh substrate is heated up. During all these stages, the surface is continuously imaged with the STM. Both borazine and ethylene are found to initially form molecular clusters on the Rh surface that ripen into larger sizes as the temperature rises. At sufficiently high temperatures, between 762 and 806 K for borazine, the images indicate that the molecules decompose, resulting in the formation of *h*-BN patches. The first stage of decomposition of ethylene, namely into CH_x clusters, takes place at room temperature, while the transformation into graphene starts around 808 K. When the temperature reaches 1000 K, the orientation of the graphene islands becomes rather similar (within 5°), while the *h*-BN islands exhibit two domain orientations, with 180° rotational difference. In both cases, the Rh(111) lattice underneath dictates the preferred orientation of the overlayer. For both overlayers, the small mismatch in lattice constant between the overlayer and the substrate leads to a moiré pattern, in the form of a modulation in the height of the overlayer with a long period. For *h*-BN on Rh(111), this corrugation is known as the 'nanomesh' structure.

In experiments where clean Rh is exposed to ethylene directly at elevated temperatures, between 750 and 980 K, rhodium carbide is observed to form instead of graphene. Luckily, a narrow temperature window can be identified, in which only graphene is stable. Deposition of ethylene in this temperature window indeed produces well-ordered graphene. Unfortunately, when the specimen is cooled down to room temperature, the overlayer structure degrades dramatically, which is due to the segregation of carbon that was dissolved into the Rh substrate at the high growth temperature. The strategy that we adopt to avoid both the formation of carbides and the dissolution of significant amounts of carbon, is to first 'seed' the Rh surface with small graphene islands, by low-temperature ethylene exposure and slow heating, followed by further ethylene deposition at the regular growth temperature. In this way, graphene can be produced of a relatively high quality. In a way, one can consider our seeding approach as the introduction of an extra combination of parameters, namely the initial density of nuclei and the nature of

these nuclei – graphene – that is added to the conventional growth parameters of deposition temperature and gas pressure.

We also demonstrate that we can use the segregation of dissolved carbon to make graphene islands grow, by slowly cooling down the specimen after stopping the ethylene exposure. At lower temperatures, we are confronted with the problematic phenomenon that this type of growth leads to the spontaneous formation of double-layer Rh islands. The Rh atoms involved in these structures originate from the retraction of Rh steps, an effect that we nick-named “anti-step flow”. The mechanism behind this type of flow is that when the growing graphene overlayer ‘colonizes’ the area that is temporarily vacated by a spontaneous fluctuation in the local position of a Rh step, this step can no longer return to its original configuration; in this way, the graphene growth biases the step fluctuations of the Rh surface in the direction of an effective retraction. For Rh adatom islands, this process leads to their shrinkage. The Rh atoms that are released at the edge find themselves trapped on top of the island, where they eventually nucleate a new layer of Rh, thus leaving their mark in the form of double-layer Rh structures. With respect to the growth of graphene at its free edges, the anti-step flow mechanism of graphene growth becomes more important as the temperature is lowered. This behavior disqualifies lower-temperature deposition of graphene as a practical growth recipe.

At the end of the thesis we combine the insight obtained in our studies of graphene growth on Rh(111) into a single, qualitative picture, in which the competition between the formation and growth of graphene and carbide is described in terms of the equilibrium between dissolved carbon, carbon adatoms and islands of graphene or carbide, based on the formation energies of these overlayers and the activation energies for their nucleation. This qualitative picture also applies to graphene growth on other transition metal systems than Rh(111).

The STM growth movies of graphene and nanomesh also enable us to analyze the kinetics of the growth process in detail. For both overlayers, we find that the basic growth unit corresponds to one complete unit cell of the moiré pattern between the overlayer and the Rh substrate. From measurements of growth rates at various sites, we conclude that the growth proceeds in two steps. The first and more difficult step is the creation of a kink, with a size corresponding to a full unit cell of the moiré pattern. After this, the new kink rapidly advances, again in units of the moiré structure. In the graphene growth process, it is easier to create a kink at concave corners than on a straight edge, and we

observe a significant preference for 60° corners. In the case of *h*-BN, the edges of *h*-BN islands are terminated by either B or N atoms, which gives rise to different edge energies. The kink creation rate is higher on high-energy edges and the kink advancement rates are equal for the high- and low-energy edges. We use these observations to obtain detailed information on formation energies of new growth units, on the formation energies of boron- or nitrogen-terminated edges, and on the corner energies of the *h*-BN overlayer.

Measurements of the speed at which voids (vacancy islands) in the overlayer fill up have formed the basis for a description of precisely how precursor molecules contribute to the growth of the film. As these molecules do not decompose on the areas that are already covered by graphene/*h*-BN, the rate at which precursor molecules reach the vacancy island is directly known from the area of the vacancy island and the gas pressure of the precursor. From these measurements we learn that borazine has to land on the Rh surface close to an *h*-BN edge in order to become incorporated in the overlayer. During ethylene exposure, we find that carbon atoms dissolve into the Rh substrate when (or where) the graphene coverage is low and the surface is populated only by separate graphene islands. Under the same conditions carbon is found to segregate back to the surface when (or where) the graphene covers a larger fraction of the surface and the uncovered Rh regions are enclosed by graphene. This interesting conclusion is explained by the observation that it is easier to create a kink at concave corners than on a straight edge. As the kink creation rate is the limiting factor for graphene growth, the average growth rate at the inner perimeter of vacancy islands in the graphene overlayer is much higher than that at the outer perimeter of compact graphene islands. This difference results in different carbon adatom densities on Rh surface even when the temperature and gas pressure are the same, which affects the flux of carbon dissolving into or segregating out of the Rh substrate.

We investigate whether it is possible to improve the quality of overlayers, in particular for *h*-BN, after they have formed on the Rh substrate. If domains can be made to ripen to much larger sizes, by diffusion and annihilation of domain boundaries, this would enable one to separate the stage of deposition from that of film quality control. Our observations show that large-angle domain boundaries are removed when temperature is increased sufficiently. But the boundaries between domains with nearly equal orientations and translational domain boundaries remain stable all the way up to the temperatures at

which the *h*-BN overlayer evaporates and the graphene overlayer dissolves. This means that a large fraction of the structural defects that are introduced during the growth of these layers cannot be removed by a simple, high-temperature procedure.

Combining all the above insights into the atomic-scale mechanisms, we arrive at optimal recipes for the growth of high-quality *h*-BN and graphene films on Rh(111). In the case of *h*-BN, the message is extremely simple: the quality of the film is completely defined by the density of domain boundaries, which is dictated by the density of *h*-BN nuclei, formed in the early stages of the growth. Keeping this density low, by combining a low borazine pressure with a high deposition temperature, one can grow *h*-BN films with excellent quality. In the case of graphene there are conflicting requirements connected to the reduction of the nucleation density, the avoidance of carbide formation and the reduction of the dissolution of carbon into the Rh substrate, which would otherwise lead to multilayer growth and deterioration of film quality. In order to reasonably satisfy all requirements, we developed a two-step deposition recipe, in which we separate the stages (and conditions) of nucleation and subsequent growth.

This thesis presents two examples of atomic-scale microscopy at high temperature. The observations made here, under actual process conditions, enable us to draw detailed conclusions that go beyond the interpretations that one could reasonably obtain from post-process, room-temperature imaging. In this approach I have tried to follow the great example set by Heike Kamerlingh Onnes, the initiator of the field of low-temperature physics after whom our laboratory is named, and who has introduced the famous motto: “Door meten tot weten” (Through measurement to knowledge).

Samenvatting

Bij het onderzoek dat in dit proefschrift beschreven staat, zijn twee relatief nieuwe materialen onderzocht: hexagonaal boron nitride (h-BN) en grafeen. Deze materialen hebben dezelfde structuur: zij bestaan uit een laagje van precies één atoom dik waarin de atomen zijn gerangschikt in een honingraatrooster. Beide materialen hebben opvallende fysische eigenschappen die een grote belofte inhouden voor praktische toepassingen, bijvoorbeeld in elektronica, aanraakschermen ('touch screens'), sensoren en als coating (voor een uitgebreide lijst, zie paragraaf 1.3.2). Ondanks het feit dat h-BN en grafeen extreem dun zijn, blijven ze intact bij blootstelling aan de lucht, aan vloeistoffen en aan hoge temperaturen. Deze verbazingwekkende eigenschappen maken grafeen momenteel tot een erg 'hot' materiaal.

De manier waarop deze materialen tijdens het hier gepresenteerde onderzoek zijn gemaakt, wordt in vaktaal 'chemical vapor deposition' (CVD) genoemd. Het basisprincipe is voor beide materialen hetzelfde: een schoon oppervlak van het metaal rodium (Rh) wordt blootgesteld aan een gas; borazine ($(\text{HBNH})_3$) voor h-BN en ethyleen (C_2H_4) voor grafeen. Het rodiumsubstraat functioneert als een katalysator voor de ontleding van de moleculen van het gas. Na deze ontleding desorbeert het waterstof terwijl de B- en N-atomen of de C-atomen achter blijven op het rodiumoppervlak. Deze vormen het enkel laagje h-BN of grafeen. Nadat het rodiumsubstraat bedekt is met h-BN of grafeen, heeft het zijn reactiviteit verloren en nieuwe gasmoleculen die het oppervlak bereiken, worden weerkaatst en blijven zo in de gasfase. Op deze manier stopt de groei van h-BN en grafeen vanzelf als er zich precies één atoomlaag heeft gevormd.

De groei van deze toplagen op Rh(111) wordt gebruikt als een modelsysteem voor de groei van h-BN en grafeen op metaaloppervlakken in het algemeen. Deze groei wordt beschouwd als één van de veelbelovende methoden voor toekomstige massaproductie van deze materialen. Hoewel het maken van laagjes op metaaloppervlakken momenteel al beschouwd wordt als een routinehandeling, zijn de gegroeide lagen lang niet volmaakt. Onvolkomenheden zoals roosterdefecten als gevolg van de beperkte grafeen-domeingrootte, diktevariaties (bijvoorbeeld combinaties van enkel-, en multilaagsstructuren), onvolledige bedekking en onzuiverheden, beïnvloeden allemaal de eigenschappen die een monolaag heeft, waardoor deze minder goed stroom geleidt en ook mechanisch niet zo sterk is als zou kunnen. Deze onvolmaaktheden zijn het

directe gevolg van gebeurtenissen die plaatsvinden op atomaire schaal tijdens de nucleatie en groei van de monolagen. Dit proefschrift richt zich op het direct zichtbaar maken van deze gebeurtenissen in een poging om de fysica erachter te begrijpen en te gebruiken om nieuwe 'recepten' te construeren die de kwaliteit van het CVD-gegroei h-BN en grafeen optimaliseren.

Zoals de meeste chemische reacties die in de praktijk worden toegepast, wordt ook de CVD-groei van h-BN en grafeen uitgevoerd bij hoge temperatuur. De meest directe methode om deze reacties te bestuderen zou natuurlijk zijn om ter plekke, met voldoende tijdsresolutie (ps) en ruimtelijk oplossend vermogen (pm), te zien hoe moleculen zich ontleden en hoe atomen zich herschikken in de nieuwe structuren. Op deze manier zouden dan alle relevante stappen in uliem detail op atomaire schaal gevolgd kunnen worden. Die droom is deels gerealiseerd door middel van de zogenaamde rastertunnelmicroscop (STM): een krachtig instrument waarmee atomen en moleculen, aanwezig aan het oppervlak van materialen, in beeld gebracht kunnen worden. Gerd Binnig en Heinrich Rohrer (werkzaam bij IBM Zürich) ontvingen in 1986 de Nobelprijs voor Natuurkunde, slechts enkele jaren nadat ze dit bijzondere instrument hadden uitgevonden.

Een STM tast een oppervlak lijn voor lijn af met het uiteinde van een metalen draad. Deze draad heeft een typische lengte van enkele millimeters en eindigt in een scherpe punt met een kromtestraal van enkele tientallen nanometers. Deze punt wordt op zeer kleine afstand van het oppervlak gehouden (ongeveer een halve nanometer) door de elektrische stroom constant te houden die gaat lopen als er een bescheiden voltage aangelegd wordt tussen de punt en het in kaart te brengen substraatoppervlak. Deze stroom is een gevolg van het quantum-mechanische tunneleffect waarbij elektronen overspringen tussen de punt van de draad en het substraat. De tunnelstroom is sterk afhankelijk van de precieze afstand tussen het preparaat en de draad, en kan daarom gebruikt worden om individuele moleculen en atomen af te beelden. Dat dit aftasten van het oppervlak een hoge precisie vereist, wordt geïllustreerd door de verhouding in afmeting tussen de millimetergrote metalen draad en de sub-nanometer afstand waarop de afgebeelde atomen van elkaar zitten. Deze verhouding is net zo extreem is als die tussen de hoogte van de Eiffeltoren en de dikte van een mensenhaar. Bij hoge temperaturen zijn atomen erg beweeglijk. Dit maakt STM-waarnemingen onder de omstandigheden van de groei van grafeen en h-BN extra lastig. We kunnen de zojuist

gebruikte analogie doortrekken door ons onderzoek bij hoge temperatuur te vergelijken met het aftasten van diezelfde mensenhaar met de punt van de Eiffeltoren, terwijl het stormt! Deze hoge moeilijkheidsgraad verklaart dan ook waarom de STM-metingen in het algemeen uitgevoerd worden bij kamertemperatuur. In het geval van chemische reacties en andere hoge-temperatuur processen voert men typisch eerst het proces bij hoge temperatuur uit, waarna het preparaat wordt afgekoeld voordat er met de STM in detail naar gekeken wordt. Hoewel deze 'post mortem'-metingen zeer relevante informatie kunnen opleveren over de reacties die zich hebben voorgedaan, is die informatie vaak indirect. Dat maakt het erg lastig om de gedetailleerde, atomaire processen te herleiden die bij de hoge temperatuur plaats hebben gevonden. Nu is het juist dit soort inzicht dat cruciaal is om de reacties volledig te begrijpen en uiteindelijk volledig onder controle te krijgen. Na jaren van optimalisatie en tests is onze STM-apparatuur nu geschikt om waarnemingen te doen gedurende de groei van bovengenoemde atoomlagen bij temperaturen tot wel 1300 K. Dit grote temperatuurbereik omvat dat van vele bestaande, industriële processen maar ook dat van nieuwe CVD-processen zoals de groei van h-BN en grafeen. Dit zijn de processen die onderzocht zijn binnen het in dit proefschrift beschreven onderzoek.

In beide groeisystemen is het effect van de temperatuur in de eerste plaats onderzocht door middel van experimenten waarbij een atomair schoon Rh(111) kristaloppervlak bij kamertemperatuur werd blootgesteld aan een dosis gasmoleculen die voldoende was om een verzadigde laag van geadsorbeerde moleculen te vormen. Vervolgens is het rodiumsubstraat verhit. Gedurende dit gehele proces is het oppervlak in beeld gebracht met de STM. Op deze manier hebben we ontdekt dat zowel borazine als ethyleen eerst moleculaire clusters vormen op het metaaloppervlak, die via een rijingsproces uitgroeien tot grotere afmetingen als de temperatuur wordt verhoogd. Bij voldoende hoge temperaturen (tussen 762 en 806 K voor borazine) laten de beelden zien dat de moleculen uiteenvallen en uiteindelijk resulteert dit in de groei van h-BN eilanden. De eerste fase van het uiteenvallen van ethyleen, namelijk in CH_x -clusters, vindt plaats bij kamertemperatuur, terwijl de transformatie naar grafeen rond 808 K begint. Zodra de temperatuur 1000 K bereikt, nemen alle grafeen eilanden dezelfde oriëntatie aan (binnen 5°), terwijl de h-BN eilanden twee oriëntaties laten zien die 180° ten opzichte van elkaar verschillen. In beide gevallen dicteert het onderliggende Rh(111)-rooster de oriëntatie die de toplaag bij voorkeur aanneemt. Voor beide bovenlagen resulteert het kleine verschil in de roosterconstante tussen de bovenlaag en het substraat in een zogenoemd

moirépatroon: een hoogtemodulatie van de bovenlaag met een lange periode. Voor h-BN op Rh(111) is deze corrugatie beter bekend als de 'nanomesh'-structuur.

In de experimenten waarbij het schone rodium direct bij hoge temperatuur (tussen 750 en 980 K) wordt blootgesteld aan ethyleen, nemen we waar dat er zich rhodiumcarbide vormt in plaats van grafeen. Gelukkig is er een klein temperatuurgebied gevonden waarin uitsluitend grafeen stabiel is. Depositie van ethyleen binnen dit temperatuurvenster resulteert inderdaad in goedgeordend grafeen. Helaas verslechtert de kwaliteit van de in dit temperatuurinterval gevormde toplaag dramatisch wanneer het preparaat afgekoeld wordt naar kamertemperatuur. Dit wordt veroorzaakt door segregatie van koolstof dat bij de hogere temperatuur opgelost is in het rodium. De strategie die gevolgd wordt om zowel de vorming van carbide als het oplossen van grote hoeveelheden koolstof te voorkomen is als volgt. Allereerst wordt, bij lage temperatuur, het rodiumoppervlak 'bezaaid' met kleine grafeen eilanden. Vervolgens wordt het oppervlak bij de gebruikelijke groeitemperatuur blootgesteld aan meer ethyleen gas. Op deze manier wordt er grafeen verkregen met een relatieve hoge kwaliteit. Men zou onze aanpak van 'inzaaien' kunnen beschouwen als het introduceren van een extra combinatie van parameters, namelijk de nucleatiedichtheid aan het begin, en de structuur van deze nucleï (grafeen), die we hebben toegevoegd aan de traditionele groeiparameters, namelijk depositietemperatuur en gasdruk.

Ook hebben we kunnen aantonen dat het segregeren ('uitzwenen') van het opgeloste koolstof kan worden gebruikt om grafeen eilanden te laten groeien. Dit wordt gedaan door, na het stopzetten van de ethyleendepositie, het preparaat langzaam af te koelen. Bij lagere temperaturen worden we geconfronteerd met het probleem dat dit type groei leidt tot spontane vorming van dubbellaagse rodium eilanden. De rodiumatomen die in de gegroeide structuren aanwezig zijn, blijken afkomstig van het terugtrekken van rodium stapranden, een effect dat we de bijnaam 'anti-step flow' hebben gegeven. Het mechanisme hierachter is dat het groeiende grafeen telkens terrein in beslag neemt dat tijdelijk vrijkomt door spontane fluctuaties in de vorm en positie van een rodium stap. Daardoor kan het rodium niet meer terug en legt de grafeen groei een gemiddelde richting op aan deze fluctuaties die overeenkomt met een effectieve terugtrekking van de rodium stap. Voor rodium eilanden leidt dit proces tot een inkrimping van hun oppervlak. De rodiumatomen die bij de randfluctuaties de rand tijdelijk verlaten, bevinden zich boven op dat eiland. Daar vormen ze uiteindelijk gezamenlijk een nieuwe rodium laag.

Op deze manier ontstaan de waargenomen dubbellaags rodium structuren. In vergelijking met de 'gebruikelijke' groei, namelijk aan een vrije rand van een grafeeneiland, wordt het 'anti-step flow'-mechanisme belangrijk als de temperatuur wordt verlaagd. Helaas heeft dit gedrag een ongunstig effect op de kwaliteit van het grafeen, en diskwalificeert het daarmee recepten voor grafeengroei waarbij depositie bij lage temperatuur wordt gebruikt.

Aan het einde van dit proefschrift heb ik de inzichten gecombineerd die we verkregen hebben in dit onderzoek naar grafeen groei op Rh(111) om één volledig, kwalitatief beeld te creëren waarin de competitie tussen vorming en groei van grafeen en carbide is omschreven in termen van de evenwichten tussen opgelost koolstof, losse koolstofatomen op het oppervlak (zgn. adiatomen) en eilanden van grafeen of van carbide, dit alles gebaseerd op de vormingsenergieën van deze toplagen en de activeringsenergieën voor hun nucleatie. Dit kwalitatieve beeld is ook van toepassing op grafeen groei op andere overgangsmetalen dan rodium.

De STM video's van de groei van de grafeen en nanomesh structuren maken het ons ook mogelijk om de kinetiek van het groeiproces in detail te bestuderen. Voor beide structuren zien wij dat de groei-eenheid overeenkomt met één volledige eenheidscel van het moirépatroon tussen de toplaag en het rodium substraat. Vanuit de metingen van de groeisnelheden op verschillende plekken kunnen we concluderen dat de groei plaats vindt in twee stappen. Allereerst een wat moeilijke stap: het maken van een zogenaamde 'kink' (knik-structuur) aan de rand van de groeiende toplaag met de afmeting van een volledige eenheidscel van het moirépatroon. Daarna beweegt deze nieuwe kink zich snel voorwaarts langs de rand, opnieuw in stappen ter grootte van een dergelijke eenheidscel. In het groeiproces van grafeen is het gemakkelijker om zo'n kink te maken op een plek waar al een inwendige (concave) hoek aanwezig is, dan op plekken waar de rand van het grafeen recht loopt. Daarbij zien we een duidelijke voorkeur voor 60° hoeken. In het geval van h-BN treden er twee verschillende soorten randen op: randen waarbij de buitenste atomen B-atomen zijn en randen waarbij juist de N-atomen aan de buitenkant zitten. Dit resulteert in verschillende randenergieën. Het tempo waarin nieuwe kinken worden gevormd is hoger bij randen met een hogere energie terwijl de kinken zich langs beide soorten randen zich even snel verplaatsen. Deze waarnemingen zijn gebruikt om gedetailleerde informatie te verkrijgen zowel over de vormingsenergieën van nieuwe groei-eenheden als over de vormingsenergieën van

randen die eindigen met boor- of stikstofatomen, en over de hoekenergieën van de h-BN laag.

Metingen van de snelheid waarmee gaten (zgn. vacancy islands) in de toplaag dichtgroeien, hebben de basis gevormd van een nauwkeurige beschrijving van de bijdrage van de moleculen van het gas (borazine of ethyleen) aan de groei van deze laag. Omdat deze moleculen niet uiteenvallen op gebieden die al bedekt zijn met grafeen/h-BN, wordt het tempo waarin moleculen in zo'n gat terechtkomen volledig bepaald door het oppervlak van dat gat en de gasdruk. Onze metingen laten zien dat borazine dicht bij een h-BN rand op het rodium moet invallen om opgenomen te kunnen worden in de h-BN laag. Gedurende de blootstelling aan ethyleen zien we dat koolstofatomen oplossen in het rodium substraat gedurende de beginstadia, als de grafeen bedekking nog laag is en het oppervlak alleen bedekt wordt met afzonderlijke eilanden. Onder dezelfde omstandigheden segregereert het koolstof terug naar het oppervlak in de latere stadia, wanneer het grafeen een groter deel van het rodium bedekt en het nog onbedekte rodium bestaat uit gebiedjes die van elkaar gescheiden worden door de grafeen laag. Deze interessante conclusie kan verklaard worden met onze eerdere waarneming dat het gemakkelijker is om een kink te maken in een concave hoek dan aan een rechte rand. Omdat de kinkvorming de beperkende factor is voor grafeen groei, is de gemiddelde groeisnelheid aan de binnenranden van gaten in het grafeen veel hoger dan aan de buitenranden van losse grafeen eilanden. Dit verschil resulteert in markante veranderingen in de hoeveelheden losse koolstofatomen die tijdens de groei op het rodiumoppervlak voorhanden zijn, zelfs als de temperatuur en de gasdruk onveranderd blijven

We hebben ook onderzocht of het mogelijk is om de kwaliteit van een laag (in het bijzonder h-BN), nadat deze volgroeid is, achteraf nog te verbeteren. Als het mogelijk zou zijn om de domeinen uit te laten groeien via beweging en annihilatie van domeingrenzen, zouden het groeiproces en het kwaliteitsbepalende proces van elkaar gescheiden kunnen worden. Onze waarnemingen laten zien dat uitsluitend de domeingrenzen met grote hoeken verdwijnen als de temperatuur voldoende wordt verhoogd. Daarentegen blijven de andere domeingrenzen stabiel: de grenzen tussen domeinen die bijna gelijke oriëntaties hebben en grenzen tussen domeinen die iets verschoven zijn ten opzichte van elkaar. Deze grenzen blijven stabiel tot aan de temperaturen waarbij de h-BN laag zelf verdampt en het grafeen uit elkaar valt en oplost

in het substraat. Dit betekent dat een groot deel van de defecten in de structuur van de toplaag die ontstaan zijn tijdens de groei niet verwijderd kunnen worden via een eenvoudige hoge-temperatuur behandeling.

Alle bovengenoemde inzichten bij elkaar nemend, is het gelukt om tot een optimaal recept te komen voor het groeien van lagen van h-BN en grafeen op Rh(111) met een relatief hoge kwaliteit. In het geval van h-BN is de boodschap erg eenvoudig: de kwaliteit van de film wordt volledig bepaald door de dichtheid van de defecten in het rooster als gevolg van domeinranden. De dichtheid van deze defecten is direct gerelateerd aan de nucleatiedichtheid tijdens de eerste fase van de groei. Door deze dichtheid laag te houden (door middel van een combinatie van hoge temperatuur en lage borazine gasdruk), kan een h-BN film van excellente kwaliteit gegroeid worden. In het geval van grafeen treden er tegenstrijdige eisen op, namelijk (i) de eis dat de nucleatiedichtheid minimaal blijft, (ii) de eis dat er zich uitsluitend grafeen vormt en geen carbide en (iii) de eis dat de dichtheid van in het rodium opgelost koolstof minimaal blijft, zodat de groei van multilagen kan worden vermeden. Deze eisen kunnen op een redelijke manier gecombineerd worden met behulp van een 'recept' waarin de nucleatiefase en de verdere groeifase bij verschillende procescondities worden doorlopen.

Dit proefschrift heeft twee voorbeelden laten zien van atomaire microscopie bij hoge temperatuur. De waarnemingen die gedaan zijn onder proces-omstandigheden hebben het ons mogelijk gemaakt om gedetailleerde conclusies te trekken, die duidelijk verder gaan dan wat mogelijk geweest zou zijn op basis van traditioneel onderzoek bij kamertemperatuur, na voltooiing van het groeiproces. Bij deze benadering heb ik geprobeerd het grote voorbeeld van Heike Kamerlingh Onnes te volgen, de grondlegger van de lage-temperatuur fysica, naar wie ons laboratorium is vernoemd. Hij was het die het beroemde motto smeedde: "Van meten tot weten."

Acknowledgements

Besides the single name on the cover, there are many people who have contributed to this work. Here I would like to acknowledge their work, help, and support.

I would like to thank Jinfeng Jia, Qikun Xue, and Weisheng Yang for organizing the cooperation project between China and Leiden University, which stood at the basis of my Phd project. Great help was received from Koen Schoots and Marcel Rost when introducing me to the experimental setup, and for helping me to get started with my work in Leiden. The Nanomesh project, which hosted the initial stages of my project, could not have started without the work done by Elodie Fourré and Femke Tabak. I also thank Jürg Osterwalder and Thomas Greber from the University of Zürich for introducing us to the subject and inviting us to their European Nanomesh project, and for providing the borazine dosing system. Hermann Sachdev is gratefully acknowledged for providing high-quality borazine. The work on graphene formation was done together with Dirk van Baarle and Gijs Hijmans, who greatly accelerated this work. I am also grateful to Jan Aarts, Ji Li and Klára Uhlířova for many useful discussions. The technical support in Leiden University is excellent, for which I thank Mirthe Bergman, Arjen Geluk, Ewie de Kuyper, Jeroen Mesman, Christiaan Pen, Fred Schenkel, Peter van der Tuijn, Gijsbert Verdoes, Emiel Wiegers, Martijn Witlox, Dian van der Zalm, from the Department of Fine Mechanics, Arno van Amersfoort, Bert Crama, Raymond Koehler, Martin Moene, René Overgaw, from the Electronics Department, and Gertjan van Baarle from Leiden Probe Microscopy B.V. I also want to thank the other members of the Interface Physics Group: for the work discussions, which have helped me solve many problems and have generated many useful ideas. The administrative support by Ellie van Rijsewijk-Salman, Qingzhe Zhang, and Xuchun Ma has made my life much easier. The advice from Jan Verhoeven helped me to solve various technical problems. The correction of English by Roger Thiel has improved the readability of this work. The constant support from my family and friends, especially Zhenzhong Wang who helped me solve vacuum problems, certainly cannot be overlooked. At last, I would like to thank my supervisor Joost Frenken. He is not only a wonderful discussion partner, bringing enthusiasm and giving valuable advice, but also a great supervisor, being patient and trustful.

Publications and patents

Publications

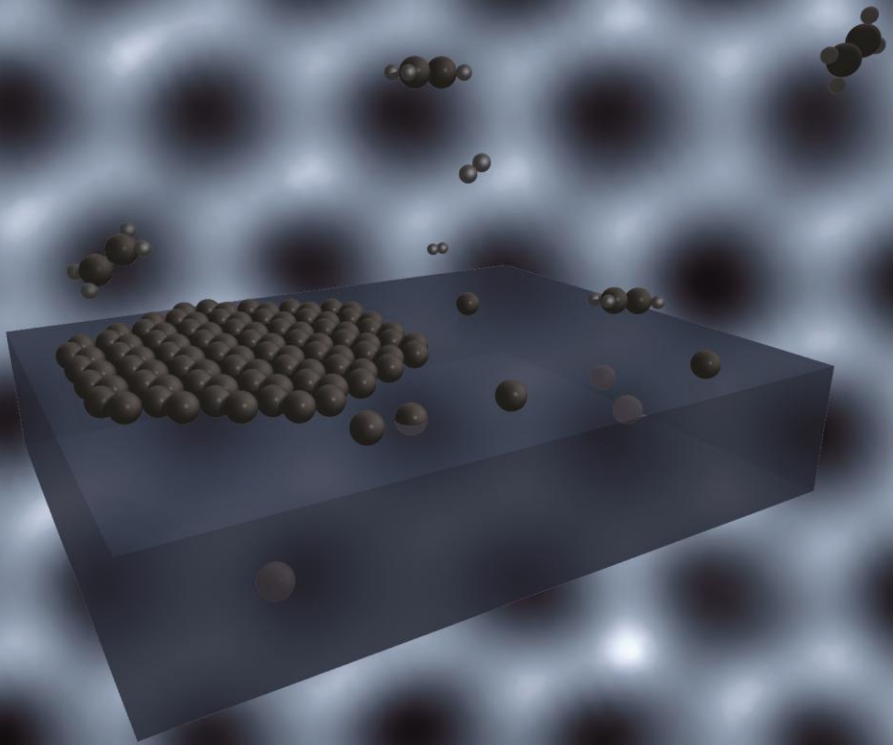
- *How boron nitride forms a regular nanomesh on Rh(111)*, PHYSICAL REVIEW LETTERS **104**, 096102 (2010), Dong G., Fourré E. B., Tabak F. C., Frenken J.W.M.
- *Graphene formation on metal surfaces investigated by in-situ STM*, NEW JOURNAL OF PHYSICS, **14**(5), 053033 (2012), Dong G., van Baarle D. W., Rost M. J., Frenken J.W.M.
- *Kinetics of graphene growth on Rh (111)*, PHYSICAL REVIEW LETTERS, submitted, Dong G., Frenken J.W.M.
- *Boron nitride nanomesh formation on Rh(111) studied by in situ STM*, in preparation, Dong G., Frenken J.W.M.
- *Self-assembled Sn nanoplatelets on Si(111)-2 root 3 x 2 root 3-Sn surface*, JOURNAL OF PHYSICS D-APPLIED PHYSICS **42**, 015305 (2009), Shen Q.T., Li W.J, Dong G., Sun G.F., Sun Y.J., Ma X.C., Jia J.F., Xue Q.K.
- *Thermal effects in photoemission from Bi(111) films on Si(111)-(7 x 7)*, SURFACE SCIENCE **602**, 102 (2008), Han T.Z., Jia J.F., Shen Q.T., Dong G., Xue Q.K.
- *Growth of Cu films on Si(111)-7 x 7 surfaces at low temperature: A scanning tunnelling microscopy study*, CHINESE PHYSICS LETTERS **24**, 3214 (2007), Shen Q.T., Sun G.F., Li W.J., Dong G., Han T.Z., Ma D.Y., Sun Y.J., Jia J.F., Xue Q.K.
- *Adhesion modulation by quantum size effects in Pb/Si(111) system*, APPLIED PHYSICS LETTERS **89**, 183109 (2006), Han T.Z., Dong G., Shen Q.T., Zhang Y.F., Jia J.F., Xue Q.K.
- *Local work function measurement on Cu(111)-Au and Cu(111)-Pd surfaces*, ACTA PHYSICA SINICA **54**, 1523 (2005), Jia J.F., Dong G., Wang L.L., Ma X.C., Xue Q.K., Hasegawa Y., Sakurai T.

Patents

- Dong G. PATENT APPLICATION NUMBER 1202080.6
- Dong G., van Rijn R. PATENT APPLICATION NUMBER 1201600.2.

Curriculum Vitae

Guocai Dong was born in Heilongjiang province, China on May 25th 1981. In 1999, he was admitted to Peking University, Beijing China, after winning the national prize in the Chinese Physics Olympiad. In 2003, after receiving his Bachelor degree in the Physics Department of Peking University, he started his research life in the field of surface science in the group of Prof. Jinfeng Jia and Prof. Qikun Xue in the Institute of Physics, CAS, Beijing China, specializing in "Growth of metal films on Si(111) studied by STM". In 2006, he joined the group of Prof. J.W.M. Frenken, in Leiden University, Leiden the Netherlands, as a PhD candidate working on the variable temperature scanning tunneling microscope. Initially, he started preparing experiments on the diffusion of metal atoms on the Si(111) surface, a topic that fit well in the collaboration with Prof. Qikun Xue. However, he got inspired by another project, namely the formation of *h*-BN nanomesh overlayers on Rh(111), that was running in parallel on the same instrument. After systematically identifying and solving all the technical imperfections in the instrumentation, he was able to routinely produce STM movies of the formation and growth of the nanomesh overlayer under a wide range of constant or varying conditions. After his success with experiments on *h*-BN, he moved his attention to a similar system, the growth of graphene on Rh(111). After finishing the two projects and writing them up as a draft for his PhD thesis, he extended his scientific research to a new and related challenge, namely large-scale and potentially commercial production of graphene, working in the same research group in Leiden as a research fellow. As part of this, he also actively took part in the initialization of a startup company named Applied Nanolayers BV. He is the first author of 2 published papers, co-author of 5 other published papers and inventor of 2 international patents.



Casimir PhD series 2012-31

ISBN: 978-90-8593-138-6